Tunable Two-Color Ultrafast Yb:Fiber Chirped Pulse Amplifier: Modeling, Experiment, and Application in Tunable Short-Pulse Mid-Infrared Generation

by

Mojtaba Hajialamdari

A thesis
presented to the University of Waterloo
in fulfillment of the
thesis requirement for the degree of
Doctor of Philosophy
in
Physics

Waterloo, Ontario, Canada, 2013

I hereby declare that I am the sole author of this thesis. This is a true copy of the thesis, including any required final revisions, as accepted by my examiners.

I understand that my thesis may be made electronically available to the public.

Abstract

In this thesis, I have developed a tunable two-color two-stage ultrafast Yb:fiber chirped pulse amplifier for the generation of short-pulse mid-infrared (MIR) radiation in the long-wavelength side of the "molecular fingerprint" (2.5-25 μm) using difference frequency generation (DFG) technique. The two colors called blue and red are in the wavelengths 1.03-1.11 μm and are amplified simultaneously in the same Yb-doped fiber amplifier (YDFA) stages in order to reduce the induced environmental noise on the phase difference of the pulses and to minimize the complexity and system cost.

I will present numerical simulations on the two-stage YDFA system to amplify a two-color spectrum in the wavelengths 1.03-1.11 μm. The first and second YDFA called preamplifier and main amplifier are single-clad, single-mode and double-clad, single-mode YDFA respectively. From numerical simulations, the optimal length of the preamplifier to have equal power at two colors centered at 1043 nm and 1105 nm are in agreement with experimental results.

It is well known that the power of MIR radiation generated by difference frequency mixing of two wavelengths scales up with the product of mixing powers in a fixed-field approximation. Furthermore, for the gain narrowing effect on the short-wavelength side of the YDFA gain profile, the spectral bandwidth of the blue color decreases resulting in pulse broadening. In addition, for the two colors separated largely, the amplified spontaneous emission is intensified. Considering the cited factors, I will present the modeling results on the two-color, two-stage YDFA system that the product of the power of the two colors is maximized for a maximized wavelength separation between the two mixing colors and a minimized gain narrowing on the blue color in order to build an as broadly tunable and powerful as possible ultrafast mid-infrared source by difference frequency mixing of the two colors.

In this research, I achieved a wavelength separation as broad as 71 nm between pulses centered at 1038 nm and 1109 nm from the two-color ultrafast YDFA system. I achieved combined average powers of 2.7 W just after the main amplifier and 1.5 W after compressing the two-color pulses centered at 1041 nm and 1103 nm to nearly Fourier transform limited pulses. From autocorrelation measurements, the full width at half maximum (FWHM) of the compressed two-color pulses with the peak wavelengths of 1041 nm and 1103 nm was $\sim$500 fs. By mixing the tunable two-color pulses in a 1-mm-thick GaSe crystal using DFG technique, I achieved tunable short-pulse MIR radiation.

In this research, I achieved short-pulse MIR radiation tunable in the wavelengths 16-20 μm. The MIR tuning range from the lower side was limited to the 16 μm because of the

71-nm limitation on the two-color separation and from the upper side was limited to the 20 μm because of the 20-μm cutoff absorption wavelength of GaSe. Based on measured MIR spectra, the MIR pulses have a picosecond pulse duration in the wavelengths 16-20 μm. The FWHM of measured spectra of the MIR pulses increases from 0.3 μm to 0.8 μm as the MIR wavelength increases from 16 μm to 20 μm. According to Fourier transform theory, the FWHM of the MIR spectra corresponds to the bandwidth of picosecond MIR pulses assuming that the MIR pulses are perfectly Fourier-transform-limited Gaussian pulses.

In this research, I achieved a maximum average power of 1.5 mW on short-pulse MIR radiation at the wavelength 18.5 μm corresponding to the difference frequency of the 500-fs two-color pulses with the peak wavelengths of 1041 nm and 1103 nm and average powers of 1350 mW and 80 mW respectively.

Considering the gain bandwidth, Ti:sapphire is a main competitor to the YDFA to be used in the two-color ultrafast laser systems. In the past, the broad gain bandwidth of Ti:sapphire crystal has resulted in synchronized two-color pulses with a wavelength separation up to 120 nm. Apart from its bulkiness and high cost, Ti:sapphire laser system is limited to a watt-level output average power at room temperature mainly due to Kerr lensing problem that occurs at high pumping powers. In comparison, YDFA as a laser amplifier has a narrower gain bandwidth but it is superior in terms of average power.

Optical parametric generation (OPG) and optical parametric amplification (OPA) techniques are two competitors to DFG technique for the generation of short-pulse long-wavelength MIR radiation. Although OPG offers a tunability range as broad as DFG, the MIR output power is lower because of the absence of input signal pulses. From the OPA technique, the tunability range is not as broad as the DFG technique due to limitations with the spectral bandwidth of the optical elements. Currently, quantum cascade lasers (QCLs) are the state-of-art MIR laser sources. At the present time, the tunability range of a single MIR QCL is not as abroad as that achieved from the DFG technique. More, mode-locked MIR QCLs are not abundant mainly because of the fast gain recovery time. Thus, the generation of widely tunable short-pulse MIR radiation from DFG technique such as that developed in this thesis remains as a persistent technological solution.

The application of the system developed in this thesis is twofold: on one hand, the tunable two-color ultrashort pulses will find applications for example in pump-probe ultrafast spectroscopy, short-pulse MIR generation, and optical frequency combs generation. On the other hand, the short-pulse MIR radiation will find applications for example in time-resolved MIR spectroscopy to study dynamical behavior of large molecules such as organic and biological molecules.

Acknowledgements

I would like to thank my PhD supervisor Professor Donna Strickland for her significant guidance, help, and support during my PhD studies. I am grateful to her for giving me the opportunity to develop my knowledge in ultrafast optics.

I would also like to thank Professors Joseph Sanderson, Li Wei, Kevin Resch, and Dayan Ban for serving as of my advisory PhD committee members and giving me insightful suggestions.

I would like to thank Canadian Institute for Photonic Innovations (CIPI) and Natural Sciences and Engineering Research Council of Canada (NSERC) for funding support.

Last but not least, a very special thank to my wife Behnaz for her support, encouragements, and patience. I am proud to share this moment with her.

Table of Contents

List of Tables

List of Figures

List of Symbols

2D	Two dimensional
ASE	Amplified spontaneous emission
BBO	β-barium borate
CPA	Chirped pulse amplification
DC	Double clad
DFG	Difference frequency generation
EC	External cavity
FWHM	Full width at half maximum
GDD	Group delay dispersion
GVW	Group velocity walk-off
MCT	HgCdTe
MIR	Mid-infrared
NA	Numerical aperture
NLO	Nonlinear optical
OPA	Optical parametric amplification
OPG	optical parametric generation
OPO	Optical parametric oscillation
PBS	polarizing beam splitter
PCF	Photonic crystal fiber
PM	Polarization maintaining
PPLN	Periodically poled lithium niobate
QCL	Quantum cascade laser
QPM	Quasi phase matching
SC	Single clad
SHG	Second harmonic generation
SOP	Stable output power
TPA	Two photon absorption
YDFA	Ytterbium doped fiber amplifier

Chapter 1

Introduction

This thesis focuses on 1- the development of a wavelength-tunable two-color ultrafast ytterbium:fiber chirped pulse amplifier in which two-color laser pulses are stretched and then amplified in the same ytterbium doped fiber amplifier (YDFA) and finally compressed, 2- the development of a wavelength-tunable short-pulse mid-infrared (MIR) source by difference frequency mixing of the output of the two-color YDFA system as well as 3- modeling of the two-color YDFA system.

In the two-color ultrafast YDFA system, the two laser pulses are amplified in the same YDFA. One of the main reasons for doing this rather than amplification of the two color pulses in separate laser amplifiers is to reduce thermo-mechanical noise on the phase difference between the two laser pulses. The reduced thermo-mechanical noise makes it unnecessary to control the pulse jitter by complicated electronic circuits. This adds some other advantages such as reduction of the system size and system cost. In this thesis, the large gain bandwidth and high average power have been in focus for using the YDFA in this research. Large heat dissipation, compact size, high beam quality, and pumping by high-power 975-nm laser diodes are some other advantages of the YDFA.

My goals of the research on the two-color YDFA system are defined as to achieve two-color laser pulses with 1- a wavelength separation as broad as possible, 2- a combined average power in the watt level optimized for the MIR generation, and 3) a sufficient bandwidth at each color for subpicosecond pulse duration.

My goals in the modeling are defined as to find the optimum fiber length of the YDFA in order to reach the goals set above for the two-color YDFA system. More, the modeling has been taken as a first step in the development of the two-color ultrafast YDFA system for understanding some of the most important behaviors and constraints of the system

such as gain competition between the two colors, amplified spontaneous emission (ASE), and gain narrowing.

The motivation in this research is to generate short-pulse MIR radiation with 1- as high as possible average power and 2- as broad as possible tunablity range in the long-wavelength range of the "molecular fingerprint". The typical wavelength range of the "molecular fingerprint" is between 2.5 μm and 25 μm which is useful for absorption spectroscopy. Few laser sources with a broad tunability within this part of spectrum can be found. It is especially challenging to generate long MIR wavelengths directly from solid-state laser gain media because most optical materials are opaque to these wavelengths.

The application of the systems developed in this thesis is twofold: on one hand, the tunable two-color ultrashort pulses will find applications for example in pump-probe ultrafast spectroscopy [1, 2], short-pulse MIR generation as demonstrated in this thesis, and optical frequency combs generation which is a hot research topic at the present time [3, 4]. On the other hand, the ultrashort MIR pulses will find applications for example in time-resolved MIR spectroscopy of large molecules. Although conventional MIR sources have been available for conventional spectroscopy, time-resolved MIR spectroscopy requires advanced MIR sources generating tunable ultrashort MIR pulses to study dynamical behavior of large molecules such as organic and biological molecules. More, explosive materials such as TNT, RDX, HMX [5], and TATP [6] show clear signatures in the wavelengths 16-20 μm. Remote detection of these explosive materials by sending the MIR radiation to the site and applying MIR spectroscopy to detected back-traveling signal is indispensable to the home land security. The research carried out in this thesis has established a successful approach for the generation of such tunable ultrashort MIR pulses.

In summary, In this research, I achieved a wavelength separation as broad as 71 nm between pulses centered at 1038 nm and 1109 nm from the two-color ultrafast YDFA system. I achieved a combined average power of 1.5 W after compressing the two-color pulses centered at 1041 nm and 1103 nm to nearly Fourier transform limited pulses. From autocorrelation measurements, the full width at half maximum (FWHM) of the compressed two-color pulses with the peak wavelengths of 1041 nm and 1103 nm was $\sim$500 fs. By mixing the tunable two-color pulses in a 1-mm-thick GaSe crystal using difference frequency generation (DFG) technique, I achieved tunable short-pulse MIR radiation.

In this research, I achieved short-pulse MIR radiation tunable in the wavelengths 16-20 μm. Based on measured MIR spectra, the MIR pulses have a picosecond pulse duration in the wavelengths 16-20 μm. The FWHM of measured spectra of the MIR pulses increases from 0.3 μm to 0.8 μm as the MIR wavelength increases from 16 μm to 20 μm. According to Fourier transform theory, the FWHM of the MIR spectra corresponds to a picosec-

ond pulse duration assuming that the MIR pulses are perfectly Fourier-transform-limited Gaussian pulses. I achieved a maximum average power of 1.5 mW at the MIR wavelength of 18.5 μm corresponding to the difference frequency of 500-fs two-color pulses with the peak wavelengths of 1041 nm and 1103 nm and average powers of 1350 mW and 80 mW respectively.

Chapter 2

Background

2.1 Broadband lasers and two-color ultrafast laser systems

The year of 1960 witnessed the discovery of the laser. In that year, the first solid state laser by Maiman [7] and the first gas laser by Javan, Bennett, and Herriott [8] were discovered. Since then, there has been a world-wide race to discover laser action from all possible materials in the solid, liquid, and gas phases. Dozens of discovered laser materials have shown a broad gain spectrum.

Lasers with a broad gain spectrum are briefly called broadband lasers. A Broadband laser gain medium is identified by its very broad emission and gain spectra. For most broadband lasers, the spectral width of the gain spectrum is smaller than the spectral width of the emission spectrum because of the overlap of the absorption spectrum with the emission spectrum as well as the bandwidth of the optical elements. Therefore, the spectral width of the emission spectrum is the maximum gain spectrum of the laser gain medium.

From Fourier transform theory, pulse duration and spectral bandwidth are inversely proportional. This indicates that for the time duration of a laser pulse to decrease its bandwidth must increase. Therefore, broadband laser gain media have been used in mode-locked lasers and short pulse laser amplifiers to provide sufficient gain bandwidth for ultrashort laser pulses.

The mode locking technique allows us to take advantage of the laser gain spectrum for generating short laser pulses. The mechanism of the generation of the mode-locked short

laser pulses is based on constructive interference of the laser cavity frequency modes in the time domain. This will happen when the phase difference between each two adjacent oscillating modes in the laser gain profile is fixed either actively or passively.

Broadband laser gain media have also been used in tunable cw lasers [9]. The combination of the two techniques has led to the development of tunable single-color mode-locked lasers [9]. Rather than using the entire gain spectrum to generate ultrashort laser pulses, the gain spectrum can be shaped to allow two short laser pulses having different colors to oscillate or be amplified in a single gain medium. These laser systems are briefly called two-color ultrafast laser systems.

In the two-color ultrafast laser systems, when the two-color laser pulses are synchronized they can be used for example in pump-probe ultrafast spectroscopy [1, 2] and optical frequency combs generation [3, 4]. When the wavelengths of the two-color laser pulses are sufficiently far apart, they can be difference frequency mixed to generate MIR radiation [10].

2.2 Ytterbium doped fiber amplifier

Etzel *et al.* achieved the laser oscillation in ytterbium doped silicate glass in 1962 [11] and Hanna *et al.* achieved the laser oscillation in ytterbium doped silica fiber in 1988 [12]. Ytterbium doped fiber amplifier has a broad gain bandwidth between 900 nm and 1200 nm [13]. The broad gain bandwidth of the YDFA can be understood from its absorption and emission spectra (see Fig. 2.1) [13]. YDFA exhibits homogeneously broadened absorption and emission spectra in the wavelengths 850-1100 nm and 900-1200 nm respectively. The broadening of the emission and absorption spectra is dominantly homogeneous because of a homogeneous crystal field in the amorphous structure of the optical fiber [14, 15]. As a result, the absorption and emission cross sections of the YDFA are continuous and homogeneously broadened. The absorption and emission cross sections of the YDFA are maximum and overlapped at 975 nm. The 975-nm absorption peak is useful for pumping the YDFA with 975-nm laser diodes. The emission cross section peaks also at $\sim$ 1030 nm which is the nominal laser wavelength of some of commercial Yb:fiber lasers.

Pumping at 975 nm, a gain bandwidth as broad as 210 nm for wavelengths above 990 nm is feasible from the YDFA. This large gain bandwidth has been used for the generation and amplification of ultrashort laser pulses [16–18], tunable short laser pulses [19], and tunable cw lasers [20, 21]. From mode-locked Yb:fiber lasers: laser pulses with durations of 36 fs [16], 33 fs [17] and 28 fs [18] have been reported. From tunable Yb:fiber laser systems a tunability as broad as 125 nm at the watt level from mode-locked Yb:fiber lasers [19],

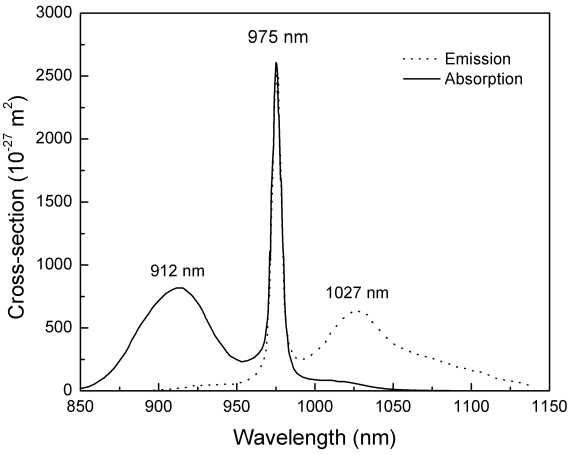

Figure 2.1: Absorption and emission cross sections of a single ytterbium ion in silica fiber. (Reproduced with permission from Ref. [13]. ©1997 IEEE.)

152 nm at the milliwatt level [20] and 110 nm at the watt level [21] from cw Yb:fiber lasers have been reported.

Another interesting characteristic of YDFA is its capability of delivering high average output powers. For example, from ultrafast YDFA systems average powers of 131-W from 220-fs, 73-MHz, 1040-nm laser pulses [22], 325 W from 375-fs, 40-MHz, 1031-nm laser pulses [23] and 830-W from 640-fs, 78-MHz, 1042-nm laser pulses [24] and from cw Yb:fiber lasers output powers of 2.1 kW at 1100 nm [25] and 10 KW [26] have been reported.

The high level of output power relies on specific properties of the YDFAs such as [13, 27–30]: low quantum defect between pump and signal wavelengths (e.g. quantum defect η is $\sim 5\%$ for the 975-nm pump and 1030-nm signal wavelengths which is calculated from $\eta = 1 - \lambda_p/\lambda_L$ where λ_p and λ_L are the wavelengths of the pump laser and laser oscillation respectively) resulting in the generation of low amount of heat at high pump powers, the very low intrinsic absorption of the silica fiber by less than 1 dB/km in the wavelengths 900-1200 nm [31], the possibility of doping the silica fibers with ytterbium to a relatively high level of concentrations by more than 10^{26} m^{-3} [32] resulting in the high gain values from a short fiber length, the large heat dissipation due to a large surface to volume ratio [33–35] resulting in reduced thermal effects such as thermally induced phase shift [36] and refractive index change [30] for maintaining the beam propagation quality at high powers, the long upper state fluorescence life time in the order of 1 ms ($\sim$ 1.5 ms in phosphorous-codoped fibers but shorter lifetimes in germanium-codoped fibers [13]) resulting in a very good energy storage medium. Moreover, in the YDFAs, the pump

and signal powers are not wasted by the excited state absorption or ion-ion concentration quenching mechanisms. This is due to the simple two-level energy structure of ytterbium ions in the silica fiber prohibiting the occurrence of these mechanisms [27] (see Appendix A for more details). The high level of output power from the YDFA systems is also grateful to double-clad Yb:fiber technology which have made it possible to guide several multi-mode high-power laser diodes in the large area of the first fiber cladding while the fiber core provides the single mode guiding property for the amplification of the single mode signals [29].

In conclusion, YDFA offers 1- a gain bandwidth as broad as 210 nm when pumped at the wavelength 975 nm and 2- a high output average power in the kilowatt level. These properties are the most important reasons for using YDFA in the development of the tunable two-color ultrafast system in this thesis.

2.3 Two-color ultrafast Yb:fiber amplifiers

From two-color ultrafast YDFA systems at the sub-watt level, wavelength separations of 60 nm [37], 65 nm [38], 67 nm [39], and 39 nm [40] and from a dual-wavelength mode-locked Yb:fiber laser at the milliwatt level a maximum wavelength separation of 35 nm [41] have been reported.

In 2003, Liu *et al.* reported a 60-nm wavelength separation from a two-color, two-stage, double-clad ultrafast Yb:fiber amplifier counter-pumped with 2-W, 965-nm laser diodes [37]. The Yb:fiber lengths were 6 m and 10 m in the preamplifier and main amplifier respectively. Liu *et al.* generated a super-continuum spectrum after injection 10-fs, 200-mW Ti:sapphire laser pulses into a 0.5-m-long photonic crystal fiber (PCF) and selected a two-color seed with an average power of 0.4 mW from the super-continuum using a grating and two-slit setup. Liu *et al.* reported a large amount of amplified spontaneous emission between the two colors after the preamplifier because the two-color seed spectrum had a power less than the noise equivalent power of the ASE. Liu *et al.* seeded the main amplifier with a 15-mW two-color spectrum (after filtering the ASE) and achieved a combined average power of 450 mW at the two colors.

In 2008, Romero-Alvarez *et al.* reported a 65-nm wavelength separation from a two-color ultrafast double-clad Yb:fiber amplifier [38] after improvements made in the setup by Liu *et al.*. Romero-Alvarez *et al.* scaled the power of the two-color seed spectrum to 5 mW by using a 5-m-long PCF pumped with a 1030-nm, 200-fs, 50-MHz, 200-mW Yb:fiber laser. The two-color spectrum was simply created by passing the super-continuum through a 50-nm-bandwidth notch filter. Romero-Alvarez *et al.* also pumped the Yb:fiber amplifiers

with more powerful, 6-W laser diodes and utilized the longer Yb:fiber in the preamplifier stage to increase the gain on the long wavelength. The main amplifier was seeded with an ASE-filtered two-color output from the preamplifier with a 60-mW average power. The authors achieved a 300-mW average power (with very little ASE) at the two short-pulse colors centered at 1038 nm and 1103 nm with a 4.5-ps FWHM at the output of the main amplifier.

In 2009, Al-Kadry and Strickland reported a 67-nm wavelength separation from a two-color ultrafast Yb:fiber chirped pulse amplifier centered at 1038 nm and 1105 nm [39] after improvements made in the amplifier setup by Romero-Alvarez *et al* and incorporating Chirped pulse amplification (CPA) technique. Al-Kadry and Strickland stretched the 200-fs super-continuum pulses using a single-mode, normal-dispersion fiber and then stretched the two-color laser pulses to a $\sim$ 40-ps pulse duration using a two-color three-grating pulse stretcher [39]. Al-Kadry and Strickland did not use a double-clad Yb:fiber in the preamplifier but used a 2.7-m single-clad Yb:fiber seeded with a 3-mW two-color spectrum and pumped from both ends with 150-mW, 976-nm laser diodes. As a result, the ASE after the preamplifier reduced noticeably. The main amplifier was a double-clad Yb:fiber amplifier counter-pumped with a 4-W, 972-nm laser diode. The authors achieved a total power of 1.1 W after the amplification stage. Al-Kadry and Strickland achieved picosecond two-color pulses with an average power of 260 mW on the 1038-nm pulses and 20 mW on the 1103-nm pulses after compressing the pulses using a two-color three-grating pulse compressor.

In 2009, Budz *et al.* reported a 39-nm wavelength separation from a two-color ultrafast Yb:fiber amplifier consisting of a 6.7-m-long polarization maintaining double-clad Yb:fiber amplifier which was counter-pumped with a 4-W, 975-nm laser diode and was seeded with two electronically-synchronized 1-ps, 577-MHz, 100-μW mode-locked external-cavity semiconductor oscillators operated at wavelengths 1040 nm and 1079 nm [40]. The authors achieved an average power of 500 mW and a pulse duration of 5 ps at each color after amplification. Budz *et al.* could not examine a larger wavelength separation because of the limited tuning range of the seed sources.

In 2012, Bai *et al.* reported a dual-wavelength operation of a passively mode-locked Yb:fiber using semiconductor saturable-absorber mirror (SESAM) for mode locking [41]. A SESAM is a Bragg mirror of quarter-wave layers whereas the layers are selected from large-band-gap semiconductor materials such as AlAs and GaAs grown on a semiconductor substrate such as GaAs and over-coated with a fast saturable absorber layer such as InGaAs [42]. The authors achieved two mode-locked wavelengths one tunable in the 1010-1058 nm and the other one tunable in the 1053-1012 nm. They achieved a wavelength separation of 35 nm with an equally distributed gain number. The authors shared an 80-cm-long

polarization maintaining Yb:fiber and a SESAM between two branch linear cavities. The Yb:fiber was pumped with a 975-nm laser diode. Each branch cavity utilized a volume Bragg grating to selectively adjust the wavelengths and reflect the beams into the cavities.

In conclusion, generating a two-color spectrum with the two colors separated as broad as possible from watt-level ultrafast Yb:fiber amplifier systems is an ongoing research. From these systems, achieving a wavelength separation as broad as the full gain bandwidth of the YDFA, *i.e.* 210 nm, is a challenging task because of gain competition between the two colors in the homogeneous gain medium of the YDFA and the very low emission cross section at long wavelengths (see Fig. 2.1). Generally, in homogeneously broadened laser gain media there exits a strong gain competition between laser wavelengths [9]. Thus, a wavelength with a lower gain coefficient is suppressed by a wavelength with a higher gain coefficient.

2.4 Tunable two-color ultrafast Ti:sapphire lasers

There are dozens of broadband laser gain media which can be used in the tunable two-color ultrafast laser amplifiers. So far, few of them have received attention for the reasons such as the gain bandwidth. Among which, Ti:sapphire for its large gain bandwidth is the main competitor to the two-color ultrafast Yb:fiber amplifier.

The laser emission from Ti:sapphire was discovered by Moulton in 1982 [43]. The absorption band of the Ti:sapphire crystal spans the wavelengths 400-630 nm which peaks around 490 nm [43]. Therefore, the blue-green lasers have been used for pumping Ti:sapphire lasers. Ti:sapphire crystal as a laser gain medium offers a broad gain bandwidth between 670 nm and 1070 nm which peaks at 790 nm [9, 43]. From this large gain bandwidth, ultrashort laser pulses with a duration of $\lesssim 6$ fs have been reported [44, 45].

The broad gain bandwidth of the Ti:sapphire crystal has resulted in the development of the tunable two-color ultrafast Ti:sapphire oscillators [46–49] and tunable two-color ultrafast Ti:sapphire laser amplifiers [50–53]. The two-color laser amplifiers have amplified either two-color laser pulses generated from the output of the two-color oscillators [50, 51] or a spectrally-shaped ultrashort-pulse single beam [52, 53].

2.4.1 Tunable two-color ultrafast Ti:sapphire oscillators

Two-color ultrafast Ti:sapphire oscillators have been developed in order to generate two synchronized ultrashort laser pulses with different wavelengths from one single Ti:sapphire

oscillator [46–49].

de Barros *et al.* achieved two-color short-pulse laser oscillations centered at 780 nm and 840 nm with a 20-nm tunability and an average power of 120 mW at each color from a two-color Ti:sapphire oscillator [46]. A Ti:sapphire rod was located between two focusing mirrors and pumped by an argon laser. The cavity was folded in a way that from one end it aimed toward a dispersion line of a prism pair and from the other end it aimed toward a saturable absorber. To achieve a two-color oscillation from the loss control method, two slits with a thin glass fiber as an obstacle in between were used between the end prism and a high-reflector mirror to shape the spectrum into a two-color spectrum. The tunable two-color operation was achieved by adjusting the prisms and end mirrors. Using one single saturable absorber, the two colors became synchronously mode locked after adjusting the distance between the two slits. Authors achieved a pulse duration $\lesssim 70$ fs at the two colors with a timing jitter < 20 fs.

Dykaar and Darack achieved two-color short-pulse laser oscillations centered at 760 nm and 780 nm with a 20-nm tunability from a two-color Ti:sapphire oscillator [47]. A single Ti:sapphire rod was located between two focusing mirrors in a Z-folded dual-cavity setup and was pumped by two spatially separated and angled argon laser beams. The Z-folded cavity ended with two D-shaped mirrors for each color. The two D-shaped mirrors at each cavity end were vertically separated by 1 mm to separate the Ti:sapphire rod into two gain regions. Authors succeeded to cancel the mode competition between the two colors by allocating each region to only one of the two colors. This was achieved by sending the two angled laser beams into the two different regions of the Ti:sapphire rod. Mode-locking at each color was achieved by Kerr lens mode locking and resulted in a pulse duration $\lesssim 100$ fs . Kerr lensing (or self focusing) produces an artificial saturable absorber by the nonlinear Kerr effect due to the nonlinear refractive index change at the beam center of a high intensity laser beam [9]. The two colors were synchronized through cross phase modulation effect. In this technique , two high intensity laser pulses interact with each other by slightly overlapping in the Ti:sapphire crystal through the nonlinear Kerr effect induced by the pulses [54]. Authors used an intracavity prism pair to compensate group velocity dispersion for both colors and the wavelength tuning was achieved by using a movable slit between the end prism and the end mirror.

Evans *et al.* demonstrated a dual-wavelength ultrafast Ti:sapphire laser [48]. Authors achieved two-color laser pulses centered at 760 nm and 850 nm with an average power of 150 mW at each color and a pulse duration $\lesssim 100$ fs. The timing jitter was recorded $\simeq 50$ fs between the two-color laser pulses. Authors used a Ti:sapphire rod in a dual-cavity setup. They pumped the Ti:sapphire rod by one single argon laser beam in a similar way that Dykaar performed. Mode locking was achieved by self focusing. The two cavities shared

the Ti:sapphire crystal and the cavity lengths were matched to obtain similar repetition rates from both cavities. Thus, simultaneous mode locking was achieved at the two colors as a result of cross phase modulation. Authors used three intracavity prisms thereby they could tune each color independently.

The method used by Dykaar *et al.* [47] was a successful approach to remove gain competition and at the same time to minimize the timing jitter between the two-color laser pulses from a two-color Ti:sapphire laser. However, they could not obtain a large wavelength separation between the two colors because of sharing the intracavity prism pair between the two colors. On the other hand, the method used by Evans *et al.* [48] was successful to independently tune each color because of using three intracavity prisms. Leitenstorfer *et al.* synthesized the systems of the two-color lasers by Dykaar and Evans [49].

Leitenstorfer *et al.* achieved two-color ultrafast laser pulses with a time duration < 30 fs and a wavelength separation as large as 100 nm from a two-color Ti:sapphire laser [49]. The average power in each color has been as high as 500 mW. A single Ti:sapphire rod was shared between two asymmetric X-folded cavities and was pumped by two spatially separated and angled argon laser beams. For each color, a set of intracavity prism pair, slit, and output coupler was used. The two colors were synchronized by the cross phase mode-locking when the cavity lengths were matched as well as the two colors overlapped in a small region of the Ti:sapphire crystal. They obtained a timing jitter < 2 fs between the two-color laser pulses. Authors observed that when the pumped regions were largely overlapped the two-color oscillation was unstable because of the mode competition between the two colors. However, they observed that it was necessary to bring the two pumped regions close enough, by a fine adjustment of the two pumping beams, for an exact synchronization via cross phase modulation.

In conclusion, the laser pulses from the two-color ultrafast Ti:sapphire oscillators have been synchronized by the cross-phase mode locking technique. From these laser systems, a combined output average power up to 1 W has been achieved. In order for the two oscillating colors being tunable, the method of adjusting intracavity prisms and slits has been successful and resulted in up to a 100-nm wavelength separation between the two colors. However, the two-color oscillators are more complicated than single color oscillators. Another approach to generate synchronized two-color pulses has been demonstrated by selecting two colors from the spectrum of ultrabroadband laser pulses from a single-color Ti:sapphire oscillator [52,53]. Yamakawa and Barty achieved synchronized two-color pulses with wavelength separations up to 120 nm by spectrally shaping 10-fs, 790-nm laser pulses from a single-color Ti:sapphire oscillator [53].

2.4.2 Tunable two-color ultrafast Ti:sapphire laser amplifiers

Two-color ultrafast Ti:sapphire chirped pulse amplifiers have been developed to simultaneously amplify the energy of the two-color laser pulses [50–53]. These two-color ultrafast Ti:sapphire laser amplifiers have been seeded by either the output of a two-color mode-locked Ti:sapphire oscillator [50, 51] or spectrally-shaped ultrashort laser pulses from the output of a single-color mode-locked Ti:sapphire oscillator [52, 53]. The two-color seed has been amplified either in a regenerative laser amplifier [50, 52, 53] or a combination of regenerative and multi-pass laser amplifiers [51]. From these laser systems, ultrashort two-color laser pulses have been stretched before the Ti:sapphire amplifiers to 200 ps using a standard all-reflective single-grating stretcher [50, 51] and to 900 ps using an all-reflective, cylindrical mirror-based pulse stretcher [53]. After amplification, the two-color laser pulses have been compressed to $\sim$ 150 fs using a three-grating pulse compressor [50, 51, 53]. Wavelength separations as large as 90 nm [50, 51], 55 nm [52], and 120 nm [53] and a total energy of 1.5 mJ [50], 15 mJ [51], 1 mJ [52], and 10 mJ [53] have been reported.

In a two-color Ti:sapphire regenerative amplifier, a Ti:sapphire crystal was placed inside a two-color folded laser cavity [50–52] or a ring laser cavity [53] and was pumped by a multiwatt green laser. To control the loss between the two colors, an intracavity three-prism setup in the folded cavity or an intracavity notch filter in the ring cavity was used. An intracavity polarizing beam splitter (PBS) was used to inject the seed pulses into the cavity. To control the number of passes, an intracavity Pockel cell was used to rotate the polarization of the pulses by 90° after activating the Pockel cell at a half-wave voltage thereby the laser pulses were trapped in the cavity as there was no reflection from the PBS. After a number of passes, the amplified beam was dumped from the laser cavity when a half-wave voltage was again applied on the Pockel cell. At this time, the polarization of the beam was the same as input seed (after a total rotation of 180°) and the amplified beam was reflected off from the same PBS in the two-color folded laser cavity [50–52] or a second PBS after the Pockel cell in the ring laser cavity [53].

The regenerative laser amplifier is used to amplify low energy laser pulses [9]. A regenerative laser amplifier allows us to control the number of passes of the seed beam through a laser gain medium which is pumped by another laser. After each pass the energy of the laser pulses increases by extracting more energy from the laser gain medium. The regenerative laser amplifier enables us to achieve a large gain factor by providing a large number of passes through the laser gain medium. However, the energy extraction is limited with the damage threshold and self focusing in the laser crystal. For this, after the regenerative laser amplifier, a multi-pass laser amplifier is used whereas the laser beam size is increased in each pass thereby the laser intensity remains below the damage threshold and self focus-

ing threshold. Thus, more energy can be extracted from the laser crystal. In a two-color multi-pass Ti:sapphire laser amplifier, the input pulses traversed a laser gain medium five passes in different angles and resulted in an output pulse energy of 15 mJ [51]. For this, the laser crystal was placed symmetrically between a number of separated beam reflectors whereas each reflector guided the input pulses and pump beam into the laser crystal in a different angle.

In conclusion, the two-color ultrafast Ti:sapphire oscillators discussed previously have provided a technical approach to generate tunable two-color synchronized ultrashort laser pulses. The output energy from these two-color ultrafast Ti:sapphire oscillators have been amplified by two-color ultrafast Ti:sapphire laser amplifiers. The extent of amplification of the ultrashort laser pulses in the Ti:sapphire laser amplifiers is limited with detrimental effects such as crystal damage, Kerr lensing, and self phase modulation. The chirped pulse amplification technique [55] has been used successfully to safely amplify the two-color ultrashort laser pulses in the two-color ultrafast Ti:sapphire laser amplifiers to the pulse energy up to 15 mJ with a pulse repetition rate of 10 Hz [51]. A wavelength separation up to 120 nm has been realized from these two-color ultrafast Ti:sapphire amplifier systems [53].

2.4.3 Limitations with the output power from Ti:sapphire lasers

The average output power from conventional Ti:sapphire oscillators and Ti:sapphire laser amplifiers is in the order of several watts [56, 57]. This is mainly because of the limitations with the power of pump lasers and more importantly with thermal lensing problem.

Pumping the Ti:sapphire is efficiently achieved by green lasers such as argon lasers (514 nm) or frequency-doubled Nd:YAG lasers (532 nm) and more recently by frequency-doubled Yb:fiber lasers [58]. The conventional laser sources of these types have an output power of several tens watts. Thermal lensing is the result of the temperature gradient induced by the absorbed pump laser. In fact, due to a large quantum defect, while pumping with the green lasers a substantial amount of heat is generated in the Ti:sapphire crystal. For example, for pumping at 532 nm and lasing at 800 nm, the quantum defect is 33%. As a result, a temperature gradient is created from the Ti:sapphire crystal axis toward the outer crystal surface where it has contact with its ambient environment. The temperature gradient induces a refractive index gradient resembling a lens-like medium which focuses the laser beam into the Ti:sapphire crystal axis. The focused pump laser does not pump the whole Ti:sapphire crystal, and therefore, the pumping efficiency will decrease and in severe cases the Ti:sapphire crystal will damage [57].

For Ti:sapphire lasers, thermal lensing puts a 7-watt limit on the pump power at room

temperature [56]. An average power of 2 W for the 10-KHz 160-fs laser pulses has been reported from a Ti:sapphire regenerative amplifier at room temperature [59]. In order to increase the pump power limit of the thermal lensing effect, some other techniques such as cryogenic cooling have been used. Yang and Walker achieved an average power of 9.4 W of 2-KHz, 46-fs laser pulses from a liquid-nitrogen-cooled Ti:sapphire laser in a ring resonator setup while pumping at 30 W. More recently, Matsushima *et al.* have reported an average power of 26 W of 10-KHz, 58-fs-FWHM laser pulses from a single-stage Ti:sapphire amplifier by incorporating 180-W pump power from two frequency-doubled Nd:YAG lasers and using the Yang-Walker's ring resonator scheme at liquid nitrogen temperature [60].

In conclusion, Ti:sapphire as a laser gain medium offers a broad gain bandwidth to simultaneously amplify two-color laser pulses with a large wavelength separation. However, Ti:sapphire laser systems are limited to a watt-level output average power. One must use expensive high-power green lasers as well as cryogenic cooling systems to achieve several ten-watt output power. In comparison, YDFA as a laser amplifier has a narrower gain bandwidth but it is superior in terms of average power.

2.5 Short-pulse mid-infrared generation

Difference frequency generation, optical parametric oscillation (OPO), optical parametric generation (OPG), and optical parametric amplification (OPA) are four routinely used techniques to generate tunable short-pulse MIR radiations where ultrafast lasers are not available or a wide tunability is desired [61]. From these techniques, MIR radiation is generated from frequency down conversion process where three optical pulses of pump, signal, and idler with frequencies ω_p, ω_s, and ω_i, respectively, are interacting with each other in a $\chi^{(2)}$ nonlinear crystal, where $\omega_p > \omega_s > \omega_i$. The process is a result of the induced second order polarization $P^{(2)}$ oscillating with a frequency of $\omega_p - \omega_s$ [61]

$$P^{(2)}(\omega_p - \omega_s) = 4\epsilon_0 \, d_{\text{eff}} \, E_p \, E_s, \tag{2.1}$$

where ϵ_0 is the permittivity of the free space, d_{eff} is the effective 2nd-order nonlinear optical susceptibility, and E_p and E_s are, respectively, the magnitudes of the pump and signal optical fields. From energy conservation, a simple relation is hold among the frequencies of the three optical fields [61]

$$\omega_i = \omega_p - \omega_s, \tag{2.2}$$

From Eq. 2.2, the process can be understood from the virtual-energy-level description whereas by absorption one photon with a frequency ω_p, one atom is excited to the highest

virtual energy level [61]. Between the ground state and the highest virtual level, it is assumed another virtual energy level through which the excited atom decays from the highest virtual level to the ground state in a two-step process resulting in the emission of signal and idler photons. This decaying process is stimulated by the presence of the signal photons. Thus, for the idler frequency takes place in the MIR range, one needs to tune the frequencies of the pump or signal fields appropriately.

For the three interacting optical fields, the wavevector mismatch Δk under collinear condition is given by [61]

$$\Delta k = k_p - k_s - k_i, \tag{2.3}$$

where k's are the magnitude of corresponding wavevectors of the optical fields. In the plane wave approximation, for the energy extraction takes place most efficiently, the three waves have to be phase matched that means $\Delta k = 0$ [61]. Now, the energy is transfered efficiently from the pump optical field to the signal and idler optical fields, otherwise, the energy would be exchanged back and forth to the pump optical field. Substituting $k = n\omega/c$ into Eq. 2.3, the perfectly phase matching under collinear condition for the plane waves is given by [61]

$$n_i\,\omega_i = n_p\,\omega_p - n_s\,\omega_s, \tag{2.4}$$

where n's represent the frequency-dependent index of refraction of the NLO crystal for the three optical fields. For ordinary optical materials and in the normal dispersion regime, refractive index increases as the frequency increases. In this case, the perfect phase matching condition from Eq. 2.4 cannot be satisfied [61]. However, for example birefringent NLO crystals can used to achieve the phase matching condition. In a birefringent crystal, the refractive index is dependent on the polarization of the incident beam. Under proper orientation of the crystal respect to the polarized pump and signal beams, the refractive indices are adjusted so that the three interacting fields are perfectly phase matched.

2.5.1 Phase matching in GaSe

The GaSe crystal has been used for second harmonic generation [62, 63], sum frequency generation [63], and difference frequency generation [38,39,52,64,65]. The GaSe crystal belongs to the point group 6m2 crystals [62]. It has only one non-zero second-order nonlinear optical coefficient d_{22} with a value of 54 pm/V [63]. The large second-order nonlinearity, a broad transparency rage of 0.65-20 μm [62, 63], and a large birefringent ($\Delta n \sim 0.35$) [66] (useful for the angle phase matching) make the GaSe crystal an attractive NLO crystal. On the negative side, the large birefringent of the GaSe crystal causes a large walk-off angle of $\sim 3.6^\circ$ resulting to a large walk-off distance of 63 μm/mm, i.e. the extraordinary beam

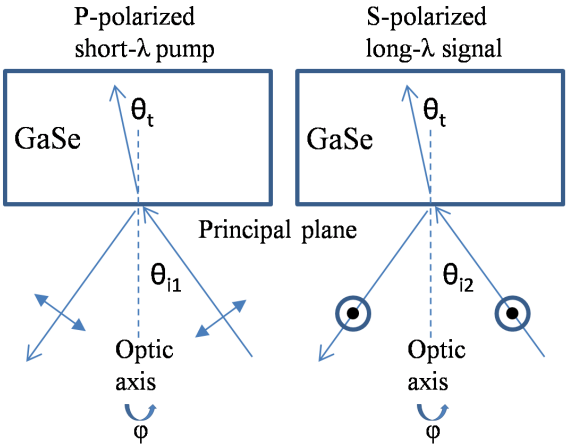

Figure 2.2: Top view of GaSe crystal and the polarizations of the pump and signal pulses respect to the principal plane. The phase matching angle is θ_t for both waves. The external angles θ_{i1} and θ_{i2} are slightly different. The azimuthal angle is ϕ. The p-polarized beam is the e-beam and the s-polarized beam is the o-beam.

becomes separated from the ordinary beam by 63 μm from a 1-mm-thick crystal. This dramatically decreases the interaction length for mixing tightly-focused pump and signal beams.

For a birefringent crystal, the crystal's refractive indices are classified into ordinary refractive index n_{o} and extraordinary refractive index n_{e} whereas n_{o} is independent from θ but for the e-beam $n_{\mathrm{e}}(\theta)$ is a function of θ according to [61]

$$\frac{1}{n_{\mathrm{e}}^2(\theta)} = \frac{\sin^2(\theta)}{n_{\mathrm{e}}^2} + \frac{\cos^2(\theta)}{n_{\mathrm{o}}^2}, \tag{2.5}$$

where θ is the angle between the optic axis and the refracted beam in the crystal (shown as θ_t in Fig. 2.2), n_{e} is the wavelength-dependent principle value of the extraordinary refractive index and n_{o} is the wavelength-dependent ordinary refractive index.

For the GaSe crystal, two types of phase matching are realized by angle tuning [62, 63]. Type-I phase matching is achieved for the polarization orientations of the high frequency pump, low frequency signal and idler radiations being (eoo) respectively and type-II phase matching is achieved for the polarization orientations being (eoe) respectively where (e) denotes the p-polarization and (o) denotes the s-polarization according to Fig. 2.2. In both phase matching types, the polarizations of the pump and signal pulses are perpendicular. By rotating the crystal about the axis perpendicular to the principal plane (the plane

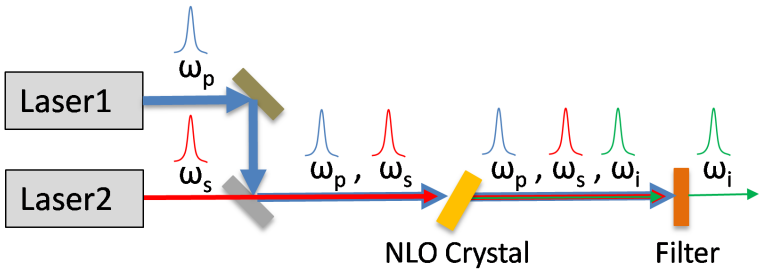

Figure 2.3: Schematic of an ultrafast DFG-based MIR generation setup.

containing the optic axis and wavevector of the incident beam), the value of $n_e(\theta)$ from Eq. 2.5 for the high-frequency pump pulses in the type-I phase matching and for the high-frequency pump pulses as well as the idler pulses in the type-II phase matching is adjusted such that the phase matching equation 2.4 is satisfied.

2.5.2 DFG-based short-pulse mid-infrared generation

Fig. 2.3 depicts the schematic of the setup for the generation of ultrafast DFG-based MIR pulses under the collinear condition. From this figure, synchronized ultrafast pump and signal laser pulses with frequencies ω_p and ω_s are focused into a nonlinear optical (NLO) crystal. The pump and signal laser pulses can be the output from two-color ultrafast laser systems such as two-color ultrafast YDFA systems [38, 39] and two-color ultrafast Ti:sapphire laser systems [52, 64]. Also, the signal and idler pulses from optical parametric oscillators have been difference frequency mixed [65, 67]. The pump and signal optical beams have to be spatially overlapped in the NLO crystal. This is achieved by perfectly aligning the two laser beams. Also, the pump and signal pulses have to be overlapped in time in order to interact efficiently. This is usually achieved by using a variable delay line (for example a movable mirror) in the optical path of one of the pump or signal pulses. When the phase matching condition for the pump, signal and idler frequencies is fulfilled, for example by rotating the NLO crystal, the pump and signal fields can be difference frequency mixed resulting in the generation of the idler pulses with the frequency ω_i. After the NLO crystal, a long-wave-pass infrared filter such as germanium plate is used to filter out the pump and signal frequencies. By tuning the pump and/or signal frequencies appropriately and rotating the NLO crystal, tunable ultrafast MIR pulses can be generated.

2.6 DFG-based short-pulse mid-infrared generation from two-color ultrafast YDFA systems

Difference frequency generation as a proven technique for the generation of the MIR wavelengths offers a practical approach to produce tunable short MIR pulses. By frequency mixing of the two-color output from two-color ultrafast YDFA systems, MIR pulses have been reported [38, 39].

From these laser systems, Romero *et al* reported short MIR pulses at 18 μm with an average power of 20 μW by difference frequency mixing of the two-color pulses centered at 1038 nm and 1103 nm in a 1-mm GaSe crystal [38] and Al-kadry and Strickland reported picosecond MIR pulses at 17.5 μm with an average power of 400 μW by difference frequency mixing of the two-color pulses centered at 1038 nm and 1105 nm with a combined average power of 280 mW in a 1-mm GaSe crystal [39].

2.7 Tunable DFG-based short-pulse mid-infrared generation from ultrafast Ti:sapphire laser systems

Synchronized two-color ultrafast Ti:sapphire laser systems have been used for the generation of tunable ultrashort MIR pulses using DFG technique. Here, two systems will be reviewed for the generation of the long-wavelength range of the "molecular fingerprint" which can be compared with the MIR results from the two-color ultrafast YDFA system.

In 1998, Kaindl *et al* reported tunable ultrashort mid-IR pulses in the 9-18 μm with a maximum average power of 1 μW at 15 μm by focusing broadband 20-fs laser pulses centered at 830 nm from a Ti:sapphire oscillator with a 88-MHz repetition rate and an average power of 100 mW into a 1-mm-long GaSe crystal [64]. The authors difference frequency mixed the different spectral components of the ultrashort Ti:sapphire pulses by the angle-tuning phase matching technique and achieved up to 0.02% photon conversion efficiency. Kaindl reported a 140-fs pulse duration for MIR pulses centered at 11.5 μm.

In 2002, Fraser *et al.* achieved tunable short MIR pulses in the wavelengths 10-20 μm with a pulse duration less than 1 ps by direct difference frequency mixing ultrashort laser pulses from a two-color ultrafast Ti:sapphire regenerative amplifier operated at 500 Hz in a GaSe crystal [52]. The authors achieved as high as 0.6-μJ pulse energy (equivalent to 300 μW average power) from MIR pulses near 14 μm after difference frequency mixing the 600-μJ ultrashort two-color pulses in a 3-mm-long GaSe crystal.

2.8 Tunable DFG-based short-pulse mid-infrared generation from ultrafast OPO systems

In an ultrafast OPO system, an intense pulsed laser is injected into an OPO cavity [68]. After interaction of the pump laser with the in-cavity NLO crystal, the signal and idler pulses are generated. The cavity may be resonant at a) signal, b) signal+idler, or c) signal+pump resulting in the amplified signal pulses. The pump laser will be more depleted by the amplified signal pulses resulting in the generation of intensified idler pulses. By continuously tuning the OPO cavity length so that being resonant at signal frequency and synchronized with the pump pulse train as well as by satisfying the phase matching condition in the NLO crystal, tunable short-pulse MIR radiation is generated.

The OPO technique is favorable for the generation of high-average-power pulses in the MIR wavelengths < 5 μm [69]. The MIR tunability range is limited to the above range because of the transparency range of suitable NLO crystals and bandwidth of the optical mirrors of the resonator. Quasi phase matching (QPM) crystals such as periodically poled lithium niobate (PPLN) are favorable NLO crystals in the OPO systems because of offering a large nonlinear response and not being selective to the propagation direction [68]. The transparency range of the PPLN lies between 0.33 and 5 μm. Currently, the QPM NLO crystals with a broader MIR range are not available commercially [70].

However, the signal+idler output pulses from ultrafast OPO systems have been used in the DFG technique in order to generate the long-wavelength range of the "molecular fingerprint". From the OPO-DFG systems, Fraser *et al.* reported subpicosecond MIR pulses tunable between 8 and 18 μm with an average power of 1 μW from a 1-mm-thick $AgGaSe_2$ crystal [67] as well as Ehret and Schneider achieved subpicosecond MIR pulses tunable between 5.2 and 18 μm with an average power of ~ 100 μW in the wavelengths 16-18 μm from a 1-mm GaSe crystal [65].

In conclusion, although short-pulse MIR radiation with a broad tunability has been generated from two-color ultrafast Ti:sapphire laser systems as well as OPO-DFG systems, from the two-color ultrafast YDFA systems the average power at the very long-wavelength MIR radiation is noticeably higher. More, the average power of the two-color YDFA systems can be increased by incorporating high-power YDFA systems to scale up the MIR power.

2.9 Tunable short-pulse mid-infrared generation from OPG and OPA systems

In an ultrafast OPG system, an NLO crystal is pumped by laser short pulses [71]. The signal and idler optical pulses are generated when phase matching condition is satisfied. The signal optical pulses are generated in the very beginning of the process and then amplified in the presence of the pump laser pulses as they propagate and interact in the NLO crystal. As a result, the idler optical pulses are intensified too. However, the idler is still weak. In the OPG technique, the threshold pump power is high because of the absence of the input signal and that can be close to the surface damage threshold of the NLO crystal. For example from an OPG system pumped by 100-ps pulses at 2.8 μm, the threshold pump intensity has been demonstrated as high as 1.1 GW/cm^2 for a 1.4-cm-long GaSe [66] while the damage threshold intensity of GaSe has been demonstrated to occur at 7 GW/cm^2 for 70-ps laser pulses [72]. From an OPG setup, Vodopyanov demonstrated short-pulse, 3-Hz, MIR radiation in the wavelengths 3.3-19 μm using a 14-mm-long GaSe crystal with a typical photon conversion efficiency of 10% [66].

In an ultrafast OPA system, the output from a short-pulse intense laser such as Ti: sapphire is divided into two or more branches [69]. One pump laser beam with a smaller power is used to generate a seed signal of the kind of either super-fluorescence or white light. The super-fluorescence is generated from the same process as in the OPG using an NLO crystal such as β-barium borate (BBO) and the white light is generated through self phase modulation by focusing the short-pulse intense laser beam into a glass medium such as sapphire. In the next stage, the seed signal is preamplified by the parametric amplification process in an NLO crystal which is pumped by the second pump pulses. Then, the preamplified signal may be sent into a main optical parametric amplifier pumped by the third pump pulses. In all amplifiers, the pump laser, signal and idler optical fields are phase matched. Finally, the pump, signal, and idler optical beams are separated by dichroic mirrors or filters and an optical compressor may be used for compressing the output pulses. Rotermund and Petrov have reported 200-fs, microjoule-level, 1-kHz (milliwatt-level average power) pulses in the wavelengths 5-9 μm [73].

In conclusion, the OPG technique offers a tunability range for the MIR pulses as broad as DFG technique, however, the MIR output power is lower because of the absence of the input signal pulses. From the OPA technique, the tunability range for the MIR pulses is not as broad as the DFG technique due to the spectral bandwidth of the optical elements. One has to replace the optical elements to switch to different wavelength ranges. Overall, the DFG technique has been proven to be a practical method for the generation of widely

tunable ultrashort MIR pulses with a moderate average power in the milliwatt level.

2.10 Quantum cascade lasers

Quantum cascade laser (QCL) was invented by J. Faist, F. Capasso and colleagues in 1994 [74]. Quantum cascade laser is one kind of semiconductor laser with an emission wavelength located in the spectral region of MIR to terahertz radiations. Quantum cascade laser is engineered by constructing multi-quantum-well structure and quantized energy levels buried in the quantum wells by stacking several nanoscopic scale layers from varying semiconductor materials [75]. The quantized energy levels are formed in conduction band of the chosen materials making possible intersubband transitions for the generation of narrow linewidth MIR radiation. By varying the thickness of the layers, the energy levels are engineered. In QCLs, there is only one type of charge carrier, i.e. electron, in contrast with semiconductors. Upon applying current, the electron travels perpendicular to the layers and tunnels to the quantum wells which accompanies with an intersubband transition and emission of a photon. A single electron can generate many photons in a cascading fashion by tunneling into stacking quantum wells. Laser action in QCLs is typically realized from a three-level energy structure [75]. In order to achieve population inversion and laser action, life time of the energy levels is engineered to obtain a laser upper energy level with a longer life time.

Quantum cascade lasers have been developed for their vast commercial applications such as remote gas sensing and MIR spectroscopy. A MIR wavelength range between 3 μm and 16 μm at room temperature has been demonstrated from QCLs [76]. Generally, the linewidth of conventional QCLs is narrow because of the intersubband transition [77]. Currently, constructing widely tunable single-mode QCL is an active area of research. For this, there are two main requirements: to achieve broadband QCLs and to implement a method to tune the output radiation over the gain spectrum. One may take a technological path involving in incorporating different cascade designs to achieve a broad gain spectrum in the MIR spectral range. Hugi *et al.* incorporated five cascades and achieved a widely tunable MIR wavelength range between 7.6 μm and 11.4 μm (a 432-cm^{-1} tuning range) with an average power of 15 mW at room temperature [78]. Each of five active cascade regions had a different gain peak which was continuously tailored to the gain spectrum of the next active cascade region resulting in a "gap-free tunable QCL". Authors used an external cavity (EC) setup in the "Littrow" configuration for tuning the output wavelength. The EC configuration is the most popular method for tuning the laser wavelength in widely tunable single-mode QCLs [77]. In the Littrow-configuration EC-QCL, the laser cavity is

constructed between the back surface of QCL and a grating at the Littrow angle. An anti-reflection collimating lens is used between QCL and the grating. At the Littrow angle, the first-order diffraction returns to the laser gain medium and the zero-order diffraction is the laser output. By angle-tuning the grating, a tunable laser is achieved.

Achieving mode-locked pulses from MIR QCLs is a challenging task mainly because of picosecond time scale of gain recovery time as a result of the fast optical phonon scattering process [79]. Consequently, cw operation becomes a dominant process in most QCLs. In 2009, Mode-locked MIR pulses with a FWHM of 3 ps were generated from a liquid-nitrogen-cooled QCL by increasing the relaxation time of intersubband transitions [79]. This was achieved by gain modulation of the QCL at a RF frequency to suppress the lasing.

In conclusion, quantum cascade lasers are the state-of-art compact size coherent MIR sources. Currently, the tunability range of a single MIR QCL is not as abroad as that achieved from nonlinear frequency down conversion processes such as DFG. More, mode-locked MIR QCLs are not abundant mainly because of the fundamental problem of the fast gain recovery time. Therefore, the generation of widely tunable short-pulse MIR radiation from DFG technique such as that presented in this thesis remains as a current technological solution for the applications such as ultrafast MIR spectroscopy.

2.11 Chirped pulse amplification

In 1985, chirped pulse amplification technique for ultrafast laser amplifiers was invented by Strickland and Mourou to amplify ultrashort laser pulses to high peak powers [55]. In the CPA technique, ultrashort laser pulses are temporally stretched to laser pulses with longer durations (more than tens of picoseconds) after traversing dispersive elements such as prisms, gratings, and optical fibers. The spectral components of a stretched laser pulse travels one after another based on group delay dispersion (GDD) in the stretcher from chromatic dispersion [80, 81]. The GDD in the prism and grating pulse stretchers is a result of optical path difference between spectral components of the pulse. The GDD in optical fibers is a result of the refractive index change with wavelength thereby the spectral components of the pulse travel at different speeds. The stretched laser pulses have now lower peak powers and can be safely amplified in laser gain media before nonlinear detrimental effects such as absorption-induced crystal damage, Kerr lensing, and self phase modulation take place. In the realm of fiber CPA, the laser pulses are stretched to avoid the SPM on the laser pulses as well as to prevent the absorption-induced damage to the fiber. Due to very small core area of a single mode fiber, even with moderate average-power laser pulses, the laser peak intensity is very high in the fiber core. In the SPM effect, the

intense laser pulses acquire nonlinear pulse broadening through Kerr effect which makes it difficult to be recompressed to the initial pulsewidth. After amplification in the laser gain media, the laser pulses are compressed using gratings or prisms in a reciprocal manner [82]. In a two-color CPA system, one may use separate laser pulse stretchers and separate laser pulse compressors for each color to have a better control on the laser pulses at each color.

2.12 Chirped laser pulses

Laser pulses are electromagnetic wave-packets [83]. The magnitude of the electric field in the pulse envelope varies with time. The temporal dependence of the electric field of the pulse in the complex from is described by [83]

$$E(t) = A(t)\, e^{i\phi(t)}, \tag{2.6}$$

where $A(t)$ is the time-dependent electric field amplitude and $\phi(t)$ is the time-dependent phase function.

From Fourier transform theory, a laser pulse consists of oscillating electromagnetic waves of different frequencies. The constituting frequencies form a continuum around a central frequency called carrier frequency. For a laser pulse that all the constituting frequencies travel simultaneously, the laser pulse is known as an unchirped laser pulse. For a laser pulse that the constituting frequencies travel one after another, the laser pulse is known as a chirped laser pulse. For the frequency components spread along the chirped pulse envelope, the pulse is stretched in time decreasing the peak power. This can be readily understood from the fact that the pulse energy E is constant and the P_{peak} decreases by increasing the pulsewidth t from $P_{peak} = E/t$.

The variations of the phase function of the laser pulse with time gives us useful information about the time-dependent instantaneous frequency of the laser pulse. The time-dependent instantaneous frequency of the laser pulse is obtained by the time derivative of the phase function [83]

$$\omega(t) = \frac{d\phi}{dt}. \tag{2.7}$$

For unchirped laser pulses, the phase function changes linearly with time such that $\phi(t) = \phi_0 + \omega_0\, t$ where ω_0 is the constant carrier frequency. Thus, the instantaneous frequency ω_0 (using Eq. 2.7) is constant along the pulse envelope for the unchirped laser pulses. For the chirped laser pulses, the phase function can be any arbitrary function of time. In the realm of stretching and compressing laser pulses, the special interest is on the

quadratically time-dependent phase function in the sort of $\phi(t) = \phi_0 + \omega_0\, t + a\, t^2$ resulting to linearly-chirped laser pulses. For the linearly chirped laser pulses, the instantaneous frequency changes linearly along the pulse envelope (using Eq. 2.7, $\omega(t) = \omega_0 + 2\, a\, t$). The instantaneous frequency along the pulse envelope increases for the positive-chirped laser pulses and that decreases for the negative-chirped laser pulses.

From Fourier transform theory, the product of pulse duration and spectral bandwidth is minimum for unchirped laser pulses. For this, the unchirped laser pulses are usually called Fourier transform limited laser pulses and have the minimum pulsewidth. For Fourier transform limited Gaussian laser pulses with a spectral bandwidth of $\Delta\nu$ and a pulsewidth of Δt, the product of the two quantities is 0.441 [83]

$$\Delta\nu\, \Delta t = 0.441. \tag{2.8}$$

It is proved that for a quadratically time-dependent phase function, the phase function in the frequency domain is a quadratic function as well [83]. Now, the phase function in the frequency domain is expanded in a Taylor's series up to the 2nd order

$$\phi = \phi_0 + \left.\frac{d\phi}{d\omega}\right|_{\omega_0} \Delta\omega + \frac{1}{2}\left(\left.\frac{d^2\phi}{d\omega^2}\right|_{\omega_0} \Delta\omega\right) \Delta\omega, \tag{2.9}$$

where the first derivative is the time of flight of the oscillating electromagnetic wave with the frequency component ω_0 after traveling a distance L in a dispersive system and $\frac{d^2\phi}{d\omega^2}|_{\omega_0}\Delta\omega$ is the time delay between two waves with a difference frequency of $\Delta\omega$ after traveling the distance L. The group delay dispersion is another name for the 2nd derivative of the phase function, that is

$$\text{GDD} = \frac{d^2\phi}{d\omega^2}. \tag{2.10}$$

For initially Fourier transform limited laser pulses, the pulse broadening for the pulses traveled in a dispersive system and acquired chirp is approximated by [83]

$$\Delta\tau = \text{GDD}\, \Delta\omega. \tag{2.11}$$

In this thesis, for the sake of simplicity, Eq. 2.11 have been used for the calculations of pulse broadening and pulse compression of initially chirped laser pulses in the pulse stretcher and pulse compressor.

In the field of fiber optics, $\Delta\tau$ is conveniently calculated from [84]

$$\Delta\tau = D\, \Delta\lambda\, L \tag{2.12}$$

where $\Delta\lambda$ is the spectral bandwidth in terms of wavelength, L is the propagation distance and D is dispersion coefficient and is given by [84]

$$D = -\frac{\lambda}{c}\frac{d^2n}{d\lambda^2} \tag{2.13}$$

which is a measure of the pulse spreading. In this thesis, Eqs. 2.12 and 2.13 have been used in order to find the amount of pulse broadening in optical fibers. In Eq. 2.13, the wavelength-dependent refractive index of silica optical fiber n can be replaced by an empirical equation that can be found in many handbooks and textbooks such as Ref. [84].

To relate the GDD to the dispersion coefficient D, we substitute $\Delta\omega$ from

$$\Delta\omega = -2\pi c\frac{\Delta\lambda}{\lambda^2} \tag{2.14}$$

into Eq. 2.11 and equate Eq. 2.11 to Eq. 2.12, thus the GDD is given by

$$\text{GDD} = \frac{-\lambda^2}{2\pi c}\, D\, L. \tag{2.15}$$

In this thesis, Martinez setup has been used to stretch the laser pulses [81]. The Martinez pulse stretcher consists of a 1:1 telescope placed between two anti-parallel gratings to impose positive GDD on the laser pulses. The telescope consists of two similar lenses sharing the focal plane. The two gratings are placed within the focal distance of the lenses outside the telescope. The positive GDD from the Martinez pulse stretcher using transmission gratings under "the ideal paraxial wave-propagation conditions and negligible dispersion of the lens material" is given by [81, 85]

$$\text{GDD} = \frac{\lambda_0^3}{\pi c^2 d^2 \cos^2\theta_d}(2f - s_1 - s_2), \tag{2.16}$$

where λ_0 is the central wavelength of the pulse, c is speed of light in vacuum, d is the grating period, θ_d is the diffraction angle, f is the focal length of the gratings, s_1 is the distance between the first grating and the first lens, and s_2 is the distance between the second grating and the second lens. In this equation, a factor of 2 has been included in the original equation for a double transmit. After the second grating, the laser pulses are laterally expanded depending on the bandwidth of the laser pulses. In a double transmit setup, the frequency components of the laser pulses are collimated back to the input beam size after a retroreflection from a flat mirror.

In this thesis, Treacy setup has been used to compress the laser pulses [82]. The Treacy pulse compressor consists of two parallel gratings to impose negative GDD on the laser pulses. The GDD for the transmission grating pulse compressor is given by [82, 85]

$$\text{GDD} = \frac{-\lambda_0^3 L}{\pi c^2 d^2 [1 - (\frac{\lambda_0}{d} - \sin\theta_i)^2]^{3/2}} \tag{2.17}$$

where λ_0 is the central wavelength of the pulse, L is the pulse compressor length, c is speed of light in vacuum, d is the grating period, and θ_i is the incident angle to the grating. Again, a factor of 2 has been included in the original equation for a double transmit for a retroreflection configuration in order to remove the lateral beam expansion.

2.13 Two photon absorption

In two photon absorption (TPA) process, two photons of the same wavelength are absorbed simultaneously or sequentially along the absorption gap of an atomic system and it arises from the imaginary part of the third-order nonlinear susceptibility [61]. Note that, in general, an optical absorption is related to the imaginary part of the optical susceptibility of the medium. The TPA process is a nonlinear process therefore the absorption rate scales with the product of the intensities of the incoming fields interacting in the medium that is the square of the laser intensity. This is similar to second harmonic generation (SHG) because two same photons are involved from the same laser. For this, the TPA process becomes efficient with high intensity lasers. On the other hand, the TPA process does not require phase matching condition because only two fields are interacting unlike the SHG or DFG processes where three electromagnetic fields are interacting. To avoid the TPA process in the DFG-based MIR generation, the two pumping wavelengths have to be more than double of the band gap wavelength λ_{gap} of the nonlinear optical crystal [61, 86]. For other wavelengths close to the $2\lambda_{\text{gap}}$, the intensity threshold of the laser beam for the TPA to get started increases as the laser wavelength increases. With the YDFA operated at the wavelengths $\gtrsim 1$ μm we obtain a higher TPA intensity threshold compared with the Ti:sapphire lasers operated at the wavelengths $\gtrsim 0.8$ μm.

2.14 Supercontinuum generation

In this method, the broadband spectrum from a mode-locked laser is further broadened into a spectrum called "supercontinuum" by injecting short laser pulses into a photonic crystal

fiber [87]. The supercontinuum is generated through the nonlinear effect from interaction of the intense short laser pulses with the fiber because the light is tightly confined by the PCF structure. A supercontinuum generated in this way can be used in many applications such as ultrashort pulse generation through pulse compression [88] and two-color ultrafast YDFA system [37–39]. In a two-color ultrafast YDFA system, a supercontinuum is sliced into two short-pulse colors and will be used as a two-color seed source in the system.

A standard fiber mainly consists of core, cladding, and a protective coating. The refractive index of the core is larger than that of the cladding resulting in guiding light through internal reflection. A single-mode optical fiber is engineered to guide only the fundamental mode by adjusting the core size and refractive indices of the core and cladding in the manufacturing stage. A new class of optical fibers called photonic crystal fibers are engineered by implementing air holes running all along the fiber to achieve: single-mode guiding property over a broad range of wavelengths, controlled dispersion behavior, and excellent mode confinement. These properties yield to the enhancement of nonlinearity in PCFs [87]. Generally, a supercontinuum is a continuous spectrum that can be generated by interaction of intense laser pulses with various materials through nonlinear optical processes such as self phase modulation, cross phase modulation, four wave mixing, and Raman scattering [87]. For the supercontinuum generation be effective, an optical fiber is preferred for its guiding property and offering a large interaction length. In highly nonlinear PCF with a solid core surrounded by air holes, a propagating mode is confined in a smaller effective area (usually by two orders of magnitude) compared with standard fiber resulting in an increased intensity in the fiber [87]. A tighter mode confinement is achieved because of a large contrast between the refractive index of the core and cladding due to the implemented air holes in the cladding. The increased intensity will result in enhancement of the nonlinear optical processes. For this, using highly nonlinear PCF for the generation of supercontinuum requires pulse energies noticeably small [87]. In this thesis, injecting nanojoule energy laser pulses from the output of a 200-mW, 200-fs, 50-MHz, 1030-nm fiber laser into a 2-m PCF has resulted in the generation of a supercontinuum extended from 950 nm to 1150 nm.

2.15 Polarization maintaining YDFA

Even a perfectly circular optical fiber contains some randomly distributed birefringent islands along the fiber due to for example randomly distributed local mechanical stress/tension forces. Thus, for a linearly polarized optical beam, the polarization plane changes randomly as the beam propagates in the fiber core. One practical way to maintain the polarization

of the beam in the fiber core is to introduce a strong mechanical stress force along the fiber core to create a strong birefringence which is not affected very much by the randomly distributed birefringence. This is usually performed by including two glass rods in the fiber cladding. The glass rods are from different material compared to the fiber cladding and they are aligned on the opposite sides of the fiber core. Fig. 2.4 depicts a Panda structure of the DC-YDFA used in this thesis. For a linearly polarized beam launched into the fiber core, the polarization will be preserved when the polarization of the beam is aligned with one of the birefringent axes shown with arrows in Fig. 2.4. The polarization of the light launched into the fiber is preserved based on the eliminated mode coupling between two polarization modes of the sort of LP_{01x} and LP_{01y} in the fiber core due to a large difference between the propagation constants of the two polarization modes [84]. Using the PM YDFA is beneficial as it reduces the optical loss from polarization-dependent optical elements such as Faraday isolators, gratings, prisms, and so on.

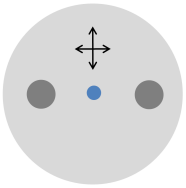

Figure 2.4: The Panda structure of the polarization maintaining DC-YDFA.

2.16 Theory and modeling

The rest of this chapter is organized as follows. Sections 2.16.1 to 2.16.4 provide a mathematical background on the amplification of a laser beam in the Yb:fiber as a laser amplifier based on existing laser theory. Sections 2.17 to 2.17.2 specify the Yb:fibers modeled in this research. Sections 2.18 to 2.18.1 explain the approach which has been taken for modeling of amplification of a two-color spectrum in the Yb:fiber amplifier system. Section 2.19 explains a LabVIEW program which has been created in this research for the simulation of the two-color YDFA system based on the modeled equations.

2.16.1 Effective absorption and emission cross sections of Yb^{3+} in Yb:fibers

For the energy states of Yb^{3+} in crystalline structures, there have been assigned a ground state $^2F_{7/2}$ manifold of four Stark sub-levels and an excited state $^2F_{5/2}$ manifold of three Stark sub-levels under a symmetrical crystal field of neighboring ions (see Appendix A.1). For the Yb^{3+} in the silica fiber, the sub-level energy states in each manifold are not sharp but they become broadened under an asymmetrical crystal field due to amorphous structure of the silica fiber. The broadened sub-level energy states in the ground state and excited state manifolds constitute two energy bands. This reduces the ytterbium silica system to a two-level system. For this, effective emission and absorption cross sections are assigned to the two energy bands.

The effective absorption cross section is the probability of absorption of one photon by one ion. Similarly, the effective emission cross section of an ion is a measure of the probability of stimulated emission of a photon. These effective cross sections are not necessarily equal but they are related to each other. A relation between the two cross sections is very helpful when one of which is available as well as when extrapolation of the cross sections is necessary. These concepts will be discussed in this section and will be applied to the Yb:fiber amplifier.

Generally speaking, the absorbed power P_{abs} by one ion is proportional to the intensity I incident upon it. For a two-level energy system and when the incident intensity is low, P_{abs} is given by $P_{abs} = \sigma_a I$ up to the first order where σ_a is the effective absorption cross section for transition from a ground state labeled by 1 to an excited energy level labeled by 2 for one ion. Obviously, for N_1 identical ions, the absorbed power can be written [14]

$$P_{abs} = N_1 \sigma_a I. \tag{2.18}$$

For a two level system , the rate equation for the change in the population of the ground state N_1 due to the absorption is obtained from dividing Eq. 2.18 by $h\nu$ where h is the Planck constant and ν is the photon frequency

$$\left.\frac{dN_1}{dt}\right|_{abs} = -\sigma_a \frac{I}{h\nu} N_1, \tag{2.19}$$

where the negative sign is for the depletion of ions in the energy level 1 due to the absorption. Equation 2.19 is also written in the form

$$\left.\frac{dN_1}{dt}\right|_{abs} = -B_{12}\rho N_1, \tag{2.20}$$

where ρ is the energy density of photons per unit volume and B_{12} is the Einstein B coefficient that gives the absorption rate. From Eqs. 2.19 and 2.20 and invoking $I = \rho c$ where c is the speed of light in vacuum, we obtain the relation

$$\sigma_a = \frac{h}{\lambda} B_{12}, \tag{2.21}$$

where λ is the wavelength of the absorbed photon. Similar equations are obtained for the stimulated emission

$$\frac{dN_2}{dt}_{em} = -\sigma_e \frac{I}{h\nu} N_2. \tag{2.22}$$

$$\frac{dN_2}{dt}_{em} = -B_{21} \rho N_2, \tag{2.23}$$

$$\sigma_e = \frac{h}{\lambda} B_{21}. \tag{2.24}$$

From Eqs. 2.21 and 2.24 and under thermodynamic equilibrium we have $B_{12} = B_{21}$ resulting to $\sigma_e = \sigma_a$. However, this relation is not valid when the ground and excited states include sub-energy states.

For an ion with degenerate energy states, when the degeneracy is lifted by some interactions such as the crystal field interaction in Yb:fibers (see Appendix A.1 for more details), the rate equations for the absorption and stimulated emission are given by [14]

$$\frac{dN_1}{dt}_{abs} = -\sum_{m_1,m_2} R^{(a)}_{m_1 m_2} N_{m_1}, \tag{2.25}$$

$$\frac{dN_2}{dt}_{em} = -\sum_{m_1,m_2} R^{(e)}_{m_2 m_1} N_{m_2}, \tag{2.26}$$

where m_1 and m_2 indicate, respectively, the sub-level indices in the ground state manifold and the excited state manifold, and R is the transition rate between the sub-levels in each manifold.

For equally populated sub-levels in the given manifolds, we have $N_{m_1} = N_1/g_1$ and $N_{m_2} = N_2/g_2$ where g_1 and g_2 are respectively the degeneracy of the ground state and excited state manifolds. Moreover, assuming that the transition between the two channels $m_1 \to m_2$ is reciprocal, *i.e.* $R^{(a)}_{m_1 m_2} = R^{(e)}_{m_2 m_1}$, Eqs. 2.25 and 2.26 are reduced to

$$\frac{dN_1}{dt}_{abs} = -\frac{N_1}{g_1} \sum_{m_1,m_2} R_{m_1 m_2} = -\sigma_a \frac{I}{h\nu} N_1, \tag{2.27}$$

$$\frac{dN_2}{dt}_{em} = -\frac{N_2}{g_2}\sum_{m_1,m_2} R_{m_1m_2} = -\sigma_e \frac{I}{h\nu} N_2, \tag{2.28}$$

From Eqs. 2.27 and 2.28 we obtain a reciprocity relation between σ_a and σ_e

$$\sum_{m_1,m_2} R_{m_1m_2} = g_1\sigma_a \frac{I}{h\nu} = g_2\sigma_e \frac{I}{h\nu}, \tag{2.29}$$

$$\sigma_e = \frac{g_1}{g_2}\sigma_a \tag{2.30}$$

From experimental evidence, it turns out that the reciprocity relation given by Eq. 2.30 is not valid for Yb:fibers and many other rare-earth doped fiber amplifiers. D. E. McCumber derived a satisfactory reciprocity relation between broadband σ_e and σ_a spectra [89] which works very well for many rare-earth doped fiber amplifiers, e.g., the Yb:fiber. Here, I will follow the derivation of the McCumber relation from Ref. [14]. From McCumber theory, the transition between two energy manifold is much slower than the transition between sub-levels in each manifold. Thus, in steady state , the distribution in each manifold is assumed to be just thermal obeying the Boltzmann statistics

$$\begin{aligned} N_{m_1} &= \frac{N_1 e^{-E_{m_1}/kT}}{Z_1}, \\ N_{m_2} &= \frac{N_2 e^{-E_{m_2}/kT}}{Z_2}, \end{aligned} \tag{2.31}$$

where E_{m_1} and E_{m_2} are the energy of the sub-levels in the ground state and the excited state manifolds respectively and they are measured from the lowest sub-level in the corresponding manifold (see Fig. 2.5) and Z_1 and Z_2 are partition functions of the ground state and the excited state manifolds and they are given by

$$\begin{aligned} Z_1 &= \sum_{m_1} e^{-E_{m_1}/kT} \\ Z_2 &= \sum_{m_2} e^{-E_{m_2}/kT} \end{aligned} \tag{2.32}$$

Substituting Eqs. 2.31 in Eqs. 2.25, and 2.26, we obtain

$$\frac{dN_1}{dt}_{abs} = -\frac{N_1}{Z_1}\sum_{m_1,m_2} R^{(a)}_{m_1m_2} e^{-E_{m_1}/kT}, \tag{2.33}$$

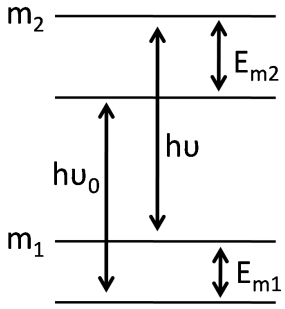

Figure 2.5: A two-level system with two sub-levels in each manifold useful for McCumber theory.

$$\frac{dN_2}{dt}_{em} = -\frac{N_2}{Z_2}\sum_{m_1,m_2} R^{(e)}_{m_2m_1} e^{-E_{m_2}/kT}, \tag{2.34}$$

Comparing Eq. 2.33 with Eq. 2.19 and Eq. 2.34 with Eq. 2.22 we obtain

$$\sigma_a(\nu) = \frac{1}{Z_1}\sum_{m_1,m_2}\frac{h\nu}{I}R^{(a)}_{m_1m_2}e^{-E_{m_1}/kT} = \frac{1}{Z_1}\sum_{m_1,m_2}\sigma^{(a)}_{m_1m_2}e^{-E_{m_1}/kT} \tag{2.35}$$

$$\sigma_e(\nu) = \frac{1}{Z_2}\sum_{m_1,m_2}\frac{h\nu}{I}R^{(e)}_{m_2m_1}e^{-E_{m_2}/kT} = \frac{1}{Z_2}\sum_{m_1,m_2}\sigma^{(e)}_{m_2m_1}e^{-E_{m_2}/kT} \tag{2.36}$$

In order to find the McCumber reciprocity relation between $\sigma_a(\nu)$ and $\sigma_e(\nu)$ from Eqs. 2.35 and 2.36, E_{m_2} is expressed in terms of E_{m_1}. Fig. 2.5 illustrates a simple case that the ground state manifold and the excited manifold have two sub-levels. From this figure, we can write

$$E_{m_2} = (h\nu - h\nu_0) + E_{m_1}, \tag{2.37}$$

where ν indicates the frequency corresponding to transition between channels m_1 and m_2, and ν_0 called the crossing frequency and is the frequency for transition between the lowest sub-levels in the two manifolds. Substituting Eq. 2.37 in Eq. 2.36, we obtain

$$\sigma_e(\nu) = \frac{e^{-(h\nu-h\nu_0)/kT}}{Z_2}\sum_{m_1,m_2}\sigma^{(e)}_{m_2m_1}e^{-E_{m_1}/kT} \tag{2.38}$$

Dividing Eq. 2.38 by Eq. 2.35 and invoking the reciprocity of absorption and emission cross sections of sub-levels, *i.e.* $\sigma^{(a)}_{m_1m_2} = \sigma^{(e)}_{m_2m_1}$, we obtain the McCumber reciprocity

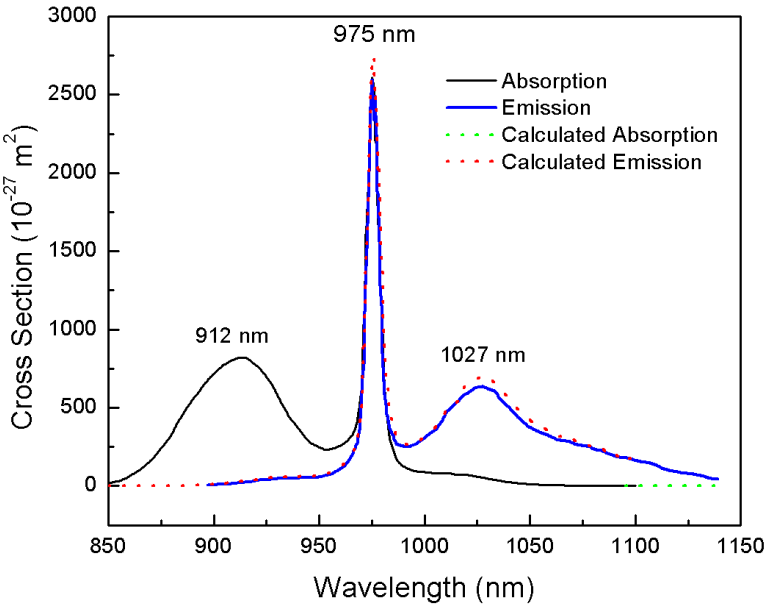

Figure 2.6: Absorption and emission cross sections of Yb^{3+} in silica fibers used in the modeling. The red dotted line shows the emission cross section calculated from the absorption cross section (black line) using Eq. 2.40. The green dotted line above 1000 nm shows the absorption cross section calculated from the emission cross section (blue line) using Eq. 2.40.(Absorption cross section (black color) and emission cross section (blue color) spectra are reproduced with permission from Ref. [13]. ©1997 IEEE.)

relation between $\sigma_e(\nu)$ and $\sigma_a(\nu)$ [14, 89, 90]

$$\sigma_e(\nu) = \frac{Z_1}{Z_2} e^{(h\nu_0 - h\nu)/kT} \sigma_a(\nu). \tag{2.39}$$

After scaling the two cross sections such that $\sigma'_e = \sigma_e/Z_1$ and $\sigma'_a = \sigma_a/Z_2$, Eq. 2.39 is reduced to

$$\sigma'_e(\lambda) = e^{(1/\lambda_0 - 1/\lambda)hc/kT} \sigma'_a(\lambda). \tag{2.40}$$

From Eq. 2.40, the following relations are valid for the crossing wavelength λ_0

$$\begin{aligned} \sigma'_e(\lambda) &< \sigma'_a(\lambda) \quad \text{for} \quad \lambda < \lambda_0 \\ \sigma'_e(\lambda) &= \sigma'_a(\lambda) \quad \text{for} \quad \lambda = \lambda_0 \\ \sigma'_e(\lambda) &> \sigma'_a(\lambda) \quad \text{for} \quad \lambda > \lambda_0 \end{aligned} \tag{2.41}$$

Fig. 2.6 shows absorption and emission cross sections of Yb:fiber used for modeling of the Yb:fibers in this thesis. The crossing wavelength $\lambda_0 = 975$ nm is the result of transition between the lowest stark sub-levels in the ground state and excited state manifolds of Yb^{3+}. From Yb^{+3} energy levels (see Fig. A.1 and Table A.1 in Appendix A.1) and using Eqs. 2.32 we obtain $Z_1 = 1.063$ and $Z_2 = 1.030$ for Yb^{3+} in the silica fiber at room temperature. With $Z_1 \cong Z_2 \cong 1$ for Yb:fiber, we will have $\sigma_e(\nu) \cong \sigma'_e(\nu)$ and $\sigma_a(\nu) \cong \sigma'_a(\nu)$ and, therefore, from Fig. 2.6 we can see that all relations given by 2.41 are valid for $\lambda_0 = 975$ nm. From Fig. 2.6, $\sigma_e(\lambda)$ (the red dotted line) has been calculated from the experimental $\sigma_a(\lambda)$ (the black line) and $\sigma_a(\lambda)$ (the green dotted line) has been calculated from the experimental $\sigma_e(\lambda)$ (the blue line) using Eq. 2.39. As can be seen, the calculated spectra reasonably agree with the experimental spectra.

In this thesis, the McCumber reciprocity relation given by Eq. 2.39 has been used to extrapolate the spectrum of the experimental effective absorption cross section (given in Ref. [13]) for $\lambda > 1100$ nm. The extrapolated absorption spectrum has been used for the modeling of amplification of these wavelengths. The extrapolation of the spectrum of the experimental effective emission cross section (given in Ref. [13]) for $\lambda < 900$ nm has been used for the calculation of effective spontaneous emission time of Yb^{+3} in the silica fiber. This will be discussed in the next section. The effective spontaneous emission time has been used in the modeling.

2.16.2 Spontaneous emission and decay time of Yb^{3+} in Yb:fiber

By assuming that there is no life time quenching effect (see Appendix A.3), the change in the population density N_{m_2} of the stark sub-level m_2 in the excited state manifold to all sub-levels in the ground state due to spontaneous emission is described by [14]

$$\frac{dN_{m_2}}{dt} = -\sum_{m_1} A_{m_2 m_1} N_{m_2}, \tag{2.42}$$

where $A_{m_2 m_1}$ is the rate of spontaneous emission for the channel $m_2 \to m_1$ and the sum goes over all stark sub-levels in the ground state manifold. By summing over m_2 of all Stark sub-levels in the excited state and using Eq. 2.31 and $N_2 = \sum_{m_2} N_{m_2}$, Eq. 2.42 becomes

$$\frac{dN_2}{dt} = -\frac{N_2}{Z_2} \sum_{m_1, m_2} A_{m_2 m_1} e^{-E_{m_2}/kT}. \tag{2.43}$$

The effective spontaneous emission rate is defined as the statistical weighted spontaneous emission rate and is given by

$$A_{21} = \frac{1}{Z_2} \sum_{m_1,m_2} A_{m_2 m_1} e^{-E_{m_2}/kT}. \tag{2.44}$$

Using Eq. 2.44, the rate equation for the spontaneous emission given by Eq. 2.43 reduces to

$$\frac{dN_2}{dt} = -A_{21} N_2. \tag{2.45}$$

Einstein applied Boltzman statistics for an ensemble of atoms which are statistically in thermodynamical equilibrium with electromagnetic waves, i.e. black body, [91]. From this, $\sigma_e(\nu)$ is given by [91]

$$\sigma_e(\nu) = \frac{\lambda^2 A_{21}}{8\pi n^2(\nu)} S(\nu), \tag{2.46}$$

where $n(\nu)$ is the index of refraction of the medium and $S(\nu)$ is the normalized lineshape of the stimulated emission. By integrating Eq. 2.46 from both sides and the fact that $\int_0^\infty S(\nu)d\nu = 1$, we obtain the Fuchtbauer-Ladenburg equation [14]

$$\frac{1}{\tau} = A_{21} = 8\pi \int_0^\infty \frac{n^2(\nu)\sigma_e(\nu)}{\lambda^2} d\nu = 8\pi c \int_0^\infty \frac{n^2(\lambda)\sigma_e(\lambda)}{\lambda^4} d\lambda. \tag{2.47}$$

The limit of the integral for ytterbium doped silica fibers, with a good approximation, lies between 850 nm and 1150 nm because $\sigma_e(\lambda)$ is very small outside this wavelength range (see Fig. 2.6). Also, the index of refraction of the silica fibers is approximately 1.45 in the 850-1150 nm wavelength range [92]. Thus, $n^2(\lambda)$ is taken out from the integral. Invoking the extrapolated $\sigma_e(\lambda)$ from Fig. 2.6 in Eq. 2.47, we obtain $\tau = 0.8$ ms for the effective spontaneous emission decay time of Yb^{3+} ions in the Yb:fiber. In this thesis, this number has been used in the modeling of the Yb:fiber laser amplifiers.

2.16.3 Population and propagation equations

In this thesis, amplification of the wavelengths between 1030 nm and 1110 nm from short laser pulses with a repetition rate of 50 MHz in the Yb:fiber have been studied. In order to find the appropriate laser equations of the amplification in the Yb:fibers, we first need to determine the number of involved energy levels. To achieve a high absorption rate of

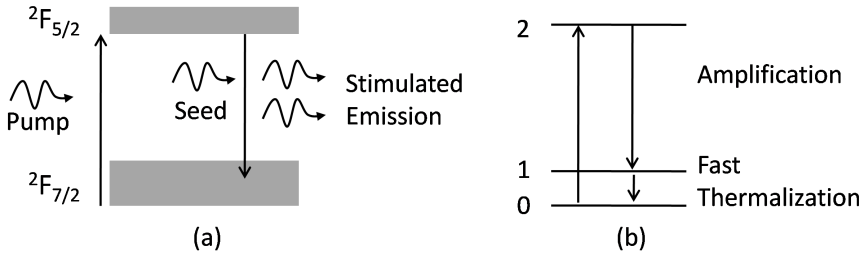

Figure 2.7: Schematic of the atomic transitions for the amplification process in the Yb:fibers.

the pump laser, the Yb:fiber is pumped at $\sim$ 975 nm because the absorption cross section peaks at this wavelength (see Fig. 2.6). Pumping at 975 nm, the amplification in above wavelength range is understood based on a quasi three-level scheme. The quasi three-level system in the Yb:fiber is simplified to a two-level system and will be explained as follows.

Firstly, as explained in Section 2.16.1 (see Appendix A.1 for more details), in the wavelengths 900-1200 nm, Yb^{+3} in the silica fiber shows two energy bands, *i.e.* the $^2F_{7/2}$ ground state manifold and the $^2F_{5/2}$ excited state manifold. Furthermore, in the Yb:fibers as explained in Appendix A.2: a) there is no excited state absorption in the 900-1200 nm and b) for a ytterbium concentration up to $\sim 8\times10^{25}$ m^{-3}, the multi-phonon non-radiative decay rate is negligible. Thus, the population and propagation equations will include only optical transitions between the sub-levels of the two energy bands.

Fig. 2.7 (a) illustrates the amplification process with the two involved energy bands and Fig. 2.7 (b) illustrates the amplification process with the three involved energy levels hidden in the two energy bands. From Fig. 2.7 (b), after absorption a photon from the pump laser at 975 nm, an electron will be excited from the energy level 0 to the energy level 2. Then, the excited electron will undergo a transition to the energy level 1 by the seed signal. As a result of that, one stimulated emission photon is added to the incident seed photon. Finally, under fast thermalization, the electron in the energy level 1 will rapidly relax to the energy level 0. Because of this fast thermalization, the population and propagation equations can be simplified to a two-level energy scheme. Nevertheless, this process is a quasi three-level scheme because in the actual three-level laser scheme the fast relaxation takes place between the level 2 and the level 1 and the amplification takes place between the level 1 and the level 0.

Secondly, the 50-MHz repetition rate of the seed laser pulses is more than four order of magnitude faster compared to the spontaneous emission rate of Yb^{+3} ions ($\sim$ 1 kHz). Therefore, the seed signal is considered as a cw input.

From above simplifications, the Yb:fiber amplifier system is modeled by using a two-level energy scheme in the cw regime. However, effective emission and absorption cross sections will be used to describe all optical transitions between all sub-levels of the two energy bands.

For the two-level laser system, the total population density N_t is given by

$$N_t = N_1 + N_2. \tag{2.48}$$

Because the total population density is constant, we have $\frac{dN_2}{dt} = -\frac{dN_1}{dt}$. Thus, from Eqs 2.19, 2.22 and 2.45, the total change in the population density N_2 of the energy level 2 is given by

$$\frac{dN_2}{dt} = -\frac{N_2}{\tau} - \frac{I}{h\nu}(\sigma_e N_2 - \sigma_a N_1), \tag{2.49}$$

where the first, second and third terms are contributions from spontaneous emission, stimulated emission and absorption respectively. For the sake of simplicity, it is assumed that the Yb:fiber is homogeneous, *i.e.*, the ytterbium concentration is constant everywhere in the fiber core as well as the fiber core radius is constant over the fiber length. In this case, the mode intensity I is the confined power in the fiber core divided by the core area A [14]. The confined power is expressed by ΓP where Γ is the mode confinement factor (see Section 2.17.1) and P is the total power of the fiber mode. Thus, Eq. 2.49 is written as [14]

$$\frac{dN_2}{dt} = -\frac{N_2}{\tau} - \frac{\lambda\Gamma P}{Ahc}(\sigma_e N_2 - \sigma_a N_1). \tag{2.50}$$

In order to obtain the actual rate equation for the population density, the two last terms in Eq. 2.50 must include all type of propagating fields in the fiber core. The first type is the field from the pump laser. The second type is the field from the seed laser. The third type is the field from amplified spontaneous emission. The mechanism of the generation of the ASE will be discussed in Section 2.16.4. By adopting the positive direction for the propagation of the seed signal in the fiber and taking into account all kinds of propagating fields in the fiber core from the pump laser, seed signal, and ASE , the rate equation for the upper state population density is given by [40, 93]

$$\begin{aligned}\frac{dN_2(z,t)}{dt} =& -\frac{N_2(z,t)}{\tau} \\ &- \frac{1}{Ahc}\sum_{i}^{\text{Pump}} \lambda_i \Gamma_p(\lambda_i)[N_2(z,t)\sigma_e(\lambda_i) - N_1(z,t)\sigma_a(\lambda_i)][uP_p^+(\lambda_i : z,t) + vP_p^-(\lambda_i : z,t)] \\ &- \frac{1}{Ahc}\sum_{j}^{\text{Seed}} \lambda_j \Gamma_s(\lambda_j)[N_2(z,t)\sigma_e(\lambda_j) - N_1(z,t)\sigma_a(\lambda_j)]P_s(\lambda_j : z,t) \\ &- \frac{1}{Ahc}\sum_{k}^{\text{ASE}} \lambda_k \Gamma_{ASE}(\lambda_k)[N_2(z,t)\sigma_e(\lambda_k) - N_1(z,t)\sigma_a(\lambda_k)][P_{ASE}^+(\lambda_k : z,t) + P_{ASE}^-(\lambda_k : z,t)],\end{aligned} \tag{2.51}$$

where i, j, and k indices go over all wavelengths in the pump laser, seed signal and ASE respectively. $P_p^+(\lambda_i : z,t)$ and $P_p^-(\lambda_i : z,t)$ are the power of the pump lasers at the wavelength λ_i, distance z, and time t for the co-pumping scheme and counter-pumping scheme respectively. For example, for the co-pumping scheme, the pump laser is injected with the seed signal from the same fiber side. We take $u = 1$ and $v = 0$ for the co-pumping scheme, $u = 0$ and $v = 1$ for the counter-pumping scheme and $u = 1$ and $v = 1$ for the two-sided pumping. The population densities $N_1(z,t)$ and $N_2(z,t)$ are dependent on z and t. $P_s(\lambda_j : z,t)$ is the power of the seed laser at the wavelength λ_j , time t and distance z. The ASE propagates in the fiber in both directions independently from the direction of propagation of the pump laser and the seed signal. Therefore, the last two terms containing the ASE power $P_{ASE}^+(\lambda_k : z,t)$ and $P_{ASE}^-(\lambda_k : z,t)$ will stay in Eq. 2.51 no matter what pumping scheme is used.

$\Gamma_p(\lambda_i)$, $\Gamma_s(\lambda_j)$, and $\Gamma_{ASE}(\lambda_k)$ are the wavelength-dependent confinement factors of the pump laser, seed signal and ASE respectively. In general, the mode confinement factor Γ is dependent on wavelength. However, the variation of Γ for the SM Yb:fibers is negligible in the 1-1.1 μm because the V number of the fiber core does not change noticeably. Thus, the Γ factors are taken out from the sum operations. For the future use in the modeling, by removing the independent variables λ, z, and t from all dependent variables as well as using N_1 from Eq. 2.48, Eq. 2.51 is written in a more compact size as

$$\frac{dN_2}{dt} = -\frac{N_2}{\tau} - \frac{\Gamma}{Ahc}\sum_{i}^{\text{Pump}} \lambda_i \left[(\sigma_e^i + \sigma_a^i)N_2 - \sigma_a^i N_t\right](uP_i^{p+} + vP_i^{p-}) \tag{2.52}$$
$$- \frac{\Gamma}{Ahc}\sum_{j}^{\text{Seed}} \lambda_j \left[(\sigma_e^j + \sigma_a^j)N_2 - \sigma_a^j N_t\right] P_j^s$$
$$- \frac{\Gamma}{Ahc}\sum_{k}^{\text{ASE}} \lambda_k \left[(\sigma_e^k + \sigma_a^k)N_2 - \sigma_a^k N_t\right](P_k^{ASE+} + P_k^{ASE-}).$$

For each propagating field in the fiber, there is a change in its power due to the interaction with Yb^{3+} ions as well as attenuation by the glass matrix. The propagation equations define the variation of power of each propagating field as a function of fiber length. First, we consider the variations of the fields of the pump laser and the seed laser. The change in the flux of one photon $\Delta\phi$ from these fields due to the stimulated emission after traveling a distance Δz in the fiber is given by

$$\Delta\phi = (N_2\Delta z)\sigma_e, \tag{2.53}$$

where $N_2\Delta z$ is the surface density of the excited ions in the fiber core and σ_e is the probability of interaction of one photon with one ion of the sort of stimulated emission. Obviously, for a beam of photons with a flux number Φ, the change of flux is given by

$$\Delta\Phi = (N_2\Delta z)\sigma_e\Phi \tag{2.54}$$

and because the power P of the propagating field is proportional to the photon flux, the change in the power ΔP due to the stimulated emission is given by [14]

$$\Delta P = (N_2\Delta z)\sigma_e(\Gamma P), \tag{2.55}$$

where Γ is the confinement factor and ΓP is the confined power in the fiber core. A similar equation for the change in the power due to the absorption by ytterbium ions can be written as [14]

$$\Delta P = -(N_1\Delta z)\sigma_a(\Gamma P), \tag{2.56}$$

where $N_1\Delta z$ is the surface density of the ions in the ground state and the negative sign is because of the reduction of power due to the absorption.

For the attenuation by the background of the fiber, the reduction of the power of each propagating field is given by

$$\Delta P = -\alpha P\Delta z, \tag{2.57}$$

where α is the wavelength-dependent attenuation factor of the silica fiber. Putting Eqs. 2.55, 2.56, and 2.57 all together and invoking Eq. 2.48, we obtain the propagation equation for the pump laser and seed signal in the plane wave approximation [40, 93]

$$\pm \frac{dP_i^{p\pm}}{dz} = \Gamma_p(\sigma_e^i + \sigma_a^i)N_2 P_i^{p\pm} - (\Gamma_p \sigma_a^i N_t + \alpha_i)P_i^{p\pm} \tag{2.58}$$

$$\frac{dP_j^s}{dz} = \Gamma_s(\sigma_e^j + \sigma_a^j)N_2 P_j^s - (\Gamma_s \sigma_a^j N_t + \alpha_j)P_j^s, \tag{2.59}$$

where, the subscripts i and j go over all wavelengths in the pump laser and seed signal respectively. The pump and seed powers as well as the upper state population density are functions of z and t. The power of the seed laser and the co-propagating and counter-propagating pump lasers are denoted by P^s, P^{p+}, and P^{p-} respectively. For the counter-propagating pump laser, a negative sign is included in the left side of Eq. 2.58 because dz is negative in this case.

2.16.4 Propagation equation of the ASE

The ASE photons in the Yb:fiber are generated primarily from zero-field spontaneous photons. These initial photons are the spontaneous emission noise in the fiber. If we divide the fiber into a number of sections, each section generates a zero field of the spontaneous emission noise independently from the other sections in the forward and backward directions. In each section, the arrived parasitic photons from the backward and forward directions are amplified by the stimulated emission process. The amplified parasitic spontaneous photons are added to the zero field parasitic spontaneous photons from the section itself. This process continues until the last section of the fiber. From this, the ASE noise becomes strong in the fiber output for highly-doped, long Yb:fibers which are pumped with powerful lasers (large number of excited Yb^{3+} ions) and seeded with low power signals because of available large gain values for the ASE.

The ASE depletes the stored energy in the Yb:fiber amplifier and therefore one needs to achieve an appropriate design to suppress it in the amplifier system. In the design, the key parameters of the Yb:fiber amplifier such as pump power, fiber length, the type of the Yb:fiber such as single clad or double clad, and seed power are investigated. This will be presented in Chapter 3. The propagation equation of the ASE in the Yb:fiber will be discussed as follows.

The first step to derive an appropriate propagation equation for the ASE power in the Yb:fiber is to find an equation for the power of the zero field spontaneous emission for each

frequency mode. Suppose that ΔV is the volume of an infinitesimal cavity in the fiber core where $\Delta V = A\Delta x$ and A is the fiber core area and Δx is an infinitesimal distance in the fiber. The total zero field ASE power for all modes in the frequency interval ν to $\nu + \Delta\nu$ in the volume ΔV is [91, 94]

$$\Delta P^0_{ASE} = [A_{21} N_2 \Delta V]\,[h\nu]\,[S(\nu)\Delta\nu]\,, \tag{2.60}$$

where $A_{21}N_2\Delta V$ is the creation rate of spontaneous photons into all frequency modes, $h\nu$ is the energy of the spontaneous photon, and $S(\nu)d\nu$ is the fraction of transitions in the frequency interval ν to $\nu + \Delta\nu$ where $S(\nu)$ is the spontaneous emission lineshape.

The total number of frequency modes in the frequency interval ν to $\nu + \Delta\nu$ and in the volume ΔV considering two polarized modes in each cavity mode is given by [91, 94]

$$m = (8\pi n^3 \nu^2)\Delta\nu / c^3 \Delta V. \tag{2.61}$$

The zero field ASE power into the frequency mode ν in the volume ΔV is obtained by dividing the total power in the frequency interval ν to $\nu + \Delta\nu$ to the total modes in this frequency interval. This is obtained by dividing Eq. 2.60 by 2.61, that is

$$\Delta P^{0,\nu}_{ASE} = \frac{A_{21} N_2 h\nu S(\nu)\Delta\nu\Delta V}{(8\pi n^3\nu^2)/c^3\Delta\nu\Delta V}. \tag{2.62}$$

Substituting $\sigma_e(\nu) = \frac{\lambda^2 A_{21}}{8\pi n^2} S(\nu)$ from Eq. 2.46 into Eq. 2.62, we obtain

$$\Delta P^{0,\nu}_{ASE} = \sigma_e(\nu) N_2 \frac{h\nu c}{n}. \tag{2.63}$$

The frequency interval $\Delta\nu$ between two longitudinal modes in the cavity with the volume ΔV and the length Δz is given by $\Delta\nu = \frac{c}{2n\Delta z}$ [91, 94]. Thus

$$\frac{1}{\Delta z} = \frac{2n}{c}\Delta\nu. \tag{2.64}$$

Multiplying both sides of Eq. 2.63 by Eq. 2.64, we obtain

$$\frac{\Delta P^{0,\nu}_{ASE}}{\Delta z} = \sigma_e(\nu) N_2 \frac{h\nu c}{n}\frac{2n}{c}\Delta\nu = \sigma_e(\nu) N_2 (2h\nu\Delta\nu), \tag{2.65}$$

or in terms of wavelength [91]

$$\frac{\Delta P^{0,\lambda}_{ASE}}{\Delta z} = \sigma_e(\lambda) N_2 \frac{2hc^2\Delta\lambda}{\lambda^3}. \tag{2.66}$$

The total change in the ASE power at each frequency mode after traveling a section of fiber with the length Δz in the fiber core is obtained by taking into account a) the contribution of the Yb:fiber amplifier gain as well as the attenuation by the silica host such as Eq. 2.58 and b) the zero field spontaneous emission of that same fiber section given by Eq. 2.66. Thus, the propagation equation of the ASE field at the wavelength λ_k is given by [40, 93]

$$\pm \frac{dP_k^{ASE\pm}}{dz} = \Gamma_{ASE}(\sigma_e^k + \sigma_a^k)N_2 P_k^{ASE\pm} - (\Gamma_{ASE}\sigma_a^k N_t + \alpha_k)P_k^{ASE\pm} + \sigma_e^k N_2 \frac{2hc^2\Delta\lambda_k}{\lambda_k^3}, \quad (2.67)$$

where, the subscript k is accounted for all wavelengths in the ASE field. The positive and negative signs in the left side of the equation above are accounted for the co-propagating and counter-propagating ASE fields respectively. Note that the ASE power $P_k^{\pm}$ and the population density of the excited state N_2 are functions of distance z and time t.

In this thesis, Eqs. 2.52, 2.58, 2.59, and 2.67 have been used for the modeling of the Yb:fiber as a fiber laser amplifier.

2.17 Single-clad and double-clad Yb:fibers

In this thesis, two types of Yb:fiber have been used: 1) a single-clad (SC) single-mode Yb:fiber as a preamplifier and 2) a double-clad (DC) single-mode polarization maintaining (PM) Yb:fiber as a main amplifier. In both fibers, only the fiber core is doped with Yb^{3+} ions.

Fig. 2.8(a) illustrates a simple schematic of the propagation of the seed signal and pump laser in a SC-YDFA. As can be seen, the seed signal counter-propagates with the

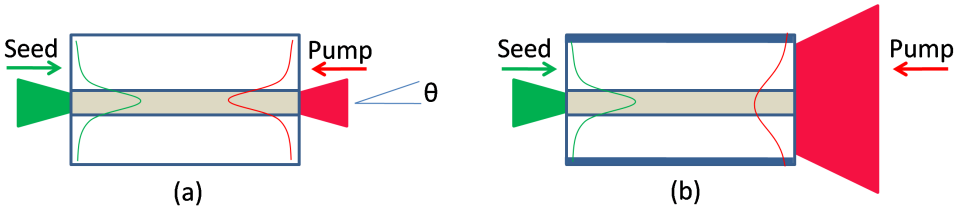

Figure 2.8: Schematic of single-clad and double-clad YDFAs. (a) Single-clad structure, (b) double-clad structure. Also it is shown, Gaussian beam profiles of the seed signal (green line) and pump laser (red line).

pump laser in the fiber core. During the propagation of the pump laser and seed signal in the fiber core, ytterbium ions become excited by absorption of the pump laser and they become de-excited by interaction with the seed signal thereby the seed signal is amplified by the stimulated emission process. The transverse mode of both seed signal and pump laser has to be a single TEM_{00} Gaussian mode in order to be launched into the SC-YDFA. The TEM_{00} mode is transformed to the LP_{01} fiber mode after confining in the SM fiber.

An optical fiber is characterized by a number called V number that is a measure for the number of guided modes supported by the fiber. The V number is found to be less than 2.405 for a SM fiber guiding only the lowest order LP_{01} fiber mode [84]. For a fiber with the fiber core radius a, the V number is related to the wavelength-dependent numerical aperture (NA) by [84]

$$V = \frac{2\pi a}{\lambda}\mathrm{NA}, \tag{2.68}$$

where λ is the wavelength of the propagating mode. The fiber NA is defined as $\sin\theta$ in Fig. 2.8 where θ is the maximum angle in air respect to the fiber axis within which the light will be guided in the fiber core by an internal reflection.

In this thesis, the fiber core diameter of the SC-YDFA is 4 μm which is surrounded by a round cladding of diameter 125 μm. From manufacturer's datasheet, the fiber NA of this fiber is 0.2 at 1060 nm which agrees with the calculated NA from Eq. 2.68 by taking the cutoff value for the V number (2.405) for guiding only the LP_{01} mode at 1060 nm. The V number value 2.405 will be used for finding the confinement factor in Section 2.17.1.

Fig. 2.8(b) illustrates a simple schematic of the propagation of the seed signal and pump laser in a DC-YDFA. From this figure, the seed signal propagates in the fiber core and the pump laser counter-propagates in the fiber inner cladding. The pumping process can be easily understood from ray tracing. That is, the pump laser travels in the inner cladding on a zig-zag path whereas it crosses the fiber core numerously. For each time the pump laser passes through the fiber core it pumps the ytterbium ions. The DC-YDFA allows us to use powerful multi-mode laser diodes to pump the DC-YDFAs. Thus, the DC-YDFA is used in the main amplifier stage. In this thesis, the fiber core diameter of the DC-YDFA is 6 μm which is surrounded by an inner cladding. The nominal NA of the fiber core of the DC-YDFA fiber is 0.15 according to the manufacturer's datasheet which agrees with the calculated NA from Eq. 2.68 by taking the cutoff value for the V number (2.405) for guiding only the LP_{01} mode at 1060 nm.

2.17.1 Confinement factor of the propagating fields in the YDFAs

It is proved that the general solutions of the wave equation for the guided modes in circular fibers are Bessel functions [84]. The Bessel functions are decaying oscillatory functions. For this reason, part of a guided mode is not confined in the fiber core but it travels in the fiber cladding and it eventually will escape from the fiber. For the fiber amplifiers is the same and only part of the power of the amplified seed signal, pump laser, and ASE is confined in the fiber core because of this partial mode confinement. To find the confined power, the confinement factor Γ is defined as the fraction of the power flowing in the fiber core. Here, I will present the approach for finding the confinement factor for the seed laser, pump laser, and ASE in the single-mode SC-YDFA and DC-YDFA used in the modeling.

After solving the wave equation in the cylindrical coordinate system, the confinement factor Γ for the fiber core is given by [84]

$$\Gamma = \frac{y^2}{V^2}[1 - \frac{J_l^2(x)}{J_{l-1}(x)J_{l+1}(x)}], \tag{2.69}$$

where J is the Bessel function of the first order, V is the V number, and x and y are defined by [84]

$$V^2 = x^2 + y^2. \tag{2.70}$$

The lowest-order confined mode in an optical fiber is LP_{01} and it is the only allowed fiber mode in a single mode fiber. To find the confinement factor for the LP_{01} mode, we substitute the y value from Eq. 2.70 and $l = 0$ in Eq. 2.69 and invoke $J_1(x) = -J_{-1}(x)$. Thus, we obtain

$$\Gamma = \frac{V^2 - x^2}{V^2}[1 + \frac{J_0^2(x)}{J_1^2(x)}]. \tag{2.71}$$

To solve Eq. 2.71 for Γ, one more equation is needed to relate the x value to the V number. This is given by the mode condition [84]

$$x\frac{J_{l+1}(x)}{J_l(x)} = y\frac{K_{l+1}(y)}{K_l(y)}, \tag{2.72}$$

where K is the Bessel function of the second order. By substituting the y value from Eq. 2.70 and $l = 0$ in Eq. 2.72 we obtain

$$x\frac{J_1(x)}{J_0(x)} = \sqrt{V^2 - x^2}\frac{K_1(\sqrt{V^2 - x^2})}{K_0(\sqrt{V^2 - x^2})}. \tag{2.73}$$

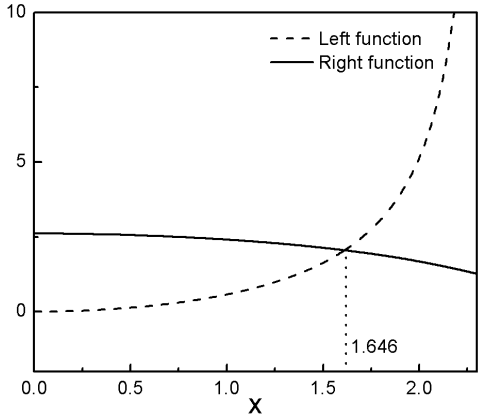

Figure 2.9: Graphical method to determine x value of the LP_{01} mode for $V = 2.405$.

Table 2.1: Fiber parameters of the SC-YDFA and DC-YDFA used in the modeling.

Type	Core Diameter (μm)	Core NA	Cladding Diameter (μm)	Cladding NA	Cladding Geometry	N_t (m^{-3})	Γ_s, Γ_{ASE}	Γ_p
SC-YDFA	4	0.2	125	–	Round	8×10^{25}	0.83	0.83
DC-YDFA	6	0.14	125	0.46	Round	8×10^{25}	0.83	2.304×10^{-3}

The x value for a specified V number is determined by solving Eq. 2.73 numerically. The V number is 2.405 for the SM YDFAs used in this thesis (see section 2.17). Fig. 2.9 shows the plot of the left hand side and right hand side of Eq. 2.73 using Mathematica program. From this figure, we find x=1.646 where the two curves intersect. Substituting this x value in Eq. 2.71, we obtain $\Gamma = 0.83$.

In this thesis, the 0.83 value has been used in the modeling for the confinement factor of the pump laser, seed laser, and ASE in the single mode SC-YDFA as well as the seed laser and ASE in the single mode DC-YDFA.

For the DC-YDFA, the confinement factor of the pump laser to the fiber core can be easily determined by the ratio of the areas of the fiber core and the fiber cladding. For the DC-YDFA with the core diameter 6 μm and the inner cladding diameter 125 μm, the confinement factor is found to be 2.304×10^{-3}. In this thesis, this value has been used in the modeling of the single mode DC-YDFA. Table 2.1 summarizes all the key fiber parameters discussed in Sections 2.17 to 2.17.1.

2.17.2 Concentration of ytterbium in the YDFAs

In both SC and DC Yb:fibers used in this thesis, the fiber core is highly doped with Yb^{3+}. Because the data sheets give us pump absorption rates rather than Yb^{3+} concentration we use Beer-Lambert law to determine concentration

$$P(z) = P_0 e^{-\alpha z}, \tag{2.74}$$

where Pz and P_0 are the power of the transmitted and the incident light, respectively, α is the absorption coefficient per unit length and z is the propagation distance. The absorption coefficient L defined in terms of (dB/m) is given by

$$L(\text{dB/m}) = \frac{10}{z} log_{10}(\frac{P(z)}{P_0}) \tag{2.75}$$

From Eqs. 2.74 and 2.75, we obtain

$$L(\text{dB/m}) = 4.343\,\alpha\,(1/\text{m}). \tag{2.76}$$

For a low-power signal which is propagating in a medium with two energy levels, the is absorption rate is much higher than the stimulated emission, so we can write

$$\alpha = \sigma_a N_t, \tag{2.77}$$

where N_t is accounted for the concentration of Yb^{3+}. From Eqs. 2.76 and 2.77 we obtain

$$N_t = \frac{L(\text{dB/m})}{4.343\,\sigma_a} \tag{2.78}$$

According to the manufacturer's datasheet, the average absorption coefficient of the fiber core of the two types of Yb:fiber is $L = 280$ dB/m at 920 nm. In addition, from Fig. 2.6 we find $\sigma_a = 7.73 \times 10^{-25}$ m^{-3} at 920 nm. Substituting L and σ_a in Eq. 2.78, we obtain $N_t \cong 8 \times 10^{25}$ m^{-3} for the concentration of Yb^{3+}.

This value has been used in the modeling of the SC and DC Yb:fibers used. In the modeling, it is also assumed that the Yb^{3+} concentration in the fiber core is uniform both radially and along the fiber core.

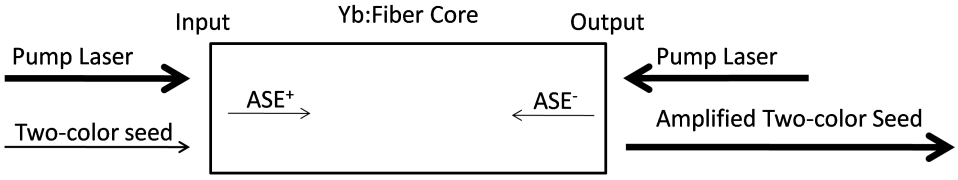

Figure 2.10: The fiber core of the Yb:fiber and the propagating fields of the pump laser, seed signal, and ASE.

2.18 Modeling of the two-color ultrafast YDFA system

In this thesis, for modeling the two-color ultrafast YDFA system, Eqs. 2.52, 2.58, 2.59, and 2.67 have been solved numerically. These equations have also been used for modeling a dual-wavelength, ultrafast double-clad YDFA system [40], heat dissipation in high power Yb:fiber amplifiers [33, 34], and Yb:fiber lasers [95].

These equations are coupled in a way that there are many coupled electronic oscillators (Yb^{+3} ions) along the Yb:fiber core. Each oscillator with its own natural frequency has a chance to be excited with a wide range of frequencies with different amplitudes from the two-color seed signal, ASE and pump lasers. Therefore, these equations need to be solved for all fields in each segment of the fiber core simultaneously. In modeling, we are seeking a set of numerical solutions to these equations in the steady state. In the steady state, the upper state population density and the power of each propagating field do not change with time in each segment of the Yb:fiber core. In programing, this means that an adequate number of iterations should be performed between the propagation equations and the population equations in each segment of the fiber until the numerical solutions to the equations are stabilized with a well defined accuracy.

Fig. 2.10 shows the fiber core of the Yb:fiber and the propagating fields. The Yb:fiber can be of the sort of single clad (SC) or double clad (DC). In this figure, as a general case, the Yb:fiber is pumped from both ends. In the pumping process, the pump lasers deliver energy to ytterbium ions. A fraction of the pump power may exit from the opposite side. This depends on the fiber length, pump power, dopant density, and fiber type (SC or DC).

From this figure, a two-color seed signal propagates from the input side toward the output side. A fraction of the absorbed pump power is transfered to the propagating seed signal. The seed signal achieves more gain as it travels further in the Yb:fiber core if it sees a positive gain. Unfortunately, some of the pump power is wasted with the generation of

the ASE in both forward and backward directions. The ASE is initiated from a zero-field parasitic spontaneous emission photons from the beginning of the Yb:fiber and is amplified as it travels further in the pumped fiber core (see section 2.16.4). The forward-traveling ASE^{+} and the backward traveling ASE^{-} are generated in both one-sided and two-sided pumping schemes. The problem is that the ASE competes with the seed signal. This is because of gain competition in Yb:fibers due to the homogeneously broadened gain profile of the Yb:fiber [9]. The outcome of this competition depends on a number of factors such as fiber length, wavelengths of the two-colors seed signal, and input power of the two-color seed signal. One of the major goals in the modeling has been to find the optimum condition of the two-color YDFA system with a reduced ASE power.

Fig. 2.11 shows the Yb:fiber divided into n segments of equal length δz used in the modeling. The population density and the power of each field are functions of distance and time. In order to find all of these time-distance-dependent functions in the fiber core, we let the fields propagate from the fiber ends. To achieve the steady state in all segments, one may find the steady state in each segment before letting the fields enter into the

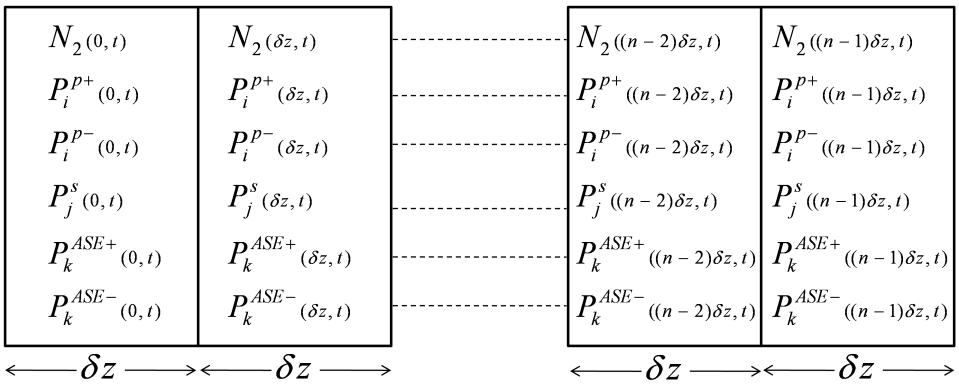

Figure 2.11: The Yb:fiber divided into equidistant segments used in the modeling.

next segment. The major problem with this method is the large number of mathematical operations for long fibers. In a more time-effective method that will be called *stable output power* (SOP), we let the fields propagate to the fiber end. The output from each segment of the fiber is an input to the next segment of the Yb:fiber core. Then, the power of each propagating field and the upper state population density are found in each segment of the Yb:fiber core. The iteration between the propagation and population equations are performed until the state of SOP is achieved in the last segment of the Yb:fiber core with a meaningful stability. For example for a 10 mW output power, 0.05 % stability is equivalent to 5 μW which is a reasonable approximation in order to compare the modeling results with

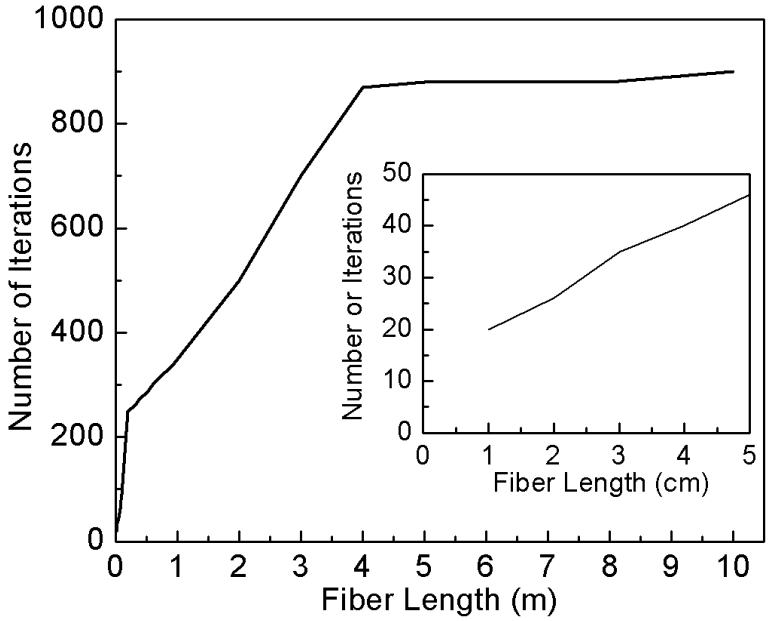

Figure 2.12: Variation of the number of iterations as a function of Yb:fiber length to achieve 0.05 % stability in the output power. Note, the unit for the fiber length in the main frame is meter and in the inset graph is centimeter.

measurements using standard laser power meters. Upon achieving the specified stability, calculations are terminated. In this thesis, I have devised and used this method.

To demonstrate the usefulness of the SOP method, Fig. 2.12 shows the simulation result to the number of iterations as a function of fiber length after the amplified output power has been stabilized by 0.05 %. In the simulation, the fiber has been a SC Yb:fiber pumped from both ends with 45 mW at 975 nm and seeded with a 4-mW two-color spectrum centered at 1035 nm and 1105 nm. The fiber has been divided into 1-mm-long segments and the output power is calculated after each 2 μs time increment. As can be seen, the number of iterations grows up with the fiber length and more importantly it does not change very much above 4 m. The flat area confirms that the SOP is a time efficient method for modeling the long Yb:fibers. The inset graph is a close-up graph for the fiber lengths up to 5 cm. From this graph, the number of iterations for a 1-cm-long Yb:fiber is 20. That means, it would be needed, more or less, 20,000 iterations between the propagation and population equations for a 10-m-long fiber if in the programming the steady state was calculated from segment to segment at each 1-cm length increment. However, from the SOP method shown in the main frame of Fig. 2.12, the number of iterations for a 10-cm-long fiber is only 900.

2.18.1 The systematic approach in the programming

In this thesis, the Yb:fiber core is divided into 1-mm-long equidistant segments [40] to obtain the output at each 1-cm length increment. From Fig. 2.11, it becomes obvious that in the segmented fiber, the local upper state population density and the local field powers can be grouped into appropriate matrix forms. This has facilitated the programming.

For the n-segment Yb:fiber, the upper state population density is expressed in terms of an n-element array $\mathcal{N}(z,t)$ such as

$$\mathcal{N}(z,t) = [N(0,t), N(\delta z,t), \cdots, N((n-2)\delta z,t), N((n-1)\delta z,t)]\,. \tag{2.79}$$

The power spectra of the pump laser, seed signal, and ASE are divided into i, j, and k channels respectively whereas to each channel is assigned a wavelength. Accordingly, we will write the n-element-array forward-traveling pump power $\mathcal{P}_i^{p+}(z,t)$ at wavelength λ_i

$$\mathcal{P}_i^{p+}(z,t) = \left[P_i^{p+}(0,t), P_i^{p+}(\delta z,t), \cdots, P_i^{p+}((n-2)\delta z,t), P_i^{p+}((n-1)\delta z,t)\right], \tag{2.80}$$

the n-element-array backward-traveling pump power $\mathcal{P}_i^{p-}(z,t)$ at wavelength λ_i

$$\mathcal{P}_i^{p-}(z,t) = \left[P_i^{p-}(0,t), P_i^{p-}(\delta z,t), \cdots, P_i^{p-}((n-2)\delta z,t), P_i^{p-}((n-1)\delta z,t)\right], \tag{2.81}$$

the n-element-array seed power $\mathcal{P}_j^{s}(z,t)$ at wavelength λ_j

$$\mathcal{P}_j^{s}(z,t) = \left[P_j^{s}(0,t), P_j^{s}(\delta z,t), \cdots, P_j^{s}((n-2)\delta z,t), P_j^{s}((n-1)\delta z,t)\right], \tag{2.82}$$

the n-element-array forward-traveling ASE power $\mathcal{P}_k^{ASE+}(z,t)$ at wavelength λ_k

$$\mathcal{P}_k^{ASE+}(z,t) = \left[P_k^{ASE+}(0,t), P_k^{ASE+}(\delta z,t), \cdots, P_k^{ASE+}((n-2)\delta z,t), P_k^{ASE+}((n-1)\delta z,t)\right], \tag{2.83}$$

and the n-element-array backward-traveling ASE power $\mathcal{P}_k^{ASE-}(z,t)$ at wavelength λ_k

$$\mathcal{P}_k^{ASE-}(z,t) = \left[P_k^{ASE-}(0,t), P_k^{ASE-}(\delta z,t), \cdots, P_k^{ASE-}((n-2)\delta z,t), P_k^{ASE-}((n-1)\delta z,t)\right]. \tag{2.84}$$

By defining five wavelength-dependent variables, the matrix forms of the population Eq. 2.52 and the propagation Eqs. 2.58, 2.59, and 2.67 can be written in a more compact size. For the population equation, the two variables ζ and η are given by

$$\zeta = -\frac{\lambda\Gamma}{Ahc}(\sigma_e + \sigma_a), \tag{2.85}$$

$$\eta = \frac{\lambda\Gamma}{Ahc}\sigma_a, \tag{2.86}$$

and for the propagation equations, the three variables κ, μ, and ξ are given by

$$\kappa = \Gamma(\sigma_e + \sigma_a), \tag{2.87}$$

$$\mu = -(\Gamma\sigma_a + \alpha/N_t), \tag{2.88}$$

$$\xi = \sigma_e \frac{2hc^2\Delta\lambda}{\lambda^3}, \tag{2.89}$$

where ξ is used only in the ASE propagation equation. Substituting ζ and η from Eqs. 2.85 and 2.86 into Eq. 2.52 , we obtain

$$\begin{aligned}\frac{dN_2}{dt} = -\frac{N_2}{\tau} &+ \left[\sum_i^{\text{Pump}} (\zeta_i^p N_2 + \eta_i^p N_t)(uP_i^{p+} + vP_i^{p-})\right] \\ &+ \left[\sum_j^{\text{Seed}} (\zeta_j^s N_2 + \eta_j^s N_t) P_j^s\right] \\ &+ \left[\sum_k^{\text{ASE}} (\zeta_k^{ASE} N_2 + \eta_k^{ASE} N_t)(P_k^{ASE+} + P_k^{ASE-})\right],\end{aligned} \tag{2.90}$$

and by substituting κ, μ, and ξ into Eqs. 2.58, 2.59, and 2.67, we obtain

$$\pm\frac{dP_i^{p\pm}}{dz} = (\kappa_i^p N_2 + \mu_i^p N_t)P_i^{p\pm}, \tag{2.91}$$

$$\frac{dP_j^s}{dz} = (\kappa_j^s N_2 + \mu_j^s N_t)P_j^s, \tag{2.92}$$

$$\pm \frac{dP_k^{ASE\pm}}{dz} = (\kappa_k^{ASE} N_2 + \mu_k^{ASE} N_t) P_k^{ASE\pm} + \xi_k N_2. \tag{2.93}$$

Eqs. 2.90 to 2.93 constitute a system of coupled differential equations. In this thesis, the finite-difference method up to the first order Taylor's expansion is used to solve each differential equation. For example, for a differential equation given by

$$\frac{dP}{dz} = f(z, P, N), \tag{2.94}$$

where both P and N are functions of z, the value of P at the point z_{n+1} is approximated by

$$P_{n+1} = P_n + f(z_n, P_n, N_n)\,\Delta z, \tag{2.95}$$

where $\Delta z = z_{n+1} - z_n$.

Applying Eq. 2.95 to the differential equation 2.91, we obtain a system of coupled nonlinear equations for the forward-propagating pump laser at the pump wavelength λ_i

$$\begin{cases} P_i^{p+}(\delta z, t) = P_i^{p+}(0,t) + \delta z(\kappa_i^p N_2(0,t) + \mu_i^p N_t) P_i^{p+}(0,t) \\ P_i^{p+}(2\delta z, t) = P_i^{p+}(\delta z, t) + \delta z(\kappa_i^p N_2(\delta z, t) + \mu_i^p N_t) P_i^{p+}(\delta z, t) \\ \cdots \\ \cdots \\ \cdots \\ P_i^{p+}((n-1)\delta z, t) = P_i^{p+}((n-2)\delta z, t) + \delta z(\kappa_i^p N_2((n-2)\delta z, t) + \mu_i^p N_t) P_i^{p+}((n-2)\delta z, t) \\ P_{i,\text{out}}^{p+}(L^+, t) = P_i^{p+}((n-1)\delta z, t) + \delta z(\kappa_i^p N_2((n-1)\delta z, t) + \mu_i^p N_t) P_i^{p+}((n-1)\delta z, t). \end{cases} \tag{2.96}$$

Note that, $P_i^{p+}(0,t)$ is the forward input pump power. This system of equations is solved from top to bottom in a manner that the input power to each equation is the output power from the previous equation. For the first equation, the input power is the amount of pump power injected into the Yb:fiber core at the wavelength λ_i. The upper state population density at each segment of the fiber is different from each other and it is derived from the population equation. However, it is zero at all segments of the fiber in the beginning of running the iteration between the propagation and population equations. The solution $P_{i,\text{out}}^{p+}(L^+, t)$ to the last equation is the output power from the fiber. In the programming, the number of system of equations given by Eq. 2.95 is equal to the number of assigned pump wavelengths. After solving for m number of pump wavelengths,

a pump-power matrix for the forward-propagating pump laser is obtained

$$\begin{bmatrix} P_1^{p+}(0,t) & P_1^{p+}(\delta z,t) & \cdots & P_1^{p+}((n-1)\delta z,t) & P_{1,\text{out}}^{p+}(L^+,t) \\ P_2^{p+}(0,t) & P_2^{p+}(\delta z,t) & \cdots & P_2^{p+}((n-1)\delta z,t) & P_{2,\text{out}}^{p+}(L^+,t) \\ & & \cdots & & \\ & & \cdots & & \\ P_m^{p+}(0,t) & P_m^{p+}(\delta z,t) & \cdots & P_m^{p+}((n-1)\delta z,t) & P_{m,\text{out}}^{p+}(L^+,t) \end{bmatrix}. \tag{2.97}$$

For the backward-propagating pump laser, the system of coupled nonlinear equations starts from the last segment of the fiber. For this, the transpose array of the population density array $\mathcal{N}(z,t)$ is derived such that

$$\mathcal{N}^T(z,t) = [N((n-1)\delta z,t), N((n-2)\delta z,t), \cdots, N(\delta z,t), N(0,t)]\,. \tag{2.98}$$

The $\mathcal{N}^T(z,t)$ array is fed into the propagation equation for the backward-propagating pump laser. Applying Eq. 2.95 to the differential equation 2.91, the system of coupled nonlinear equations for the backward-propagating pump laser at the pump wavelength λ_i is given by

$$\begin{cases} P_i^{p-}((n-2)\delta z,t) = P_i^{p-}((n-1)\delta z,t) + \delta z(\kappa_i^p N_2((n-1)\delta z,t) + \mu_i^p N_t)P_i^{p-}((n-1)\delta z,t) \\ P_i^{p-}((n-3)\delta z,t) = P_i^{p-}((n-2)\delta z,t) + \delta z(\kappa_i^p N_2((n-2)\delta z,t) + \mu_i^p N_t)P_i^{p-}((n-2)\delta z,t) \\ \qquad\qquad \cdots \\ \qquad\qquad \cdots \\ P_i^{p-}(0,t) = P_i^{p-}(\delta z,t) + \delta z(\kappa_i^p N_2(\delta z,t) + \mu_i^p N_t)P_i^{p-}(\delta z,t) \\ P_{i,\text{out}}^{p-}(L^-,t) = P_i^{p-}(0,t) + \delta z(\kappa_i^p N_2(0,t) + \mu_i^p N_t)P_i^{p-}(0,t), \end{cases}, \tag{2.99}$$

where $P_i^{p-}((n-1)\delta z,t)$ is the backward input pump power and $P_{i,\text{out}}^{p-}(L^-,t)$ is the output power from the seed side. Accordingly, the pump-power matrix for the backward-propagating pump laser of an m-wavelength channel pump laser is given by

$$\begin{bmatrix} P_1^{p-}(0,t) & P_1^{p-}(\delta z,t) & \cdots & P_1^{p-}((n-1)\delta z,t) & P_{1,\text{out}}^{p-}(L^-,t) \\ P_2^{p-}(0,t) & P_2^{p-}(\delta z,t) & \cdots & P_2^{p-}((n-1)\delta z,t) & P_{2,\text{out}}^{p-}(L^-,t) \\ & & \cdots & & \\ & & \cdots & & \\ P_m^{p-}(0,t) & P_m^{p-}(\delta z,t) & \cdots & P_m^{p-}((n-1)\delta z,t) & P_{m,\text{out}}^{p-}(L^-,t) \end{bmatrix}. \tag{2.100}$$

Similarly, a system of coupled nonlinear equations for the two-color seed at the seed

wavelength λ_j is given by

$$\begin{cases} P_j^s(\delta z,t) = P_j^s(0,t) + \delta z(\kappa_j^s N_2(0,t) + \mu_j^s N_t) P_i^s(0,t) \\ P_j^s(2\delta z,t) = P_j^s(\delta z,t) + \delta z(\kappa_j^s N_2(\delta z,t) + \mu_j^s N_t) P_j^s(\delta z,t) \\ \cdots \\ \cdots \\ P_j^s((n-1)\delta z,t) = P_j^s((n-2)\delta z,t) + \delta z(\kappa_j^s N_2((n-2)\delta z,t) + \mu_j^s N_t) P_j^s((n-2)\delta z,t) \\ P_{j,\text{out}}^s(L^+,t) = P_j^s((n-1)\delta z,t) + \delta z(\kappa_j^s N_2((n-1)\delta z,t) + \mu_j^s N_t) P_j^s((n-1)\delta z,t), \end{cases} \tag{2.101}$$

and the seed-power matrix consisting of n wavelengths is given by

$$\begin{bmatrix} P_1^s(0,t) & P_1^s(\delta z,t) & \cdots & P_1^s((n-1)\delta z,t) & P_{1,\text{out}}^s(L^+,t) \\ P_2^s(0,t) & P_2^s(\delta z,t) & \cdots & P_2^s((n-1)\delta z,t) & P_{2,\text{out}}^s(L^+,t) \\ & & \cdots & & \\ & & \cdots & & \\ P_n^s(0,t) & P_n^s(\delta z,t) & \cdots & P_n^s((n-1)\delta z,t) & P_{n,\text{out}}^s(L^+,t) \end{bmatrix}. \tag{2.102}$$

The system of coupled nonlinear equations for the propagation of the ASE is obtained by adding the zero-field ASE term ξN_2 in the propagation equations given previously. For the forward-propagating ASE field, the system of coupled propagation equations at the ASE wavelength λ_k is given by

$$\begin{cases} P_k^{ASE+}(\delta z,t) = P_k^{ASE+}(0,t) + \delta z[(\kappa_k^{ASE} N_2(0,t) + \mu_k^{ASE} N_t) P_k^{ASE+}(0,t) + \xi_k N_2(0,t)] \\ P_k^{ASE+}(2\delta z,t) = P_k^{ASE+}(\delta z,t) + \delta z[(\kappa_k^{ASE} N_2(\delta z,t) + \mu_k^{ASE} N_t) P_k^{ASE+}(\delta z,t) + \xi_k N_2(\delta z,t)] \\ \cdots \\ \cdots \\ \cdots \\ P_k^{ASE+}((n-1)\delta z,t) = P_k^{ASE+}((n-2)\delta z,t) + \delta z[(\kappa_k^{ASE} N_2((n-2)\delta z,t) + \mu_k^{ASE} N_t) \\ \times P_k^{ASE+}((n-2)\delta z,t) + \xi_k N_2((n-2)\delta z,t)] \\ P_{k,\text{out}}^{ASE+}(L^+,t) = P_k^{ASE+}((n-1)\delta z,t) + \delta z[(\kappa_k^{ASE} N_2((n-1)\delta z,t) + \mu_k^{ASE} N_t) \\ \times P_k^{ASE+}((n-1)\delta z,t) + \xi_k N_2((n-1)\delta z,t)]. \end{cases} \tag{2.103}$$

From these equations, in the first run of the iteration, the ASE power at all wavelengths and in all segments of the Yb:fiber is zero because $N_2(z,0)$ is zero at time zero in all

segments of the fiber. However, in the second run where N_2 is not zero, the ASE starts building up from the zero-field ASE term in the first equation of 2.103. The ASE-power matrix for the forward-traveling ASE field consisting of l wavelengths is given by

$$\begin{bmatrix} P_1^{ASE+}(0,t) & P_1^{ASE+}(\delta z,t) & \cdots & P_1^{ASE+}((n-1)\delta z,t) & P_{1,\text{out}}^{ASE+}(L^+,t) \\ P_2^{ASE+}(0,t) & P_2^{ASE+}(\delta z,t) & \cdots & P_2^{ASE+}((n-1)\delta z,t) & P_{2,\text{out}}^{ASE+}(L^+,t) \\ & & \cdots & & \\ & & \cdots & & \\ P_l^{ASE+}(0,t) & P_l^{ASE+}(\delta z,t) & \cdots & P_l^{ASE+}((n-1)\delta z,t) & P_{l,\text{out}}^{ASE+}(L^+,t) \end{bmatrix}. \tag{2.104}$$

For the backward-propagating ASE field, the transpose array $\mathcal{N}^T(z,t)$ is fed into the propagation equation 2.93, thereby, the system of coupled propagation equations at the ASE wavelength λ_k is given by

$$\begin{cases} P_k^{ASE-}((n-2)\delta z,t) = P_k^{ASE-}((n-1)\delta z,t) + \delta z(\kappa_k^{ASE}N_2((n-1)\delta z,t) + \mu_k^{ASE}N_t) \\ \qquad \times P_k^{ASE+}((n-1)\delta z,t) + \xi_k N_2((n-1)\delta z,t) \\ P_k^{ASE-}((n-3)\delta z,t) = P_k^{ASE-}((n-2)\delta z,t) + \delta z(\kappa_k^{ASE}N_2((n-2)\delta z,t) + \mu_k^{ASE}N_t) \\ \qquad \times P_k^{ASE+}((n-2)\delta z,t) + \xi_k N_2((n-2)\delta z,t) \\ \cdots \\ \cdots \\ \cdots \\ P_k^{ASE-}(0,t) = P_k^{ASE-}(\delta z,t) + \delta z(\kappa_k^{ASE}N_2(\delta z,t) + \mu_k^{ASE}N_t)P_k^{ASE-}(\delta z,t) + \xi_k N_2(\delta z,t) \\ P_{k,out}^{ASE-}(L^-,t) = P_k^{ASE-}(0,t) + \delta z(\kappa_k^{ASE}N_2(0,t) + \mu_k^{ASE}N_t)P_k^{ASE-}(0,t) + \xi_k N_2((0,t) \end{cases} \tag{2.105}$$

The ASE power matrix for the backward-propagating ASE field consisting of l wavelengths is given by

$$\begin{bmatrix} P_1^{ASE-}(0,t) & P_1^{ASE-}(\delta z,t) & \cdots & P_1^{ASE-}((n-1)\delta z,t) & P_{1,\text{out}}^{ASE-}(L^-,t) \\ P_2^{ASE-}(0,t) & P_2^{ASE-}(\delta z,t) & \cdots & P_2^{ASE-}((n-1)\delta z,t) & P_{2,\text{out}}^{ASE-}(L^-,t) \\ & & \cdots & & \\ & & \cdots & & \\ P_l^{ASE-}(0,t) & P_l^{ASE-}(\delta z,t) & \cdots & P_l^{ASE-}((n-1)\delta z,t) & P_{l,\text{out}}^{ASE-}(L^-,t) \end{bmatrix}. \tag{2.106}$$

After finding the distribution of power of each propagating field in the Yb:fiber core, the population equation given by Eq. 2.90 is solved by the use of power matrices given by Eqs. 2.97, 2.100, 2.102, 2.104, and 2.106. For this, the population equation is written for each segment of the fiber by invoking the corresponding column of the power matrices and the corresponding element of the population array 2.79. Using the finite-difference method given by Eq. 2.95, the population equation in the matrix form is given by

$$\begin{pmatrix} N_2(0,(t+\delta t)) \\ N_2(\delta z,(t+\delta t)) \\ \cdot \\ N_2((n-2)\delta z,(t+\delta t)) \\ N_2((n-1)\delta z,(t+\delta t)) \end{pmatrix} = \begin{pmatrix} N_2(0,t) \\ N_2(\delta z,t) \\ \cdot \\ N_2((n-2)\delta z,t) \\ N_2((n-1)\delta z,t) \end{pmatrix} - \frac{\delta t}{\tau} \begin{pmatrix} N_2(0,t) \\ N_2(\delta z,t) \\ \cdot \\ N_2((n-2)\delta z,t) \\ N_2((n-1)\delta z,t) \end{pmatrix} \tag{2.107}$$

$$+\delta t \begin{pmatrix} \sum_i^{\text{Pump}}(\zeta_i^p N_2(0,t)+\eta_i^p N_t)(uP_i^{p+}(0,t)+vP_i^{p-}(0,t)) \\ \sum_i^{\text{Pump}}(\zeta_i^p N_2(\delta z,t)+\eta_i^p N_t)(uP_i^{p+}(\delta z,t)+vP_i^{p-}(\delta z,t)) \\ \cdot \\ \sum_i^{\text{Pump}}(\zeta_i^p N_2((n-2)\delta z,t)+\eta_i^p N_t)(uP_i^{p+}((n-2)\delta z,t)+vP_i^{p-}((n-2)\delta z,t)) \\ \sum_i^{\text{Pump}}(\zeta_i^p N_2((n-1)\delta z,t)+\eta_i^p N_t)(uP_i^{p+}((n-1)\delta z,t)+vP_i^{p-}((n-1)\delta z,t)) \end{pmatrix}$$

$$+\delta t \begin{pmatrix} \sum_i^{\text{Seed}}(\zeta_i^s N_2(0,t)+\eta_i^s N_t)P_i^s(0,t) \\ \sum_i^{\text{Seed}}(\zeta_i^s N_2(\delta z,t)+\eta_i^s N_t)P_i^s(\delta z,t) \\ \cdot \\ \sum_i^{\text{Seed}}(\zeta_i^s N_2((n-2)\delta z,t)+\eta_i^s N_t)P_i^s((n-2)\delta z,t) \\ \sum_i^{\text{Seed}}(\zeta_i^s N_2((n-1)\delta z,t)+\eta_i^s N_t)P_i^s((n-1)\delta z,t) \end{pmatrix}$$

$$+\delta t \begin{pmatrix} \sum_i^{\text{ASE}} (\zeta_i^{ASE} N_2(0,t) + \eta_i^{ASE} N_t)(P_i^{ASE+}(0,t) + P_i^{ASE-}(0,t)) \\ \sum_i^{\text{ASE}} (\zeta_i^{ASE} N_2(\delta z,t) + \eta_i^{ASE} N_t)(P_i^{ASE+}(\delta z,t) + P_i^{ASE-}(\delta z,t)) \\ \cdot \\ \sum_i^{\text{ASE}} (\zeta_i^{ASE} N_2((n-2)\delta z,t) + \eta_i^{ASE} N_t)(P_i^{ASE+}((n-2)\delta z,t) + P_i^{ASE-}((n-2)\delta z,t)) \\ \sum_i^{\text{ASE}} (\zeta_i^{ASE} N_2((n-1)\delta z,t) + \eta_i^{ASE} N_t)(P_i^{ASE+}((n-1)\delta z,t) + P_i^{ASE-}((n-1)\delta z,t)) \end{pmatrix}$$

The population array obtained from the left side of the matrix equation 2.107 is updated in the program using the power matrices of the propagating fields in the fiber core and taking $\delta t = 2$ μs and $\tau = 0.8$ ms. The new population array is substituted in Eqs. 2.96, 2.99, 2.101, 2.103, and 2.105 to obtain new power matrices of the propagating fields in the Yb:fiber core. This routine continues until the SOP condition is satisfied. From the simulation results, a reasonably SOP has been achieved when the variation of the output power is less than 0.05%.

2.19 The LabVIEW program

In this thesis, I have created a LabVIEW program to simulate the amplification of high-repetition-rate two-color laser pulses in the YDFA based on the modeled equations presented in section 2.18.1. LabVIEW is more importantly popular for its versatile data acquisition tools to communicate with a wide collection of digital equipment for monitoring, signal processing, as well as controlling purposes. In this thesis, however, other potential benefits of LabVIEW such as graphical programming and visualization have been found very useful. Therefore, the main effort has been concentrated on the mathematical model and algorithm.

Fig. 2.13 shows the flowchart of the LabVIEW program. In the '*Modeling Mode*' block, one of the two operating modes can be selected: 1) fiber length variation and 2) pump power variation. In the fiber length variation mode, the power spectra of the propagating fields are calculated as a function of fiber length while the input pump powers are constant. In the pump power variation mode, the power spectra are calculated as a function of pump power while the fiber length is constant.

The next block in the flow chart is the '*Two-color Seed, Pump Laser, ASE*' block. Although pump, seed and ASE fields have continuous spectrum, in order to solve the rate equations numerically each field is divided into channels with a corresponding wavelength. For this, the input power spectra are created as two-dimensional (2D) arrays consisting

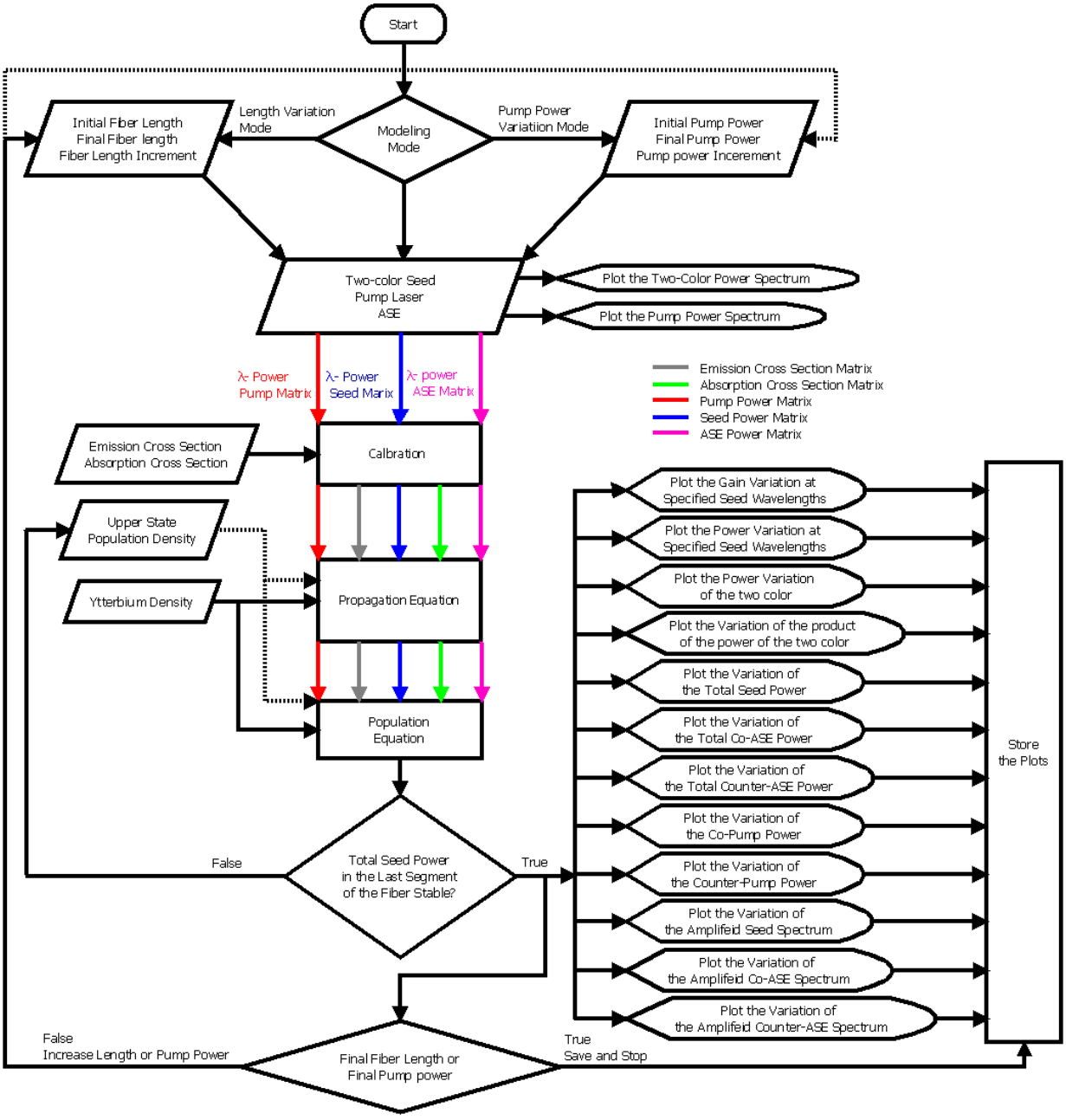

Figure 2.13: The flowchart of the computer program for the Yb:fiber simulation.

of wavelengths in the first column and the attributed powers in the second column. The input 2D arrays are prepared in the *.txt file format and are called into the program. Ideally, the input power spectrum of the two-color seed and the pump lasers are prepared from measured power spectra, otherwise, the 2D arrays are built from arbitrary powers at specified wavelengths. The input two-color seed and pump power spectra are plotted once the programs gets started.

The input power spectrum of the ASE is generated by a subroutine in the program after taking input values from user. For this, the input power spectrum of the ASE is constructed by the minimum ASE wavelength, the maximum ASE wavelength and the bandwidth of the channels. In total, there are five 2D-array power spectra of the sort $P_{\lambda}^{p+}(0,0)$, $P_{\lambda}^{p-}(L,0)$, $P_{\lambda}^{s}(0,0)$, $P_{\lambda}^{ASE+}(0,0)$, $P_{\lambda}^{ASE-}(L,0)$ where in the parentheses, the first number is the distance z and the second number is the time t. In the flowchart, the red, blue, and magenta colors are assigned to show the 2D arrays of the pump power, two-color seed, and ASE power spectra respectively.

The next block is the '*Calibration*' block. In this part of the program a created *Calibration* subroutine is called into the program to determine the emission and absorption values at the wavelengths of the pump laser, two-color seed, and ASE. For this, 2D arrays of $\sigma_e(\lambda)$ and $\sigma_a(\lambda)$ containing the cross section values for wavelengths from 850 nm to 1140 nm with a 0.1 nm resolution are called into the subroutine. $\sigma_e(\lambda)$ and $\sigma_a(\lambda)$ are displayed in Fig. 2.6. The *Calibration* subroutine extracts the $\sigma_e(\lambda)$ and $\sigma_a(\lambda)$ values for the 2D arrays of the pump laser, two-color seed, and ASE by looking up the wavelengths in the 2D arrays of $\sigma_e(\lambda)$ and $\sigma_a(\lambda)$. In the output of the *calibration* block, new 2D arrays of $\sigma_e(\lambda)$ and $\sigma_a(\lambda)$ are constructed for each propagating field. The new 2D arrays are shown with the grey line for the $\sigma_e(\lambda)$ and the green line for the $\sigma_a(\lambda)$.

Other values given to the program are the confinement factors: Γ_p, Γ_s, Γ_{ASE}, the dopant density N_t, the effective core area A, florescence life time τ, background absorption α, and time increment δt. The fiber segment δz has been preset to 1 mm in the program. In the length variation mode, the initial fiber length, final fiber length and fiber length increment are input values to the program. In the pump power variation mode, a subroutine is used to construct a Gaussian profile of the pump power as a function of wavelength. In this mode, three input values are given to the program to construct the Gaussian profile: central pump wavelength, bandwidth, and channel bandwidth and three other parameters are given to control the change of power: initial pump power, final pump power, and pump power increment.

A 1D array $\mathcal{N}(z,t)$ is constructed to store the upper state population density at each segment of the Yb:fiber. The $\mathcal{N}(z,t)$ array is zero in the beginning but it changes after

each iteration. The array dimension of $\mathcal{N}(z,t)$ increases as the fiber length increases.

In the '*Propagation Equation*' block, Eqs. 2.96, 2.99, 2.101, 2.103, and 2.105 are solved for each wavelength of the propagating pump, seed, and ASE fields. The output of this block is the power matrices given by Eqs. 2.97, 2.100, 2.102, 2.104, and 2.106. These power matrices are input to the '*Population Equation*' block where Eq. 2.107 is used to derive the upper state population density $\mathcal{N}(z,t)$ array.

In the '*Total Seed Power*' decision making block, the total output power of the seed signal is calculated by summing all elements in the last column of the seed-power matrix from Eq. 2.102. If its current value shows a variation by more than 0.05% compared to the previous value then the loop will start over again from the '*Propagation Equation*' block. Otherwise, all quantities shown in the flowchart will be stored in local variables and then plotted.

In the last decision making block, *i.e.* the '*Final Fiber Length or Final Pump Power*' block, the final fiber length (or the final pump power) is checked. If the current value is less than the input value, a move is carried out in the amount of fiber length increment (or pump power increment) and the program will start from the beginning. Otherwise, all plots are saved in the *.txt file format and the program will stop.

2.20 Conclusion

Two-color ultrafast laser systems with two synchronized output pulses are useful for example in pump-probe ultrafast spectroscopy and optical frequency combs generation. More, when the wavelengths of the two-color laser pulses are sufficiently far apart, they can be difference frequency mixed to generate short-pulse MIR radiation.

Yb:fiber amplifier offers 1- a gain bandwidth as broad as 210 nm when pumped at the wavelength 975 nm and 2- a high output average power. These properties are the most important reasons for using YDFA in the development of tunable two-color ultrafast system in this thesis.

Amplification of a two-color spectrum with the two colors separated as broad as the 210-nm gain spectrum in the watt-level from two-color ultrafast YDFA is a challenging task because of gain competition between the two colors and the amplified spontaneous emission. The gain competition becomes dramatic for the long wavelength side because of its very low emission cross section. A wavelength separation as large as 67 nm has been achieved between two amplified pulses from a two-color ultrafast YDFA system while the

average power on the long wavelength has been 20 mW [39]. As will be demonstrated in this thesis, a more carefully designed two-color Yb:fiber amplifier system will result in a larger wavelength separation (71 nm) between the two colors with a higher average power (more than 100 mW) on the long-wavelength pulses.

Considering the gain bandwidth, Ti:sapphire is a main competitor to the YDFA to be used in the two-color ultrafast laser systems. The broad gain bandwidth (670-1070 nm) of Ti:sapphire crystal has resulted in synchronized two-color pulses with a wavelength separation up to 120 nm [53]. Apart from its bulkiness and high cost, Ti:sapphire laser system is limited to a watt-level output average power at room temperature mainly due to Kerr lensing problem that occurs when it is pumped with high power lasers. Although this problem is resolved by cooling Ti:sapphire crystal, one has to use a cumbersome cryogenic system to obtain several ten-watt average power. In comparison, YDFA as a laser amplifier has a narrower gain bandwidth but it is superior in terms of average power. An astonishing average power of 830-W has been achieved from ultrafast YDFA systems with 640-fs, 78-MHz, 1042-nm output laser pulses [24].

Mid-infrared ultrafast laser sources that can be tuned over a large portion of spectrum of the molecular fingerprint (2.5-25 μm) are few. It is especially challenging to generate the long MIR wavelengths directly from solid-state laser gain media because most optical materials are opaque to these wavelengths. Alternatively, for the generation of tunable short-pulse MIR radiation up to the long-wavelength side, applying the difference frequency generation technique has resulted in: a maximum tunability range of 10-20 μm with a maximum average power of 300 μW from two-color ultrafast Ti:sapphire laser systems [52] and a maximum tunability range of 5.2-18 μm with a maximum average power of $\sim$ 100 μW from ultrafast optical parametric oscillator systems [65]. On the other hand, from mixing the output of two-color ultrafast YDFA systems, an average power of 400 μW on the short-pulse MIR radiation at the wavelength 17.5 μ has been reported [39] which is noticeably higher than that from the reported results from Ti:sapphire systems and OPO+DFG systems cited above. More, the average power of the two-color YDFA systems can be increased conveniently by incorporating high-power YDFAs in these systems to scale up the MIR power. Other techniques such as optical parametric generation and optical parametric amplification, are two competitors to the DFG-based short-pulse MIR generation. Optical parametric generation offers a tunability range for the MIR pulses as broad as DFG technique, however, the MIR output power is lower because of the absence of the input signal pulses. From the OPA technique, the tunability range for the MIR pulses is not as broad as the DFG technique due to the spectral bandwidth of the optical elements.

Currently, quantum cascade lasers are the state-of-art MIR laser sources. At the present

time, the tunability range of a single MIR QCL is not as abroad as that achieved from nonlinear frequency down conversion processes such as DFG. More, mode-locked MIR QCLs are not abundant mainly because of the fast gain recovery time. The generation of widely tunable short-pulse MIR radiation from DFG technique such as that presented in this thesis remains as a persistent technological solution for the applications such as ultrafast MIR spectroscopy.

In this chapter, a systematic approach was provided to model amplification of two-color ultrafast laser pulses in YDFA. The modeling is based on cw rate and propagation equations from existing laser theory. Also, McCumber theory was successfully used to extrapolate the experimental emission and absorption cross sections of ytterbium ions in the YDFA of Ref. [13] to be used in modeling. In the modeling, two types of Yb:fibers of the sort of single-clad and double-clad were considered differing in mode confinement factor for the pump lasers to the fiber core of the YDFAs. A LabVIEW program that has been created for this research was described in that the modeled equations are solved for digitized spectra of the two-color, pump laser, and the ASE fields. The program has a main task to calculate the power at each wavelength for each 1-mm-long segment of the YDFAs.

Chapter 3

Results of the modeling

This chapter is based on the following publications:

1. **M. Hajialamdari**, A. M. Alkadry, and D. Strickland. Modeling of a two-color, two-stage, ultafast Yb-doped fiber amplifier. *Opt. Commun.*, **284**, 2843, 2011.

2. **M. Hajialamdari** and D. Strickland. Tunable mid-infrared source from an ultrafast two-color Yb:fiber chirped-pulse amplifier. *Opt. Lett.*, **37**, 3570, 2012.

3.1 Introduction

This chapter includes the results of modeling to the amplification of a two-color seed signal in a two-stage two-color Yb:fiber amplifier system. The first amplifier stage consists of a single-clad single-mode Yb:fiber as of preamplifier and the second amplifier stage consists of a double-clad single-mode Yb:fiber as of main amplifier. For the modeling results presented in this chapter, I have used the LabVIEW simulation program for the complicated case of considering digitized spectra for the two-color seed signal, the pump laser, and the ASE. In Appendix B, I have also presented an analytical approach to obtain the saturation power of the seed signal in both single-clad and double-clad Yb:fiber amplifiers pumped at 975 nm considering a simple case that the pump and signal fields are single wavelength laser sources and there is no ASE. The seed saturation power from the analytical approach is used as a target value for the input two-color seed power to the main amplifier.

3.2 The preamplifier and main amplifier setup

Before presenting the modeling results, I explain the experimental setup of the preamplifier and main amplifier that have been modeled. Fig. 3.1 depicts the schematic of the experimental setup of the preamplifier stage. The preamplifier is a single-clad single-mode Yb:fiber amplifier. It is pumped from both ends by 975-nm laser diodes. There are four dichroic mirrors DM1 which are highly reflective at 975 nm and highly transmissive for wavelengths above 1030 nm. There are also two dichroic mirrors DM2 which are highly transmissive at 975 and highly reflective for wavelengths above 1030 nm. The laser diodes are collimated by the 10X microscope objective lenses. On the left hand side of the figure, after the DM2 mirror, the pump laser and a two-color seed signal are colinear and then focused into the fiber core by a 20X microscope objective lens. On the right hand side of the figure, the amplified seed signal is collimated by the 10X objective lens and then directed out of the amplifier setup by the DM2 mirror.

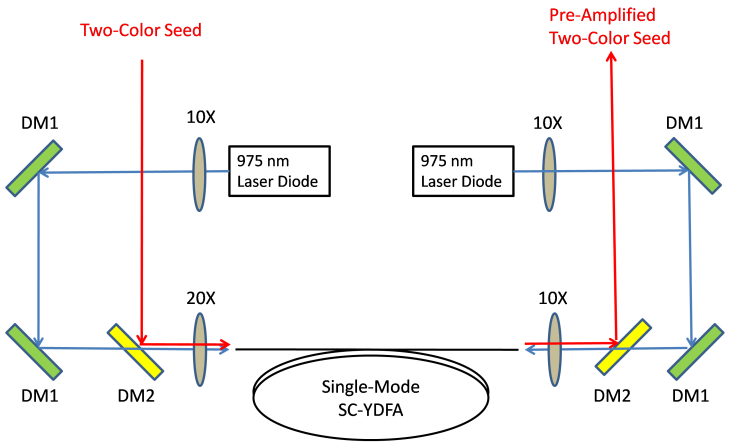

Figure 3.1: Schematic of the preamplifier stage.

The schematic of the experimental setup of the main amplifier is illustrated in Fig. 3.2. The main amplifier is a polarization maintaining double-clad single-mode Yb:fiber amplifier. It is counter-pumped by a 975-nm multimode laser diode at 6 W. The pump laser is collimated by the first 10X microscope objective lens and focused into the first cladding by the second 10X microscope objective lens. The two-color seed signal, output from the preamplifier stage, is injected into the fiber core using a 20X microscope objective lens.

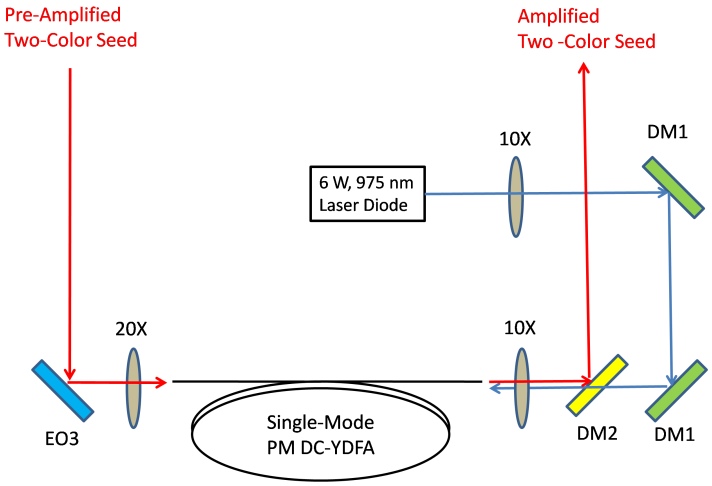

Figure 3.2: Schematic of the main amplifier stage.

3.3 Results of modeling of the preamplifier

In this section, I will present the modeling results on the two-color single-clad Yb:fiber as a preamplifier using the LabVIEW program. The key fiber parameters used in the modeling were given in Table 2.1. Furthermore, the fiber is divided into 1-mm-long segments [40], the time increment δt between iterations is 2 μs, the effective spontaneous emission time τ is 0.8 ms, the background absorption α of the fiber is 0.009 m^{-1} [40], the spectral range of the two color seed signal is within 1020 - 1115 nm, the spectral range of the ASE is from 1000 nm to 1130 nm, and the ASE spectrum is divided into 1-nm-bandwidth channels. The modeling is based on using single-mode 975-nm laser diodes with output powers of 150 mW and 500 mW. The modeling results on the 150-mW and 500-mW laser diodes will be presented in subsections 3.3.1 and 3.3.2 respectively.

3.3.1 Pumping by 150 mW laser diodes

We consider a single-clad Yb:fiber pumped from both ends by 975-nm, 150-mW laser diodes. The coupling efficiency of the pump lasers to the fiber is $\sim 30\%$, from experimental measurements, reducing the launched pump power to 45 mW for each laser diode. The coupling efficiency was low because of poor quality focusing lenses. Fig. 3.3(a) illustrates a 4-mW flat-top two-color seed spectrum centered at 1032:1108 nm. Each color has a 15-nm bandwidth and a 2-mW power. Fig. 3.3(b) illustrates the amplified seed spectrum from

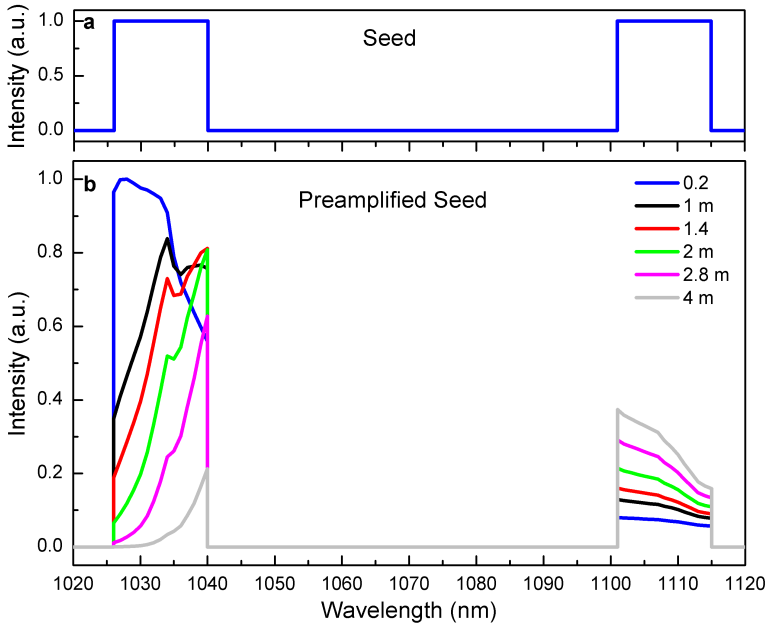

Figure 3.3: (a) The 4-mW flat-top two-color seed signal and (b) amplified seed spectrum from the single-clad YDFA pumped by 150-mW, 975-nm laser diodes from both ends.

fiber lengths 0.2, 1, 1.4, 2, 2.8, and 4 m. As can be seen, the short-wavelength color (will be called blue color) experiences gain narrowing as the fiber length increases from 0.2 m to 4 m. The short-wavelength side of the blue color is amplified in the beginning of the fiber, however, as the fiber length increases due to a high absorption cross section it is absorbed. Therefore, the gain is pulled toward the gain center. Eventually, the amplified blue color is almost absorbed from a 4-m fiber and the absorbed power is delivered to the long-wavelength color. From this figure, the long-wavelength color (will be called red color) is amplified as the fiber length increases from 0.2 m to 4 m and it experiences the gain pulling toward the gain center. The red color bandwidth decreases as the fiber length increases, however, the gain narrowing effect is dramatic for the blue color.

Fig. 3.4(a) depicts the pump transmission as a function of fiber length. As can be seen, the co-propagating and counter-propagating pump lasers are completely absorbed after traveling 40 cm in the fiber core. Fig. 3.4(b) depicts the amplified seed power at the wavelengths 1035 nm and 1105 nm as a function of fiber length. From this figure, the 1035-nm signal power increases to a maximum power of 3.6 mW from amplification in a 40-cm Yb:fiber and thereafter it decreases as the fiber length increases because of the absence of pump power. Also from this figure, the 1105-nm signal power increases

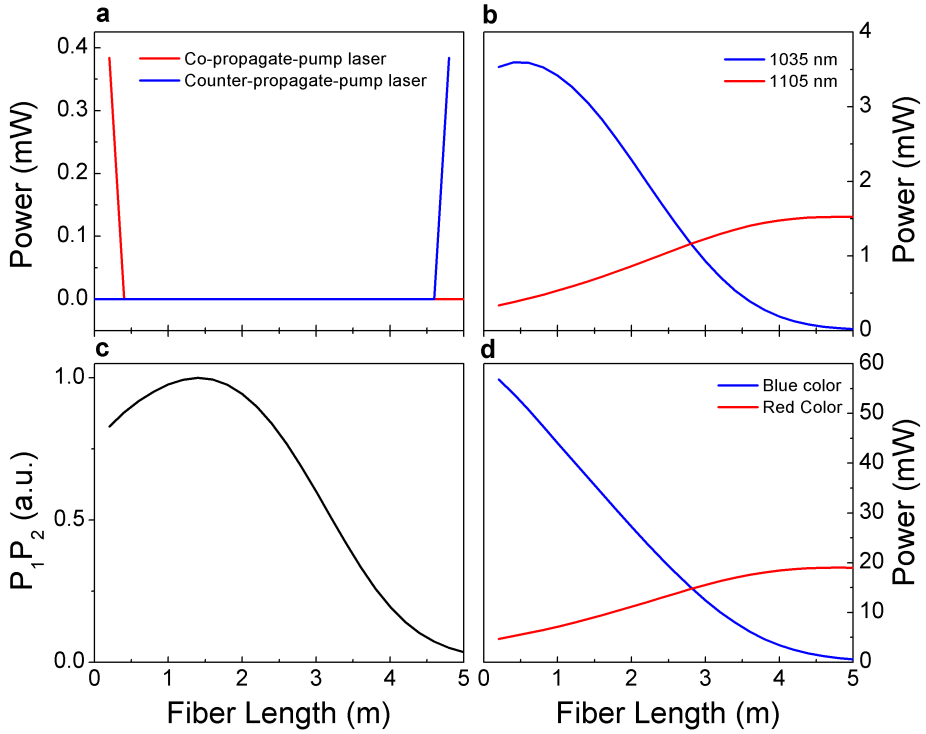

Figure 3.4: Variations of (a) the power of pump lasers (b) the power of the 1035-nm and 1105-nm amplified signals (c) the product of the power of the blue and red colors (d) the power of the blue and red colors as a function of fiber length from the single-clad Yb:fiber amplifier with launched pump power of 45-mW from each end.

monotonically to a maximum power of 1.5 mW. Fig. 3.4(d) depicts the total power at each color as a function of fiber length. From this figure, the power of the blue color is 57 mW from a 20-cm-long Yb:fiber and then it decreases as the fiber length increases. The power of the red color is 4.7 mW from a 20-cm-long Yb:fiber and it increases as the fiber length increases. Also from this figure, the blue color and red colors are amplified to the same power of 14.7 mW from a 2.8-m-long Yb:fiber. Fig. 3.4(c) depicts the product of the powers of the two colors, *i.e.* P_1P_2, as a function of fiber length. From this figure, P_1P_2 is maximized from a 1.4-m-long Yb:fiber. The 1.4-m-long Yb:fiber could be useful for the DFG-based MIR generation because the MIR power scales up with the P_1P_2.

Fig. 3.5(a) illustrates the forward-traveling ASE in the direction of the seed signal. From this figure, as the fiber length increases the ASE is gain pulled toward the gain center and it is intensified (note the increased FWHM of the spectrum). The backward-

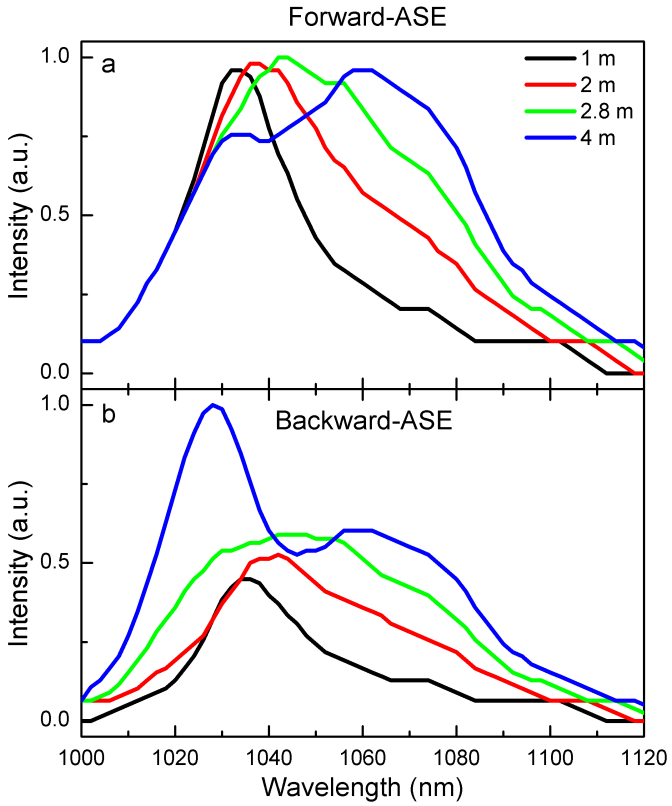

Figure 3.5: Variations of the (a) forward-traveling and (b) backward-traveling ASE spectra for different Yb:fiber lengths from the single-clad Yb:fiber amplifier pumped by 150-mW laser diodes from both ends.

traveling ASE is shown in Fig. 3.5(b). From this figure, as the fiber length increases, the generated ASE is intensified on the short wavelength-side of the spectrum. This is because of high pump power in the beginning of the fiber as well as high emission cross section for the short wavelengths resulting to a high gain value at left shoulder of the ASE spectrum.

Fig. 3.6(a) shows the variations of the total amplified power of the two-color spectrum as a function of fiber length. From this figure, the total power decreases almost linearly from 60 mW to 30 mW and then it exponentially decreases very slowly. This behavior is a result from the net behavior of the blue and red colors shown in Fig. 3.4(d). From Fig. 3.6(b), the total ASE power increases to ~ 0.7 mW from a 4-m-long Yb:fiber. From this figure, from a 2.8-m-long Yb:fiber, the total generated ASE is 2% of the amplified two-color signal.

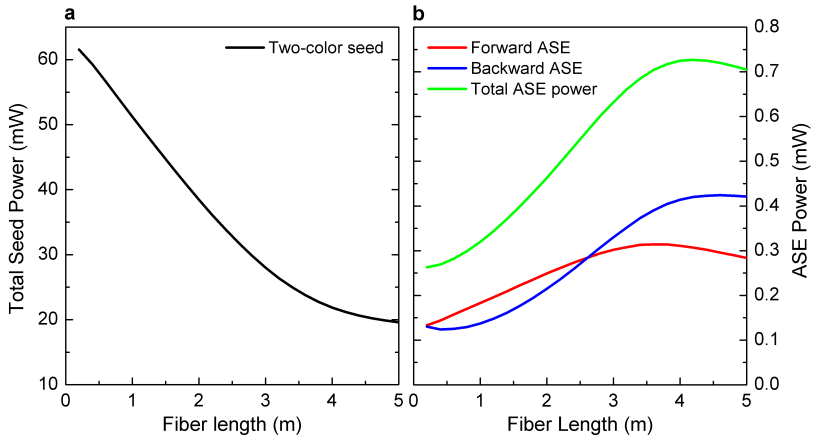

Figure 3.6: Variations of the total (a) amplified power of the two-color seed spectrum and (b) ASE power as a function of fiber length from the single-clad Yb:fiber amplifier pumped by 150-mW laser diodes from both ends.

In order to model the preamplifier under real conditions, an experimental two-color seed spectrum has been used instead of the flat-top two-color spectrum. Fig. 3.7(a) depicts a 3-mW experimental seed signal with 1:1 peak power at wavelengths of 1035 nm and 1105 nm used in the numerical simulations of the preamplifier fiber. From this figure, the short and long wavelength spectra extend from 1020 nm to 1042 nm and from 1101 nm to 1118 nm respectively. Fig. 3.7(b) depicts the preamplified power spectra obtained from simulation (red line) and experiment (blue line) from a 2-m-long, single-clad, Yb:fiber. The average power including ASE in both spectra is ∼30 mW. As can be seen, the power spectrum obtained from the simulation matches that from experiment with some more significant deviations around 1105 nm. These deviations are mainly related to the variations of the input seed signal in the course of time. Simultaneous measurements of the seed and amplified signal could be carried out with angled glass slides to achieve an exact match between spectra. From this figure, long wavelengths centered at 1105 nm are less amplified than short wavelengths centered at 1035 nm from the 2-m-long fiber. Because of a higher re-absorption rate for short wavelengths, fiber lengths longer than 2 m are suggested to lower the short-wavelength intensities for the generation of a two-color amplified spectrum with an equally distributed power between the two colors. This can be seen more clearly from variations of gain at the two center wavelengths as a function of fiber length in Fig. 3.7(c). As can be seen, the gain of the short wavelength at the beginning of the fiber is almost three times bigger than that of the long wavelength. However, the preamplifier gain increases for the long wavelengths and decreases for the short wavelengths as fiber

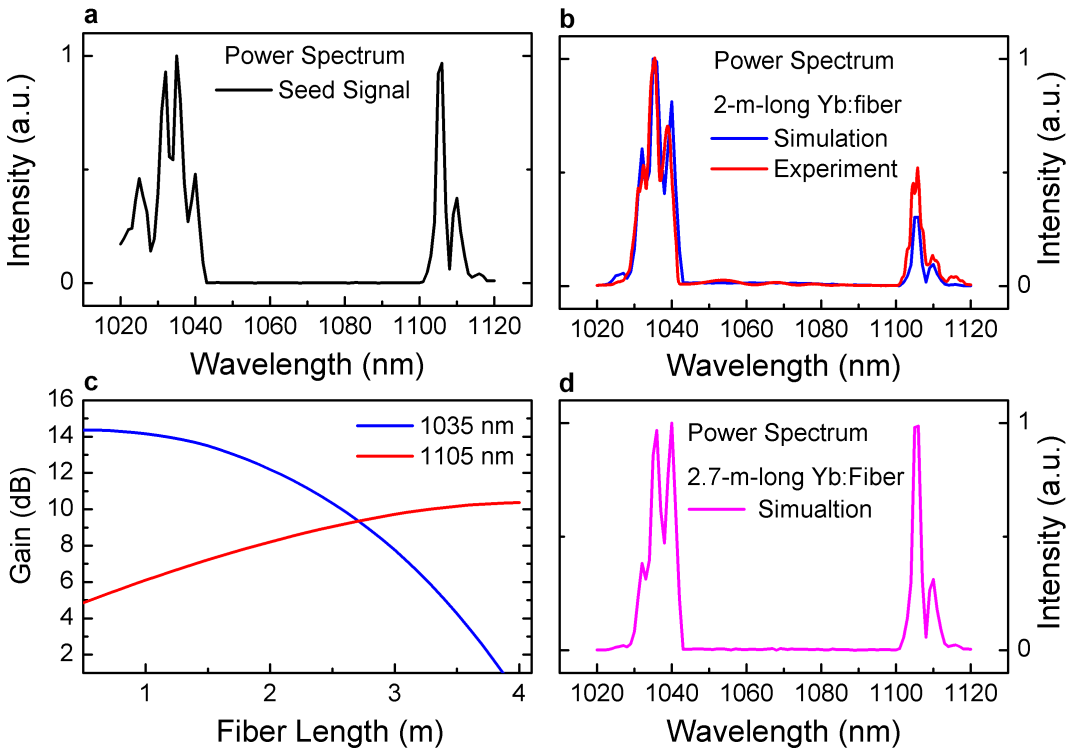

Figure 3.7: Simulation results to the single-clad Yb:fiber amplifier pumped by 150-mW laser diodes from both ends and seeded by an experimental two-color seed spectrum; (a) Experimental two-color seed spectrum used in the simulations, (b) preamplified two-color seed spectrum from a 2-m-long Yb:fiber, (c) simulation to gain profile at 1035 nm and 1105 nm as a function of Yb:fiber length, and (d) simulation to the preamplified power spectrum of the two-color seed spectrum from a 2.7-m-long preamplifier. (published in Ref. [93]).

length increases. This trend continues until at the fiber length of 2.7 m where the two gain numbers are identical. Fig. 3.7(d) shows the simulation to the preamplified power spectrum from a 2.7-m-long preamplifier with the same pumping and seeding parameters of the 2-m simulation. As can be seen, the two colors have been amplified to the same peak power at this fiber length. This panel also shows that the short wavelength spectrum has been red-shifted as expected from the increased gain at the longer wavelengths. The total preamplified power for the 2.7-m-long fiber has decreased to 23 mW from 30 mW for the 2.0-m-long fiber, agreeing with the experimental results [93]. We also notice that there is an agreement on the simulation results to the optimum fiber length between seeding with an experimental two-color seed spectrum and with a flat-top two-color seed spectrum.

From crude calculations (see Appendix B), the saturation power on the 1035 nm is 14 mW and on the 1105 nm is 51 mW nm in the main amplifier. Thus, the 23-mW average power from the preamplifier is not sufficient to extract maximum power from the main amplifier. In practice, between the preamplifier and main amplifier, there exist a notch filter to remove the ASE from the preamplified signal and a Faraday isolator to protect the preamplifier from backward-traveling ASE originated from the main amplifier. In our setup, this combination reduces the preamplified power by 70%. Due to this power reduction, we have obtained a nominal 6-mW average power on the seed signal before the main amplifier which is less than the seed saturation power by one order of magnitude. Increasing the two color seed power to the main amplifier dramatically lowers the generated ASE from the main amplifier. In the following, I will present the modeling results on the preamplifier using 500-mW laser diodes. Furthermore, the simulation results will be compared with experimental results.

3.3.2 Pumping by 500 mW laser diodes

In the improved setup of the preamplifier pumped by single-mode 500-mW 986-nm laser diodes, the pump power coupling efficiency increased after replacing the focusing lenses. For the simulation to give us reliable results, it was required to determine the pump power coupling efficiency. Here, I will present the simulation and experimental results by which I have determined the pump power coupling efficiency to the preamplifier.

Fig. 3.8 depicts the total power of the backward-traveling ASE as a function of launched pump power from simulation and experimental results from a 7.5-m-long single-clad Yb:fiber when there is no input signal and in a single-sided pumping scheme. For the simulation, the LabVIEW program mode is the *power mode*. In order to match the modeled ASE power with the experimental ASE power, the output power of the laser diode was multiplied by 1/2 giving us a coupling efficiency of 50% for the pump laser.

Figs. 3.9(a) and 3.9(b) compare the ASE power spectra from simulation and experiment with no input seed. Fig. 3.9(a) depicts the simulation and experimental results to the power spectrum of the forward-traveling ASE with a launched pump power of 220 mW in a single-sided pumping scheme from a 7.5-m-long single-clad Yb:fiber. Fig. 3.9(b) depicts the simulation and experimental results to the power spectrum of the backward-traveling ASE with a launched pump power of 80 mW in a single-sided pumping scheme from a 7.5-m-long single-clad Yb:fiber. As can be seen, the modeled power spectra agree very well with the experimental power spectra.

Figs. 3.10(a) and 3.10(b) illustrate the variations of pump power transmission as a

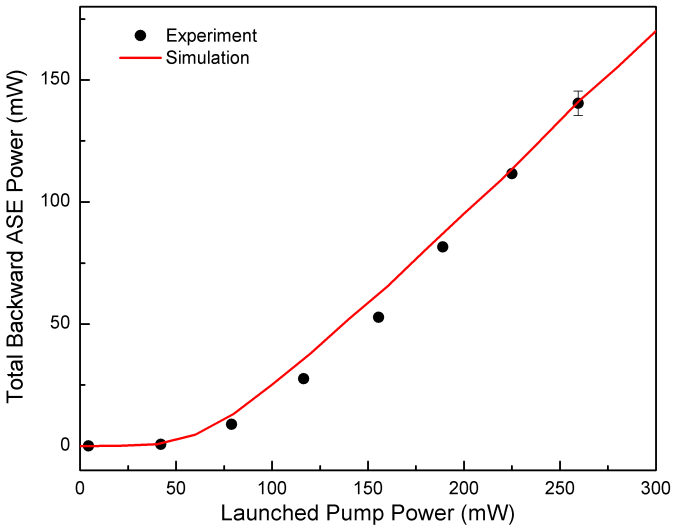

Figure 3.8: The simulation and experimental results to the total power of backward-traveling ASE from a 7.5-m-long single-clad Yb:fiber amplifier pumped from one end by a 500-mW, 986-nm laser diode with no input seed. The horizontal axis is the launched pump power in the modeling.

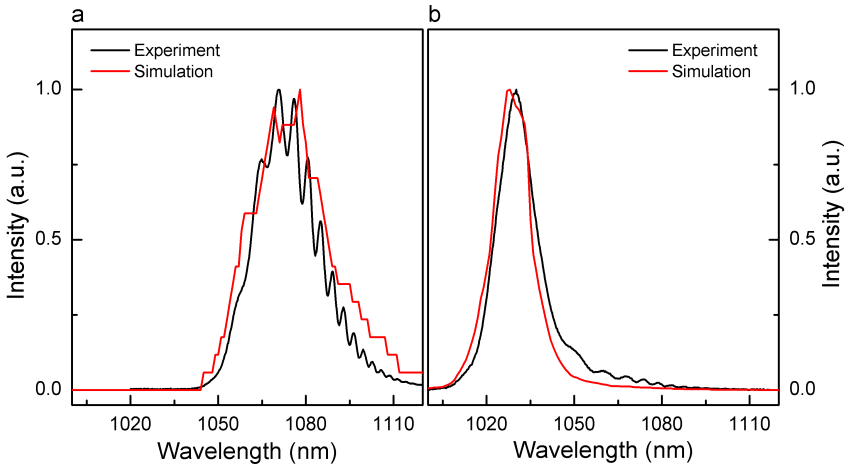

Figure 3.9: The simulation and experimental results to the power spectra of the (a) forward-traveling ASE and (b) backward-traveling ASE from a 7.5-m-long single-clad Yb:fiber amplifier pumped from one end by a 500-mW, 986-nm laser diode with no input seed.

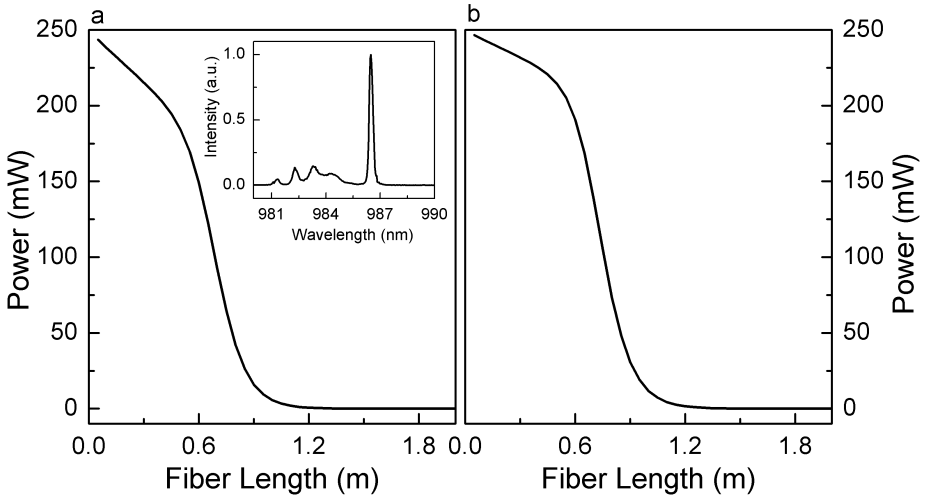

Figure 3.10: Simulation results to the pump power transmission as a function of Yb:fiber length from a single-clad Yb:fiber amplifier pumped from (a) one end and (b) both ends by 500-mW, 986-nm laser diodes with no input seed. The inset graph shows the measured power spectrum of the laser diodes.

function of fiber length in the single-sided and double-sided pumping schemes respectively pumped by 500-mW, 986-nm laser diodes with no input seed. As can be seen, the pump power is largely absorbed for fiber lengths longer than 1 m. From these figures, the pump absorption is slightly different for the fiber lengths shorter than 0.6 m for the two pumping schemes. From these short fiber lengths, for the double-pumping scheme, the forward-traveling pump laser experiences less absorption because of the backward traveling pump laser. The inset graph shows measured power spectrum of the laser diode operated at 500 mW which has been used in the modeling. From this figure, the peak wavelength of the pump laser is 986 nm.

When a long preamplifier is operated without an input seed signal, the output is merely ASE. The power of the generated ASE gives a good estimate of a preamplified seed signal when the seed signal is high enough because of the gain competition in Yb:fibers. Fig. 3.11 depicts the simulation results to the ASE power as a function of Yb:fiber length from a single-clad Yb:fiber amplifier pumped by 500-mW, 986-nm laser diodes in single-sided and double-sided pumping schemes without seeding. From this figure, the generated powers of the forward- and backward-traveling ASE in the double-sided pumping scheme are the same because of the symmetrical pumping scheme, assuming identical pump power in the fiber from each laser diode. In the double-sided pumping scheme, the ASE power is 193

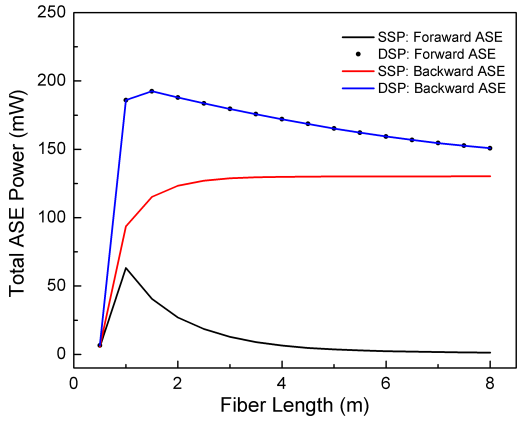

Figure 3.11: Simulation results to the ASE power as a function of fiber length from a single-clad Yb:fiber amplifier pumped by 500-mW, 986-nm laser diodes in single-sided and double-sided pumping schemes without seeding. (SSP: single-sided pumping, DSP: double-sided pumping.)

mW from each fiber end from a 1.5-m-long single-clad Yb:fiber and it decreases to 153 mW from a 7.5-m-long fiber. In the single-sided pumping scheme, the output power of the forward-traveling ASE is much lower than the output power of the backward-traveling ASE for the fiber lengths above 1 m. This is because of depletion of the pump power as the fiber length increases. From this figure, the output power of the backward-traveling ASE in the single-sided pumping scheme shows a plateau of 130 mW for fiber lengths above 2 m.

Figs. 3.12(a) and 3.12(b) display the simulation results to the power spectra of the forward-traveling and backward-traveling ASE respectively, from a single-clad Yb:fiber amplifier pumped by a 500-mW, 986-nm laser diode in a single-sided pumping scheme without seeding. From Fig. 3.12(a), the peak maximum of the forward-traveling ASE shifts from 1029 nm to 1034 nm as the fiber length increases from 0.5 m to 2 m. From this figure, the froward-traveling ASE spectrum is almost diminished from a 7.5-m-long fiber because of depletion of pump power. From Fig. 3.12(b), the location of the 1033-nm peak maximum of the backward-traveling ASE spectrum is not sensitive with the fiber length. From this figure, the backward-traveling ASE spectrum from a 7.5-long fiber is almost the same as that from a 2-m-long fiber resembling the 130-mW plateau in Fig. 3.11.

Figs. 3.13(a) and 3.13(b) display the simulation results to power spectra of the forward-traveling and backward-traveling ASE respectively, from a single-clad Yb:fiber amplifier pumped by 500-mW, 986-nm laser diode in a double-sided pumping scheme without seed-

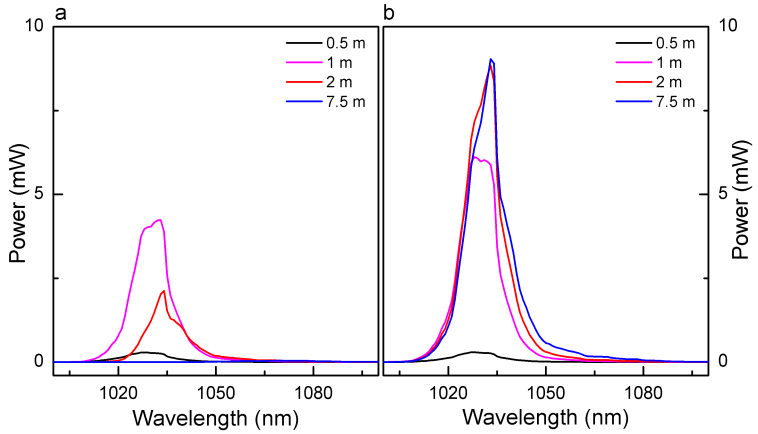

Figure 3.12: Simulation results to the power spectrum of the (a) forward-traveling ASE and (b) backward-traveling ASE from a single-clad Yb:fiber amplifier pumped by a 500-mW, 986-nm laser diode in a single-sided pumping scheme without seeding.

ing. As can be seen, the power spectra of the forward-traveling ASE is the same as backward-traveling ASE, an expected result from the symmetrical pumping scheme. From these figures, the peak maximum shifts from 1029 nm to 1034 nm as the fiber length increases from 0.5 m to 2 m. For the 7.5-m-long fiber, the spectrum centered at 1034 nm has largely decreased because of the large re-absorption at these wavelengths. More interestingly, a new spectrum centered at 1060 nm has appeared which is a consequence of gain

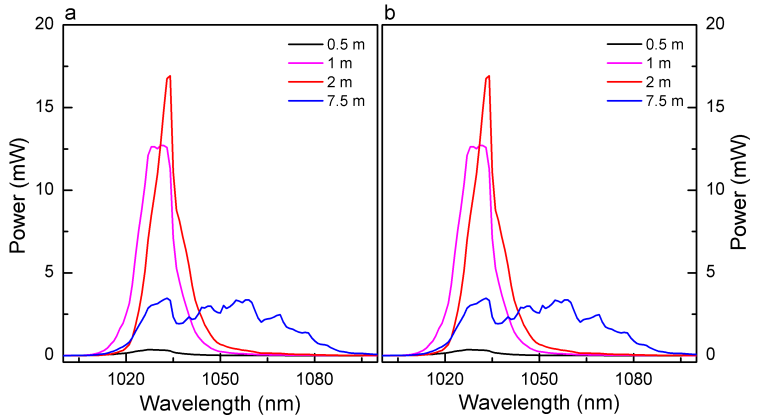

Figure 3.13: Simulation results to power spectra of the (a) forward-traveling ASE and (b) backward-traveling ASE from a single-clad Yb:fiber amplifier pumped by 500-mW, 986-nm laser diodes in a double-sided pumping scheme without seeding.

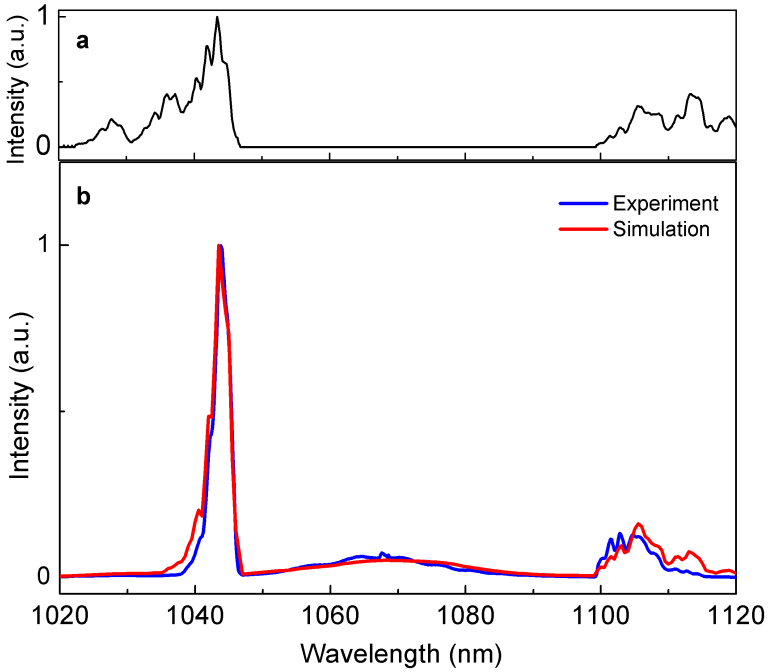

Figure 3.14: (a) An experimental two-color seed spectrum. (b) Preamplified seed spectrum from a 7.5-m-long Yb:fiber pumped from both ends. (Published in Ref. [96].)

shifting toward the gain center. The 1060 spectrum was not observed in the single-sided pumping scheme because of depletion of the forward traveling pump laser. Now, with the backward-traveling pump laser, a large portion of the YDFA gain profile shows up.

Fig. 3.14(a) depicts an experimental two-color seed spectrum with an average power of 2.5 mW distributed at a ratio of 4:1 between the blue and red colors. The blue color extends from 1030 nm to 1047 nm and the red color extends from 1100 nm to 1120 nm. The blue color peaks at 1043 nm and the red color peaks at 1106 nm. This two-color seed spectrum has been used in the numerical modeling of the two-color single-clad Yb:fiber amplifier in order to find the optimized fiber length of the preamplifier. Fig. 3.14(b) depicts the simulation and experimental power spectra from a 7.5-m-long single-clad Yb:fiber co-pumped by 350-mW and counter-pumped by 500-mW from 986-nm laser diodes. Lasing action occurred in the preamplifier at higher pump powers. From Fig. 3.14(b), the amplified blue color peaks at 1043 nm and the red color peaks at 1105 nm. The spectrum between 1048 nm and 1100 nm is ASE. As can be seen, the simulated power spectrum conforms suitably with the experimental power spectrum. From simulation, the total power including ASE is 200 mW with a power distribution of (95:95) mW on the blue:red colors and 10 mW

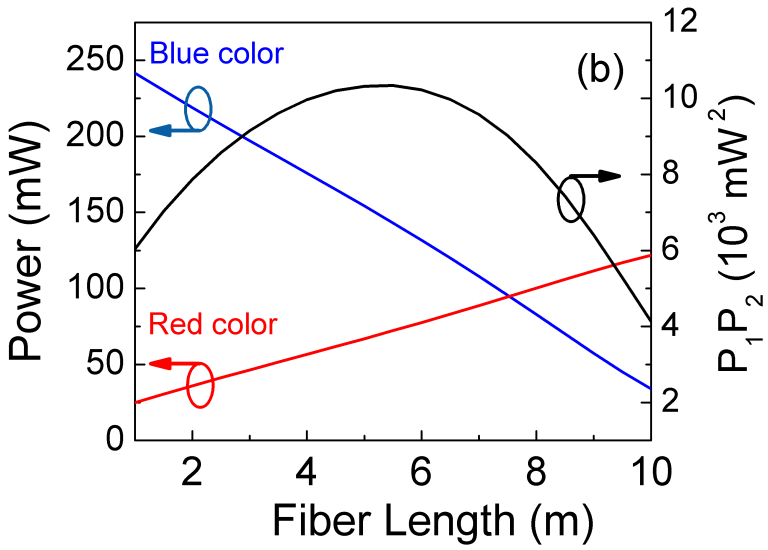

Figure 3.15: Simulation results to variations of the preamplified power of the blue and red colors as well as their product as a function of fiber length. (Published in Ref. [96].)

on the ASE extending from 1048 nm to 1100 nm agreeing very well with the 200-mW measured total power. From this figure, we observe gain narrowing on the blue color. The gain narrowing on the blue color is because of the steep gain profile of the YDFA at the blue-color side. The spectrum of the red color has been blue shifted toward the gain center. The pronounced gain narrowing on the blue color becomes more problematic by increasing the preamplifier fiber length or increasing the pump power imposing a limitation on the bandwidth of the blue color.

Fig. 3.15 shows the simulation results to variations of the preamplified power of the blue and red colors as well as their product (curved line) P_1P_2 as a function of fiber length. As can be seen, the blue color power is maximum (250 mW) at 1 m and it decreases as the fiber length increases. This is because the pump power is depleted quickly in the beginning of the fiber. Moreover, due to high absorption on the short wavelength side, the blue color is absorbed by ytterbium ions as it travels further in the pump-depleted fiber. The red color has minimum power at 1 m due to a lower gain but the absorbed power from the blue color is delivered to the red color as the fiber length increases. From this figure, the power at the two colors is equal with a value of 95 mW at the 7.5-m fiber length. As can be seen, P_1P_2 is maximized at 5.5 m. Therefore, for a single stage YDFA, 5.5 m would be the optimal fiber length. However, numerical modeling on the main amplifier reveals that the 5.5 m is not an optimal fiber length for the preamplifier in a two-stage YDFA system.

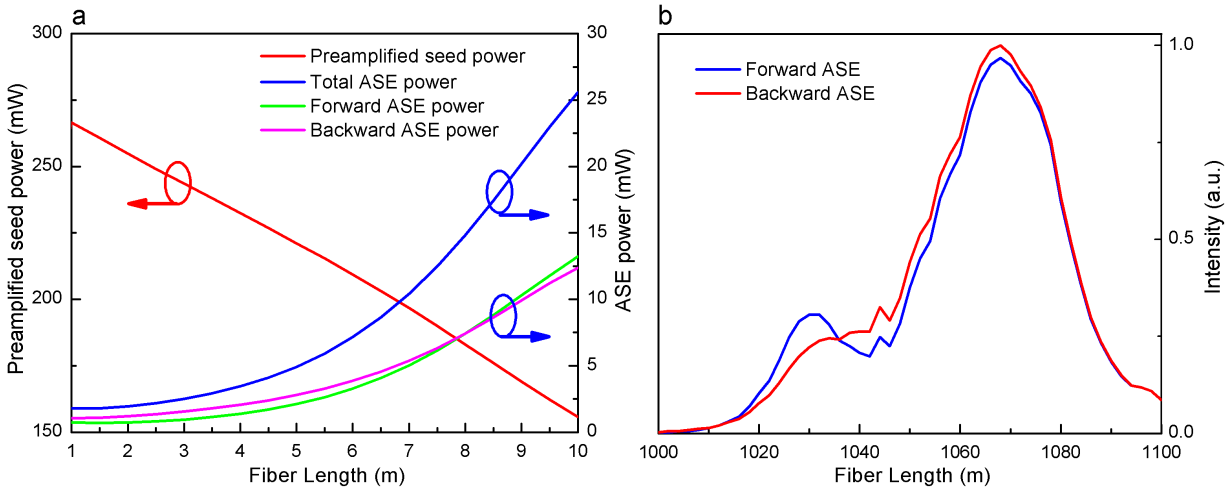

Figure 3.16: Simulation results to (a) variations of the preamplified two-color seed power and ASE power as a function of preamplifier fiber length and (b) ASE power spectra from a 7.5-m-long preamplifier. The two-color seed spectrum is that from Fig. 3.14(a).

This will be discussed in the modeling of the main amplifier.

Fig. 3.16(a) illustrates the simulation results to variations of the power of the preamplified two-color seed, forward-traveling and backward-traveling ASE fields, and total ASE filed as a function of preamplifier fiber length. From this figure, the total signal power decreases as the fiber length increases as a result of absorption of the blue color. The absorbed power of the blue color is delivered to the red color and the ASE field. As can be seen, the forward- and backward-traveling are both intensified as the fiber length increases. Also, the forward- and backward-traveling ASE fields show almost the same behavior. Comparing this figure with Fig. 3.11, the generated power from the backward ASE or forward ASE has decreased by a factor of 25 from a 7.5-m-long preamplifier fiber. From this figure, at a 7.5-m-long preamplifier fiber, the signal power of the two-color seed spectrum has increased from 2.5 mW to 190 mW and the total ASE power is 12.5 mW. Fig. 3.16(b) shows the power spectra of the forward- and backward-traveling ASE from a 7.5-m-long preamplifier. As can be seen, both modeled ASE spectra show almost the same profile. From this figure, the ASE power is maximum at the wavelength 1070 nm which is attributed to the gain maximum of the 7.5-m-long single-clad YDFA.

3.4 Results of the modeling of the main amplifier

In this section, I will present the results to modeling of the two-color double-clad Yb:fiber as a main amplifier using the LabVIEW program. The key fiber parameters used in the modeling were given in Table 2.1. Also, the background absorption α of the fiber is 0.009 m^{-1} for all wavelengths, the fiber is divided into 1-mm-long segments, the time increment δt between iterations is 2 μs, the effective spontaneous emission time τ is 0.8 ms. In the modeling, the pump laser is a 976-nm multimode laser diode with an output power of 6 W. The coupling efficiency of the pump laser to the first fiber cladding obtained from measurements is 60%. The propagation of the pump laser and two-color seed signal in the fiber is in a counter-propagating configuration as was shown in Fig. 3.2.

The main frame of Fig. 3.17 illustrates the simulation results to transmission of the 3.6-W launched pump power in the double-clad Yb:fiber as a function of fiber length without seeding. As can be seen, the pump power is almost zero from a 10-m-long fiber indicating a high power extraction efficiency can be achieved when the fiber is seeded. The spectrum of the pump laser is shown in the inset graph.

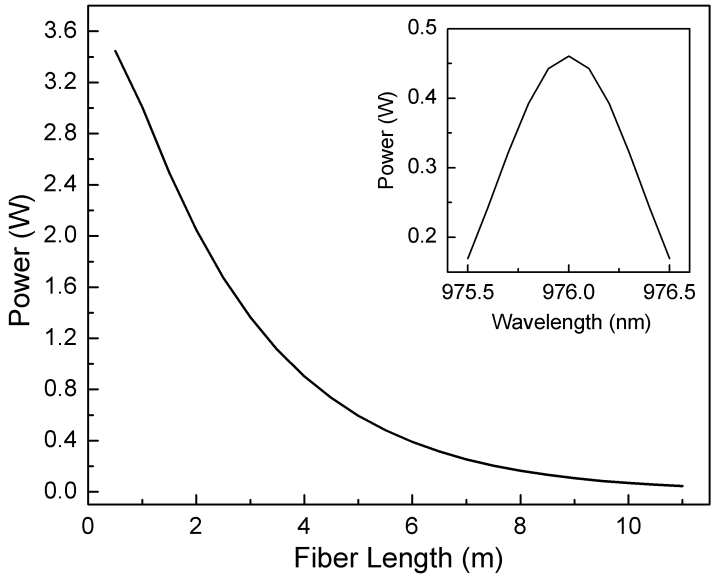

Figure 3.17: Simulation results to pump power transmission as a function of main amplifier fiber length. Inset graph shows the power spectrum of the 3.6-W multimode laser diode used in the modeling.

Figs. 3.18(a) and 3.18(b) show, respectively, simulation results to the forward-traveling

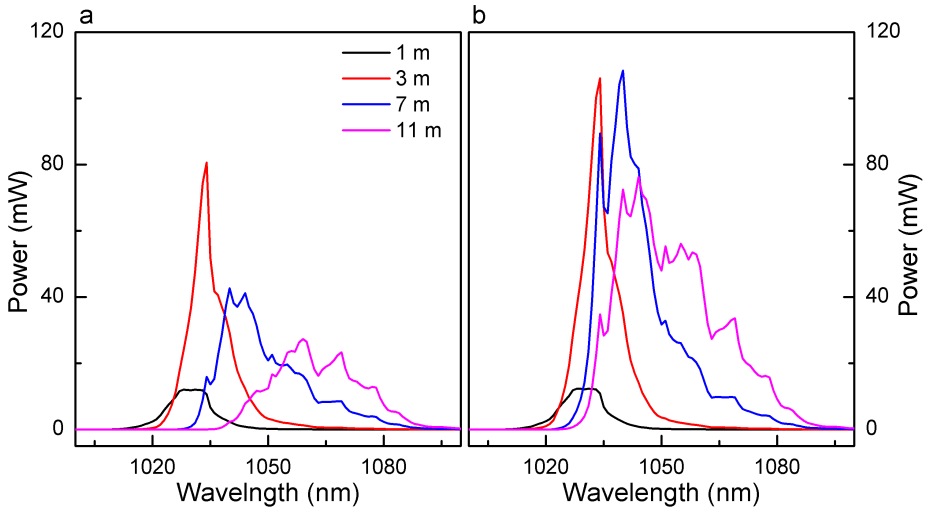

Figure 3.18: Simulation results to (a) forward-traveling and (b) backward-traveling ASE spectra for different amplifier fiber lengths with a 3.6-W launched pump power without seeding.

and backward-traveling ASE spectra for different amplifier fiber lengths with a 3.6-W launched pump power without seeding. In the modeled ASE spectra, the spectral range of the ASE is from 1000 nm to 1140 nm. This spectral range is divided into channels with a 1-nm bandwidth. From both figures, for short fiber lengths, the generated ASE is centered around 1034 nm. As the fiber length increases the ASE spectra are gain pulled toward the gain center at 1060 nm. From these figures, the backward-traveling ASE spectrum is more powerful compared to the forward-traveling ASE.

Fig. 3.19 display the simulation to variations of the ASE power as a function of amplifier fiber length related to the results shown in Fig. 3.18. From this figure, for fiber lengths shorter than 1.5 m, the forward ASE and backward ASE have almost the same power. For fiber lengths more than 1.5 m, the backward-ASE power continuously becomes larger than the forward-ASE power. The forward-ASE power decreases for fiber lengths longer than 5.5 m as a result of pump depletion. From this figure, the forward-ASE power is 680 mW and the backward-ASE power is 2060 mW from an 11-m-long amplifier fiber.

In the modeling of the two-stage two-color Yb:fiber amplifier system, the seed spectrum to the main amplifier is the output spectrum from the preamplifier. The seed coupling efficiency from the preamplifier to the main amplifier is estimated to be $\sim$ 12%. In the experimental setup, there are two notch filters and a Faraday isolator between the preamplifier and main amplifier. The notch filters are used to remove ASE between the two

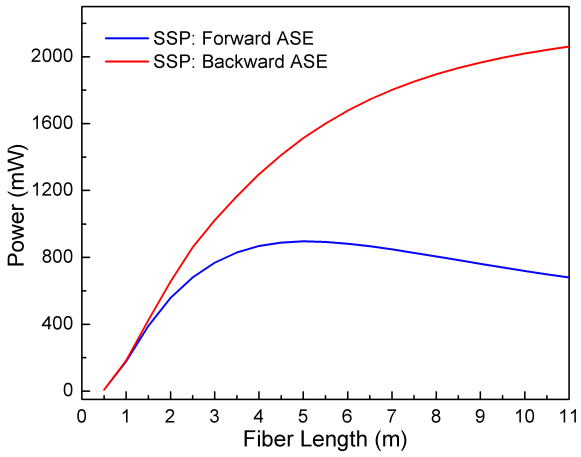

Figure 3.19: Simulation results to total power of the forward- and backward-traveling ASE as a function of amplifier fiber length with 3.6-W launched pump power without seeding.

colors and the Faraday isolator is used to block backward traveling ASE from the main amplifier to the preamplifier. The seed signal experiences a 50% loss after passing through each of these optical components.

In the modeling of the two-stage two-color Yb:fiber amplifier system, the goal is to find both the optimized preamplifier fiber length and the main amplifier fiber length. For this, the preamplifier fiber length varies between 5.5 m and 10 m at each 0.5-m step and different spectra are obtained. Fig. 3.20 illustrates the seed spectra to the main amplifier selected from modeled 5.5-, 7.5-, and 9.5-m-long preamplifier fibers. The spectral range of the two color seed signal is in the wavelengths 1025-1120 nm with a 0.5-nm resolution. From this figure, the total power of the two-color seed spectrum after applying the 12.5% reduction is 26, 23, and 20 mW from the modeled preamplifier fiber with a fiber length 5.5, 7.5, and 9.5 m respectively.

Fig. 3.21(a) illustrates the main amplifier output using the 7.5-m spectrum from the preamplifier. From this figure, by increasing the fiber length up to 5 m, the amplifier mostly increases the power of the blue color centered at 1044 nm. For fiber lengths above 5 m, the red color centered at 1105 nm picks up power while the blue color loses its power. By increasing the fiber length to 15 m, the amplifier output is mostly at the red-color wavelengths. Figs. 3.21(b) and (c) illustrate the forward-traveling and backward-traveling ASE spectra respectively. From these figures, the ASE spectrum is centered at 1070 nm and it becomes more powerful as the amplifier fiber length increases. The ASE spectrum shows negligible power at the blue- and red- color wavelengths.

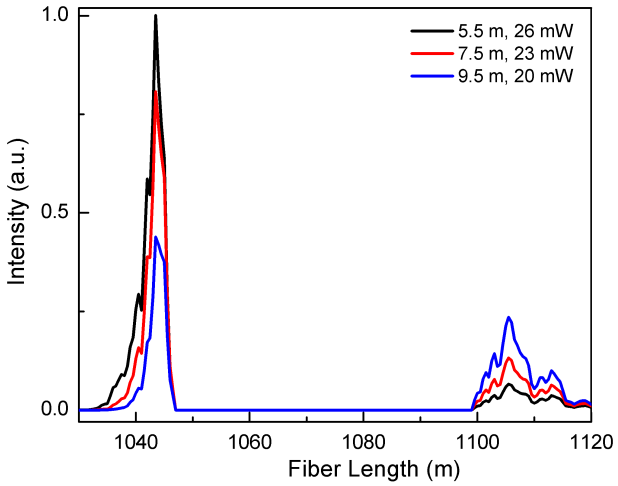

Figure 3.20: Two-color power spectra from the modeled preamplifier used for modeling the two-color main amplifier.

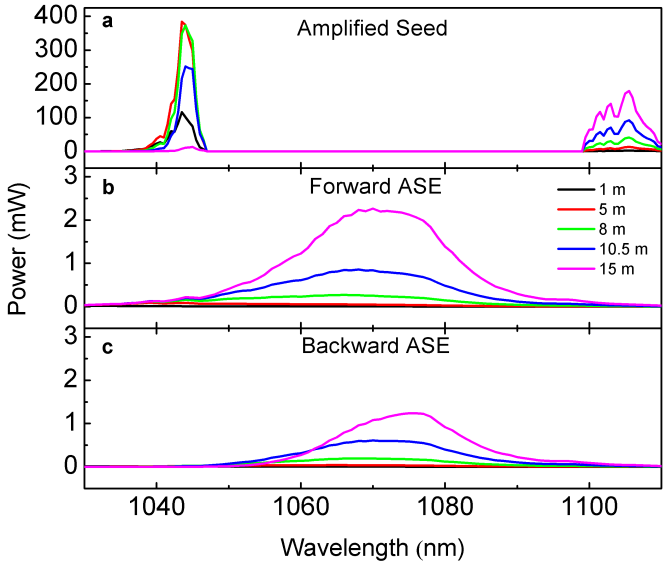

Figure 3.21: (a) Two-color power spectra from the modeled main amplifier seeded with the output from a modeled 7.5-m-long preamplifier, (b) power spectra of modeled forward-traveling ASE, and (c) power spectra of modeled backward-traveling ASE.

Fig. 3.22 depicts the variations of the amplified power of the blue and red colors as well as their product as a function of amplifier fiber length from the modeled main amplifier

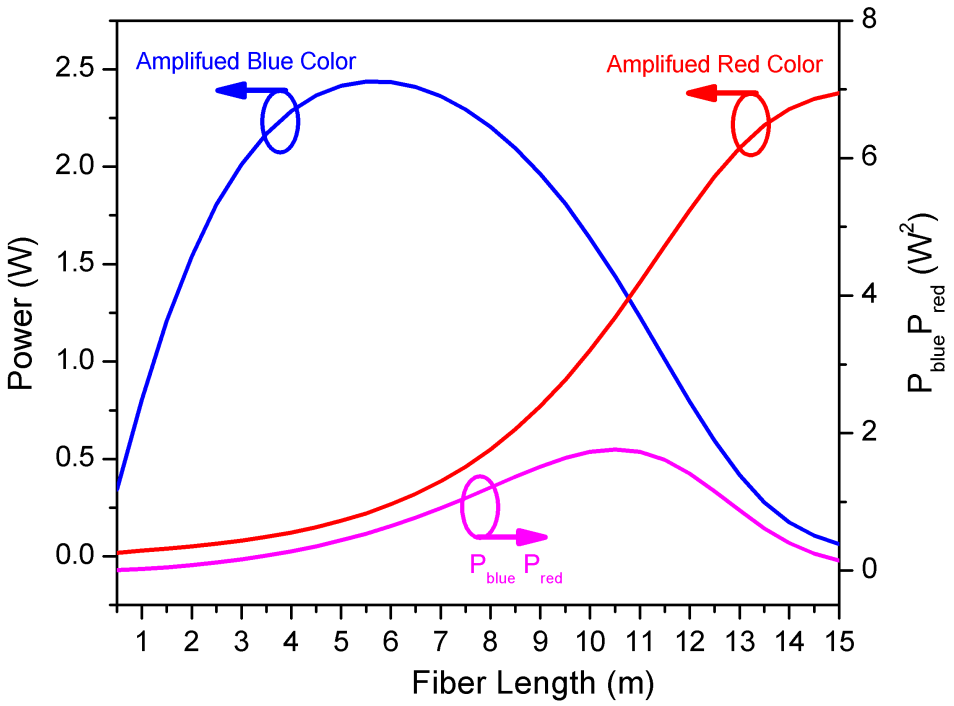

Figure 3.22: Variations of the amplified power of the blue and red colors as well as their product as a function of amplifier fiber length from the modeled main amplifier seeded by the output from the 7.5-m-long preamplifier.

seeded by the output from the 7.5-m-long preamplifier. From this figure, the power of the blue color is maximized to a value of 2.4 W from a 5.5-m-long amplifier fiber. The power of the red color monotonically increases as the fiber length increases. From a 15-m-long amplifier fiber, the power of the red color reaches to 2.4 W. The power of the two colors is equal to a value of 1.3 W from a 10.75-m-long amplifier fiber. The product of power of the two colors $P_{blue}P_{red}$ is maximized from a 10.5-m-long amplifier fiber. At this amplifier fiber length, the power of the amplified blue color is 1.44 W and the power of the amplified red color is 1.23 W. The 10.5-m-long amplifier fiber is the optimized amplifier fiber length in relate to the 7.5-m-long preamplifier fiber length useful for the MIR generation.

Fig. 3.23 depicts the variations of the power of the amplified two-color spectrum, forward-traveling ASE, backward-traveling ASE and total ASE as a function of fiber length from the modeled main amplifier seeded by the output from a 7.5-m-long preamplifier. From this figure, the total power of the amplified two-color signal is maximized from a 7.5-m-long amplifier fiber. At the 10.5-m-long fiber, the total output power of the two-color

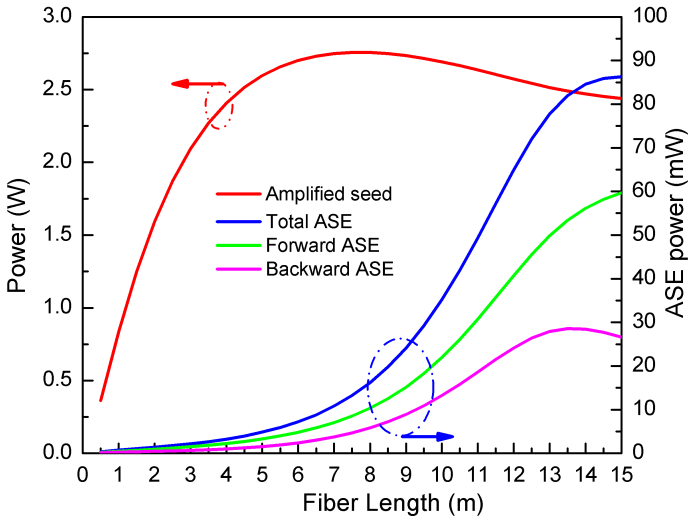

Figure 3.23: Variations of the power of the amplified two-color spectrum, forward-traveling ASE, backward-traveling ASE and total ASE as a function of fiber length from the modeled main amplifier seeded by the output from a 7.5-m-long preamplifier.

signal is 2.67 W and the power of the forward-, backward-, and total ASE is 26, 16, and 42 mW respectively.

Simulations have been carried out to find the maximized P_1P_2 from the main amplifier for different preamplifier fiber lengths as was demonstrated for the 7.5-m-long preamplifier fiber. Fig. 3.24 illustrate the simulation results to the maximized P_1P_2 from the main amplifier as a function of preamplifier fiber length. From this figure, when the preamplifier fiber length is 5.5 m, P_1P_2 is maximized from a 12.5-m-long main amplifier fiber. The maximized P_1P_2 then increases as the preamplifier fiber length increases to 9.5 m where it is at the peak maximum (10% above the 5.5-m result) from an 8.5-m-long main amplifier fiber and afterwards it decreases by increasing the preamplifier length.

The final decision on the optimized fiber lengths should consider the gain narrowing problem on the blue color. From Fig. 3.20, the bandwidth of the blue color (used for seeding the main amplifier) decreases as the preamplifier fiber length increases to 9.5 m. The gain narrowing on the blue color is because of the steep gain profile of the YDFA at the blue color side. From this figure, the pronounced gain narrowing on the blue color becomes problematic by increasing the preamplifier imposing a limitation on the pulse compression. For this reason, increasing the preamplifier length from 5.5 m to 9.5 m in order to maximize P_1P_2 from the main amplifier is at the expense of decreasing the spectral bandwidth of

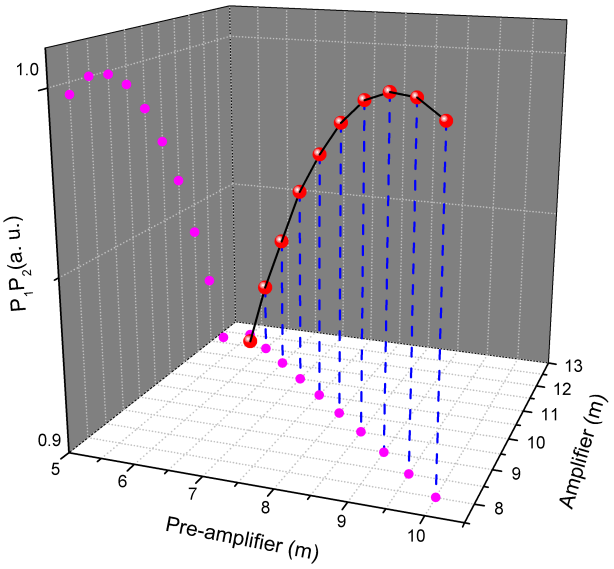

Figure 3.24: A 3D view of the variation of P_1P_2 from the main amplifier as a function of preamplifier fiber length and main amplifier fiber length. (Published in Ref. [96].)

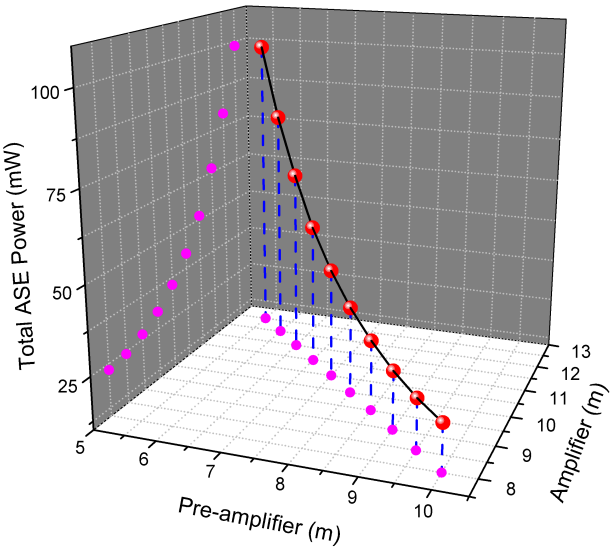

Figure 3.25: A 3D view of the variation of total ASE power corresponding to the optimized P_1P_2 as a function of preamplifier fiber length and main amplifier fiber length.

the blue color. From Fig. 3.24, in the midway, we find the 7.5-m-long preamplifier fiber a good compromise between maximum power and maximum bandwidth of the blue color. From this figure, the optimized fiber length of the main amplifier corresponding to the 7.5-m-long preamplifier is 10.5 m.

Fig. 3.25 illustrates the total ASE power generated from the main amplifier corresponding to the optimized P_1P_2. The corresponding ASE from the main amplifier decreases as the preamplifier fiber length increases because of the increased two-color seed power to the main amplifier and also decreased main amplifier fiber length. From this figure, the total ASE power decreases by 75% after increasing the preamplifier fiber length from 5.5 m to 9.5 m. The total ASE power including forward- and backward-traveling ASE is 42 mW from the 10.5-m-long main amplifier fiber.

3.5 conclusion

In summary, the modeling was successful to find the optimum fiber length of the two-color YDFAs in order to achieve two-color laser pulses with 1- a wavelength separation more than 70 nm, 2- a combined average power of more than 2.7 W optimized for the MIR generation, and 3) a sufficient bandwidth at each color for the subpicosecond durations.

I employed the LabVIEW simulation program that developed in this thesis for modeling of the amplification of two-color spectra in the wavelength range 1020-1120 nm in a two-stage YDFA system consisting of a single-clad single-mode Yb:fiber as of preamplifier and a double-clad single-mode Yb:fiber as of main amplifier. In the first step, the modeling results were justified with the measured output from previous low-power preamplifiers with the fiber lengths of 2.0 m and 2.7 m pumped with 150-mW laser diodes from both ends and seeded with a 3-mW two-color spectrum. Comparing the modeling and experimental results, the simulation was successful in order to predict the amplified two-color spectra and the total output average power of 23 mW. Also, an agreement was achieved on the simulation results to the optimum preamplifier fiber length between seeding with an experimental two-color seed spectrum and with a flat-top two-color seed spectrum. At this stage, the optimum fiber length was defined to have equal powers in the amplified colors.

In the experimental setup, the 23-mW output power of the two-color spectrum is reduced to 6 mW after passing through a notch filter and a Faraday isolator. The reduced two-color power is less than the seed saturation power of the main amplifier by one order of magnitude resulting to the generation of tremendous amount of ASE power after the main amplifier. For this, the LabVIEW simulation was used to model a more powerful preamplifier and a suitable length of the main amplifier.

In the modeling and based on experimental constraints, the preamplifier was co-pumped by 350-mW and counter-pumped by 500-mW from 986-nm single-mode laser diodes and the main amplifier was counter-pumped by a 6-W, 975-nm, multi-mode laser diode (from experiment, increasing the pump power in the preamplifier resulted in the ASE lasing spikes). In the simulation, an experimental 2.5-mW two-color spectrum was used. The short-wavelength color extended from 1030 nm to 1047 nm (peaked at 1043 nm) and the long-wavelength color extended from 1100 nm to 1120 nm (peaked at 1106 nm). Comparing the modeling and experimental results, the simulation was successful in order to predict the amplified two-color spectra and the total output average power of 200 mW after an optimized preamplifier fiber length. From modeling, the optimized preamplifier is 7.5 m long and delivers equal average powers on the output pulses. In the modeling, the main amplifier is seeded with 23 mW. The reduced seed power is because of using two notch filters and one Faraday isolator between the preamplifier and main amplifier in the experimental setup. From modeling results, the main amplifier fiber length is optimized at 10.5 m resulting to a good compromise between maximum power and maximum bandwidth of the blue color. This optimized two-color YDFA will find applications in the generation of short-pulse mid-infrared radiation. From modeling, the combined average power on the amplified two-color spectrum is 2.7 W. This result is confirmed by the result obtained from measurements.

Chapter 4

Tunable two-color ultrafast Yb:fiber CPA and mid-infrared generation

This chapter is based on the following publication:

M. Hajialamdari and D. Strickland. Tunable mid-infrared source from an ultrafast two-color Yb:fiber chirped-pulse amplifier. *Opt. Lett.*, **37**, 3570, 2012.

4.1 Tunable two-color Yb:fiber chirped pulse amplifier

In this thesis, I dealt with a two-color, ultrafast Yb:fiber chirped pulse amplifier as well as the generation of ultrashort MIR radiations by difference frequency mixing of the two-color pulses.

Fiber amplifiers have a unique characteristic of mode confinement in the high power regime which is hard to achieve from bulk laser gain media. The mode confinement is a result of the fiber design and the high power is a result of the distributed gain over a large fiber length. In recent years, ytterbium doped fiber amplifier systems have been increasingly used to amplify high-repetition-rate short laser pulses [22] because of their favorable properties such as high average output power, broad gain bandwidth, low cost, and compact size. Two-color short-pulse YDFA systems have been developed to amplify simultaneously two synchronized pulsed-laser beams of two different wavelengths [38–40]. The simultaneous amplification of the two colors in the same YDFA is advantageous. When

amplified in separate amplifiers, the two-color laser pulses acquire random phases due to fluctuations of the optical path imposed by the fluctuations of the ambient temperature and mechanical stress on the fiber. This becomes problematic for the DFG-based MIR generation where the two colors must have a stable phase difference. Thanks to the two-color YDFA system for reducing this noise.

In this thesis, I improved the two-color Yb:fiber chirped pulse amplifier system of Ref. [39] step by step, in order to suppress the ASE between the two colors and achieve a better-balanced two-color spectrum with a watt-level average power. From the improved system, I achieved more than 2.7 W average power at the two colors with a significantly reduced ASE power after the main amplifier whereas the two colors were separated spectrally as wide as 71 nm. In the first step, the two-color single-clad Yb:fiber in the preamplifier stage was improved using the modeling results. The improved two-color preamplifier resulted in an increased average power of $\sim$ 200 mW which was an improvement by one order of magnitude, distributed equally on the two colors centered at 1038:1103 nm. In the second step, the two-color Yb:fiber in the main amplifier stage was improved by replacing the non polarization maintaining double-clad Yb:fiber with a polarization maintaining type. Therefore, it became possible to adjust the polarization of the output two-color pulses from the main amplifier with a s-polarized transmission grating pulse compressor. Together with its longer length that was already determined by modeling, the new PM double-clad Yb:fiber amplifier resulted in two-color ultrashort pulses with an increased average power of 2.7 W after the amplification stage and a total average power of $\sim$ 1.5 W after the two-color pulse compressor with a better-balanced two-color spectrum which was an improvement by a factor of five. The tunable two-color ultrafast pulses was used for the generation of tunable ultrashort MIR pulses using DFG technique in a GaSe crystal.

Before the improvements, this system was not widely tunable because the seed power was not sufficient to overcome the ASE at the gain peak in the YDFA for a wide color separation. The tuning range of the MIR is limited on the long wavelength side by absorption in the NLO crystal. For GaSe, this limit is $\sim$ 20 μm. On the short wavelength side, it is limited by either the phase-matching bandwidth of the NLO crystal or, in this system, the maximum separation of the two colors. The YDFA system when pumped at 980 nm, has a gain profile in the wavelengths $\sim 1020 - 1120$ nm with a gain maximum between 1030 nm and 1100 nm depending on the fiber length. In our two-color YDFA system, the gain maximum is around $\sim$ 1070 nm. In the improved two-color YDFA system, the maximum separation of the two colors was limited by 71 nm because the average power of the two-color pulses before the preamplifier was insufficient to suppress the ASE. For the low average-power seed pulses with more than 71-nm wavelength separation, the ASE at the gain peak took over the stored energy in the Yb:fiber amplifiers resulting in detrimental

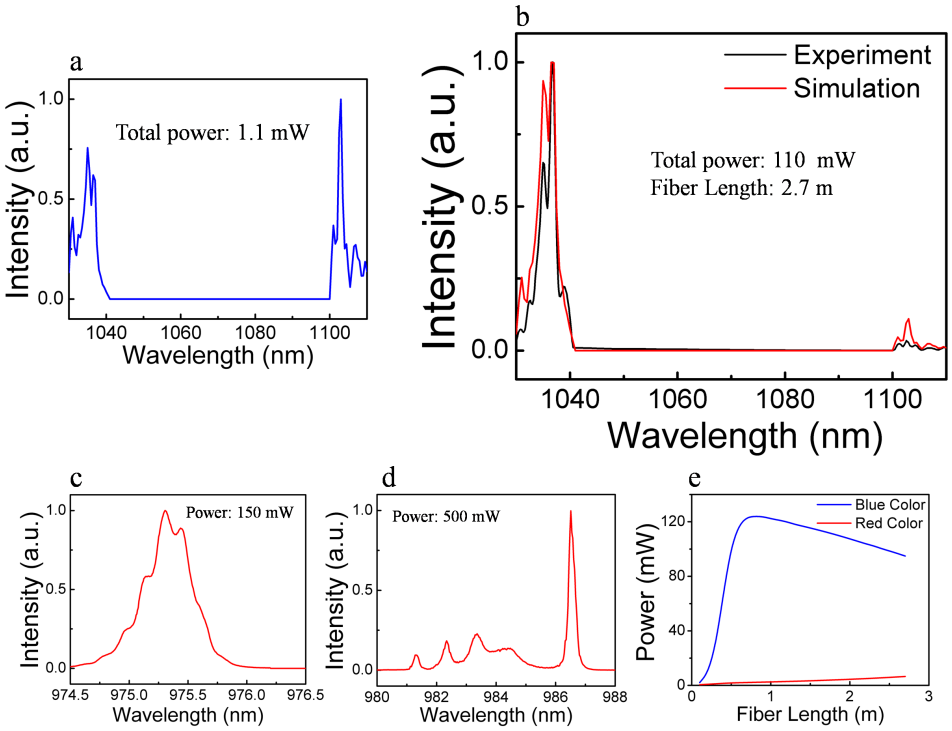

Figure 4.1: (a) Measured spectrum of a 1.1-mW two-color seed input to the preamplifier, (b) measured spectrum (black line) and modeled spectrum (red line) after the 2.7-m-long preamplifier fiber seeded with the two-color spectrum of the panel (a), (c) measured spectrum of the 150-mW laser diode, (d) measured spectrum of the 500-mW laser diode, and (e) simulation results to the variations of the average power of each color as a function of fiber length. The modeling has been performed with the experimental two-color seed spectrum and power spectra of the pump lasers shown in the panels (a), (c), and (d). The pump coupling efficiency is 40%.

lasing spikes at high pump powers.

In order to investigate the performance of the system of Ref. [39], I replaced one of the pump lasers and the focusing lenses to the fiber core. A coupling efficiency of 40% was achieved for launching pump power into the fibers after replacing the focusing lenses. Fig. 4.1(b) depicts the measured spectrum (black line) from the 2.7-m-long preamplifier fiber after replacing the 150-mW 975-nm laser diode in the counter-pumping position by a 500-mW 986-nm laser diode. The fiber was co-pumped by a 150-mW 975-nm laser diode as was in Ref. [39]. In this figure, the spectrum shown with the red line depicts the modeled

preamplified spectrum. Figs. 4.1(a), (c), (d), and (e) illustrate, respectively, measured spectrum of a 1.1-mW two-color seed input to the preamplifier, measured spectrum of the 150-mW laser diode, measured spectrum of the 500-mW laser diode, and simulation results of variations of the average power of each color as a function of fiber length. The measured preamplified two-color spectrum had a 110-mW total average power and the modeled two-color spectrum has a 102-mW total average power. From Fig. 4.1(b), the 110-mW average power is not distributed equally between the two colors. From Fig. 4.1(e), the simulation shows an average power of 95 mW in the blue color and an average power of 7 mW in the red color. Also from this figure, it is obvious that the two colors would have been amplified to the same power level if the amplifier length were increased above the 2.7 m. This was discussed in detail in Chapter 3 and I showed (from both experimental and modeling results) that the preamplifier fiber length is ideally 7.5 m for the case that was pumped from both ends by the 500-mW laser diodes.

Using the output from the preamplifier discussed above, Fig. 4.2(a) shows the measured preamplified two-color spectrum after passing through a 1055-nm notch filter with a 55-nm rejection bandwidth for removing the ASE and then passing through a Faraday isolator. The seed spectrum had a total average power of 34 mW just before the main amplifier. Fig. 4.2(b) shows the measured (black line) and modeled (red line) two-color spectrum from the main amplifier fiber seeded with the 34-mW two-color spectrum. The main amplifier was a 9-m-long non-polarization maintaining double-double Yb:fiber counter-pumped by a 5-W 975-nm laser diode as in Ref. [39]. Figs. 4.2(c), (d), and (e) illustrate, respectively, measured spectrum of the 5-W laser diode, simulation results to the variations of the average power of each color and the (forward + backward traveling) ASE as a function of fiber length, and the simulation results to the product of the power of the two colors as a function of fiber length. The measured two-color spectrum after the main amplifier had a 2.3-W total average power. The modeled two-color spectrum has a total average power of 2.235 W distributed as of 1830 mW in the blue color, 290 mW in the red color, and 115 mW in the ASE spectrum (from panel (d)). From Fig. 4.2(b), the 2.3-W average power is not distributed equally between the two colors. From Fig. 4.2(e), the product of the power of the two colors is maximized from an 11-m amplifier length where the total average power decreases to 1.75 W distributed through 1060 mW in the blue color, 690 mW in the red color and 350 mW in the ASE spectrum.

In Section 3.3.2, from simulation and experimental results, an average power of 200 mW distributed equally on the two colors was obtained from the improved 7.5-m-long preamplifier pumped from both ends by 500-mW 986-nm laser diodes. Also, in Section 3.4 from simulation results, an average power of 2.7 W distributed through 1.44 W in the blue color and 1.23 W in the red color was obtained from the improved 10.5-m-long polarization

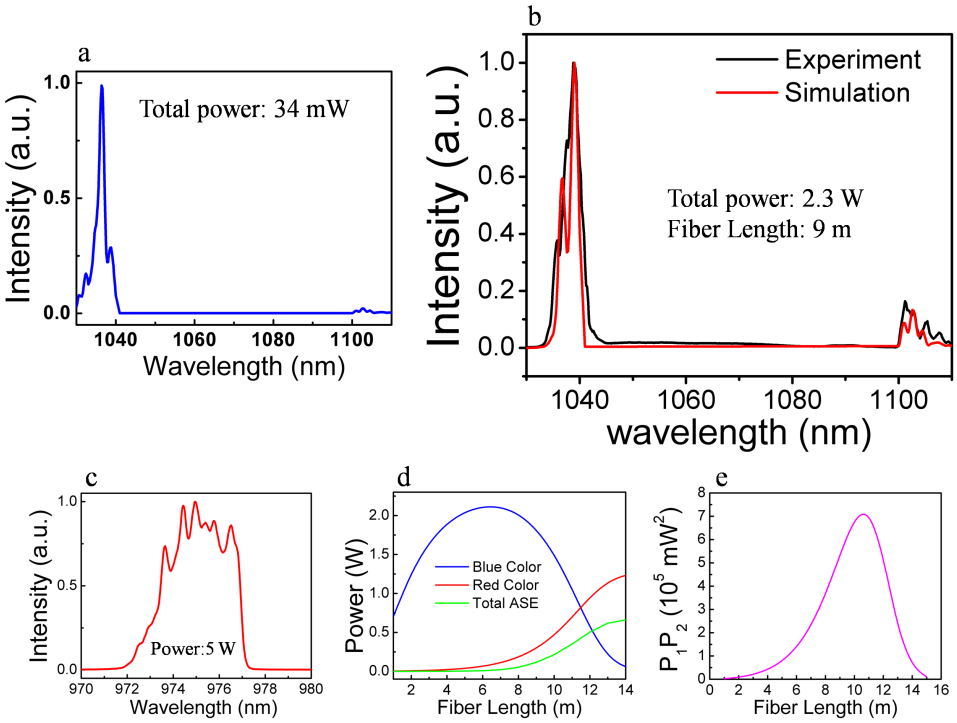

Figure 4.2: (a) Measured spectrum of a 34-mW two-color seed before the main amplifier, (b) measured spectrum (black line) and modeled spectrum (red line) after the 9-m-long main amplifier fiber seeded with the two-color spectrum of the panel (a), (c) measured spectrum of the 5-W laser diode, (d) simulation results to the variations of the average power of each color and (forward + backward traveling) ASE as a function of fiber length, and (e) simulation results to the product of the power of the two colors as a function of fiber length. The modeling has been performed with the experimental two-color seed spectrum and power spectra of the pump lasers shown in the panels (a) and (c). The pump coupling efficiency is 50%.

maintaining amplifier counter-pumped by a 6-W 975-nm laser diode. From experimental results, a total average power of more than 2.7 W was measured from the improved main amplifier. The output of the improved amplifier after the pulse compressor is presented in Figs. 4.8 and 4.9 in relate to the measured MIR spectra.

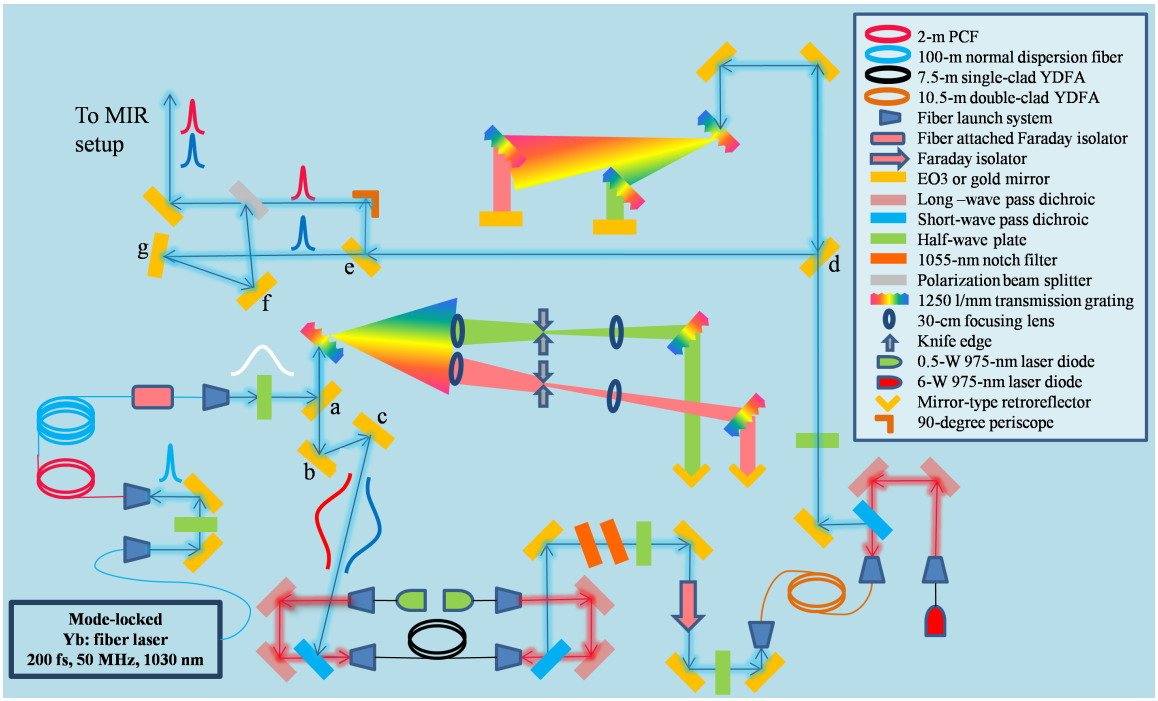

Figure 4.3: Top-view layout of the experimental setup of the tunable two-color ultrafast Yb:fiber chirped pulse amplifier. The rainbow mimics the infrared continuum in the wavelengths 950-1150 nm. In the two-color pulse compressor setup, the spectrum between the two colors is an indication of the ASE spectrum.

4.2 Experimental setup of the tunable two-color ultrafast Yb:fiber chirped pulse amplifier

In this thesis, for the generation of tunable two-color ultrafast laser pulses, I used the experimental setup from Ref. [39] and improved the preamplifier and amplifier stages.

Fig. 4.3 illustrates the top-view layout of the experimental setup of the tunable two-color ultrafast Yb:fiber chirped pulse amplifier. To generate a continuum, the output pulses from a polarized 200-fs, 50-MHz, 1030-nm Yb:fiber laser are launched into a 2-m-long single-mode 1040-nm-zero-dispersion photonic crystal fiber after passing through a $\lambda/2$ plate. In the launching system, two 10× microscope objective lenses are used and the coupling efficiency is estimated 50%. To stretch the pulses, the PCF is fiber spliced to a 100-m-long normal dispersion fiber. In the normal dispersion fiber, the laser pulses acquire a positive chirp, that is the high-frequency components of the pulses travel slower

than the low-frequency components. Using the refractive index of the pure fused silica, the up-chirped laser pulses have a pulsewidth of 25 ps at the wavelength 1041 nm and 19 ps at the wavelength 1103 nm after the fiber stretcher.

The output of the dispersion fiber is spliced to a fiber-attached Faraday isolator to protect the Yb:fiber oscillator from backward traveling radiations. After the Faraday isolator, the continuum is collimated by an AR-coated 11-mm focal length aspheric lens and then it passes through another $\lambda/2$ plate for rotating its polarization in order to maximize the throughput from the free space optics. The normal dispersion fiber partially preserves the polarization of the continuum due to the fiber birefringence. The fiber birefringence arises from the inherent mechanical stress in the fiber and from the coiled fiber. After the fiber-attached Faraday isolator, the continuum extends from 950 nm to 1150 nm with an average power of 27 mW. The spectrum of the continuum showed variations with the input polarization of the pulses into the PCF. The variations were dramatic at the short-wavelength side of the continuum.

Next, the continuum is sent toward a two-color pulse stretcher after reflecting off the mirror (a). The two-color pulse stretcher comprises of three 1250 l/mm polarization transmission gratings (Ibsen photonics, FSTG-PCG-1250-1064), four 30-cm focal-length 2.5-cm-diameter focusing lenses forming two telescopes, four movable knife edges placed at the focal plane of the telescopes, and two mirror-type retroreflectors. The purpose of using the two-color pulse stretcher is twofold: stretching the pulses and slicing the continuum into two colors. The grating size is 20 mm $\times$ 10 mm. The 20-mm grating width was not enough if one would try to build the stretcher out of the two gratings for an 80-nm spectral separation between the two colors.

After the mirror (a), the continuum is reflected toward the first grating of the two-color pulse stretcher. The beam hits the first grating close to its lower side. From datasheet, the transmission spectrum of the gratings shows more than 90% transmission for the wavelengths 1000-1100 nm for the TE polarization at the Littrow angle. The Littrow angle is 41.7 degrees at the wavelength 1064 nm. From this, the angle between the normal line to the first grating and the incident beam is set roughly 42 degrees. After the first grating, the refracted continuum travels toward the two lenses placed at a distance 23 cm from the first grating. From the grating's datasheet, the divergence angle of the spectrum is roughly 0.1 degrees/nm at the wavelength 1064 nm. At the 23-cm distance a spectral bandwidth of $\sim$ 60 nm passed through each lens for each of the short-wavelength and long-wavelength colors. Now, the continuum is divided into two colors traveling to the four knife edges. Four movable knife edges placed at the focal plane of the telescope act like two perfect notch filters. The central wavelength and bandwidth of each color are set by moving the four knife edges. The distance between the two knife edges is adjusted a few millimeters

to have a bandwidth of roughly 10 nm at each color passes through the knife edges. This bandwidth is enough for the Fourier transform limited 200-fs pulses at the wavelengths 1041 nm and 1103 nm. After passing through the two last lenses, the two colors travel toward the two last gratings. The two last gratings have a perpendicular orientation to the first grating. The distance between the second lens and the second grating for the 1041-nm color was set at 45 mm and that for the 1103-nm color was set at 182 mm. From calculations by using the cited distances, the pulsewidth of the two-color seed after the pulse stretcher was increased by 47 ps for the 1041-nm pulses and by 39 ps for the 1103-nm pulses from the grating pulse stretcher. After reflecting from the retroreflectors made up of perpendicular mirrors, the two colors travel back to the first grating. The retroreflector mirrors are adjusted to have the reflected beam above the incident beam on the first grating in order to pass above the mirror (a).

The two-color beam has to be collimated for the best coupling efficiency to the preamplifier fiber. For this, the beam size was measured in the near field and far field locations and corrections were made by adjusting the collimating lens after the fiber-attached Faraday isolator and slightly changing the positions of the second lenses in the stretcher. Also, the two-color beam has to be free of spatial chirp. For a beam with a spatial chirp, the distribution of the frequency components of the pulse is not uniform but is dispersed across the beam spot. This becomes problematic for uniformly focusing all the frequency components of the two-color beam into the fiber core of the preamplifier fiber. The spatial chirp on the two-color beam was tested by focusing the beam into a fiber-attached spectrometer. By tweaking the beam to the left and right of the focusing lens of the connected fiber to the spectrometer, the spectrum was tested in order to observe a uniformly decreasing amplitude. The spatial chirp was removed from both of the short-wavelength color and the long-wavelength color by slightly rotating the two last gratings in the two-color pulse stretcher.

The two color seed spectrum had, typically, an average power of 2.5 mW after the pulse stretcher as was shown in Fig. 3.14(a). By rotating the two first $\lambda/2$ waveplates, the total average power and the power ratio between the two colors of the seed spectrum could be changed.

Next, the stretched two-color pulses were directed toward the preamplifier by mirrors (b) and (c). Now, the preamplifier is a 7.5-m-long single-mode single-clad Yb:fiber pumped from both ends by 500-mW, 986-nm single-mode laser diodes. In order to prevent feedback of the signals into the fiber cores, the preamplifier fiber was angle cleaved at 8 degrees from both ends. The laser diodes from each side were collimated by an 11-mm focal length AR-coated aspheric lens. In the input side, the seed signal and laser diode were focused into the preamplifier fiber by a 6-mm focal length AR-coated aspheric lens for a tight focusing

of the seed into the fiber core. In the output side, an 11-mm focal length AR-coated aspheric lens was used. Two dichroic mirrors of the same type were used for the input seed signal and output amplified signal in the preamplifier setup. From measurements, the seed dichroic mirror had more than 98% reflection at the wavelength 1035 nm, 80% reflection at the wavelength 1105 nm and 80% transmission at the wavelength 975 nm at the angle 35 degrees. The seed dichroic mirror had an optimum working condition at the angle 35 degrees. Two dichroic mirrors from each side were used for aiming each laser diode into the fiber core. From measurements, the pump dichroic mirrors had more than 98% reflection at 975 nm and 80% transmission for the wavelengths 1035-1105 nm at the angle 45 degrees. The core diameter of the preamplifier fiber is 4 μm with a core numerical aperture of 0.2. The estimated coupling efficiency of the laser diodes into the preamplifier fiber is roughly 50%. The nominal average power in the two colors after the preamplifier was 200 mW as was shown in Fig. 3.14(b) for a co-pump power of 350 mW and a counter-pump power of 500 mW. Detrimental lasing spikes appeared at a co-pump power of 500 mW.

After the preamplifier, two holographic notch filters were used in series to remove the ASE spectrum between the two colors. The central wavelength and rejection bandwidth of the two notch filters are, respectively, 1065 nm and 45 nm for a normal incident beam. However, these could be changed by varying the incident angle. Ideally, we needed a tunable rejection bandwidth of between 57 nm and 71 nm for the MIR generation between 20 and 16 μm. By tuning the incident angles of the two notch filters, a tunable rejection bandwidth of between 48 and 55 nm centered at 1073 nm was achieved. From measurements, each notch filter had a 50% transmission for the wavelengths 1035-1110 nm. Next, the beam passed though a Faraday isolator to block the radiations from the main amplifier back to the preamplifier. A $\lambda/2$ waveplate was used before the Faraday isolator to rotate the polarization into the p-state. A maximum transmission of 50% was achieved. The Faraday isolator has a 90% transmission for a perfectly polarized light. However, after the non-polarization maintaining preamplifier, the two-color pulses are partially polarized.

Next, the preamplified two-color pulses were injected into the main amplifier. Now, the main amplifier is a 10.5-m-long polarization-maintaining single-mode double-clad Yb:fiber counter-pumped by a 6-W, 975-nm multi-mode laser diode. In order to prevent feedback of the signals into the fiber cores, the amplifier fiber was angle cleaved at 8 degrees from both ends. The laser diode was collimated by an 11-mm focal length AR-coated aspheric lens then it was focused into the inner cladding of the fiber by the same lens type. In the input side, the seed signal was focused into the fiber core by a 6-mm focal length AR-coated aspheric lens for a tight focusing. In the output side, the dichroic mirrors are the same as that explained for the preamplifier. In the input side, there is no dichroic mirror but just EO3 mirrors. The core diameter of the main amplifier fiber is roughly 6 μm with a

core numerical aperture of 0.14. The numerical aperture of the inner cladding is 0.46. The estimated coupling efficiency of the pump power into the inner cladding is roughly 60%. The waveplate before the main amplifier was used to rotate the polarization of the input two-color pulses with one of the slow or fast axes of the PM Yb:fiber amplifier. For this, the output power after the amplifier was maximized by rotating the waveplate by the fact that the reflection coefficient of the output dichroic mirror is polarization dependent. A typical average power more than 2.7 W was achieved after the main amplifier. The ratio of the average power of the two colors could be changed by rotating the first two waveplates in the system.

Next, the amplified two-color pulses were sent toward the two-color pulse compressor after passing through a $\lambda/2$ waveplate and from above the mirror (d). The waveplate was used to maximize the throughput of the pulse compressor for the TE-polarized transmission gratings. The two-color pulse compressor comprises of the same three gratings used in the pulse stretcher. The first grating is oriented at the 42-degree Littrow angle. The incident beam hits the first grating close to its upper side. The two-color spectrum are refracted toward the other two gratings, one for the 1041-nm pulses and another one for the 1103-nm pulses. The first grating is parallel with the other gratings. After reflecting from the regular EO3 mirrors in the compressor arms, the two colors travel back to the first grating. The mirrors are adjusted so that on the first grating from top to bottom, the incident beam, the compressed 1041-nm pulses, and the compressed 1103-nm pulses are located in a column. Again, the compressed two-color pulses are refracted back from the first grating to the mirror (d). Now, the two-color beams turn around toward the setup of the polarization beam splitter. With the 1041-nm color on top of the 1103-nm color, the 1041-nm color passes above the mirror (e) and turns around in a triangle path by the mirrors (f) and (g) toward the polarization beam splitter and then is reflected to the left by the PBS. The 1103-nm color is reflected by the mirror (e) toward a 90-degree periscope. After the periscope, the polarization of the 1103-nm color is rotated by 90 degrees and the beam passes through the PBS. The PBS is oriented at the Brewster angle for the 1103-nm color. The two colors are s-polarized after the two-color pulse compressor and now the 1103-nm color is p-polarized. The two color pulses were temporally overlapped by moving the back mirror in the 1041-nm pulse compressor. A typical average power of 1400 mW for the 1041-nm pulses and 100 mW for the 1103-nm pulses was achieved after the PBS. In the pulse compressor, the distance between the first grating and the second grating for the 1041-nm pulses was optimized at 134 mm and that for the 1103-nm pulses was optimized at 310 mm

4.2.1 Pulse stretching, pulse compression, and excess negative GDD on the 1041-nm pulses in the two-color Yb:fiber CPA

In the two-color grating pulse stretcher, the incident angle is at the Littrow angle 42 degrees, the diffracted angle θ_d is 39.2 degrees at the wavelength 1041 nm and is 45.2 degrees at the wavelength 1103 nm for the grating period of 1250 l/mm. Using the values from the experimental setup: $f = 30.0$ cm, $s_1 = 22.9$ cm for the distance between the first grating and the first lenses, $s_2 = 4.5$ cm for the distance between the second grating and final lens for the 1041-nm pulses, $s_2 = 18.2$ cm for the distance between the second grating and the final lens for the 1103-nm pulses, and $d = 1250$ l/mm in Eq. 2.16, the GDD is 3.384 ps^2 at the wavelength 1041 nm and is 2.823 ps^2 at the wavelength 1103 nm after the two-color grating pulse stretcher. The GDD is positive from the pulse stretcher indicating a positive chirp is imposed on the stretched pulses. Using Eq. 2.11, from the grating pulse stretcher, the pulse broadening $\Delta\tau$ is 47 ps for the 1041-nm pulses with a 8-nm spectral bandwidth and is 39 ps for the 1103-nm pulses with a 9-nm spectral bandwidth.

Ideally from the stretcher equation 2.16, as s_1 and s_2 decrease the GDD increases resulting in a more pulse broadening. Thus, with a reduced pulse peak power, amplification of the laser pulses in the YDFAs can be performed more safely. However, in the experimental setup there were physical limitations with decreasing the s_1 and s_2 distances. For the s_1 distance, the first grating was at the closest distance to the first lenses such that the two colors centered roughly at 1035 nm and 1105 nm passed through each lens individually while the two lenses were side by side at a closest distance. For the s_2 distance of the short-wavelength pulses, it was at the minimum distance because the physical dimension of optical holders of the grating and the second lens did not allow us to bring them closer. The s_2 distance of the long-wavelength pulses was more than that of the short-wavelength pulses because of limited space in the pulse compressor. With the s_2 decreases the compressor length increases.

To further stretch the pulses, a fiber stretcher in the normal dispersion regime was added to the system before the grating pulse stretcher. The pulse broadening and GDD from the fiber are calculated as follows. From Eq. 2.13, the dispersion coefficient can be readily calculated for the fibers by knowing the refractive index. The main material of the fibers used in this thesis is silica and we assume that the refractive index of the fiber stretcher and Yb:fibers can be described by the refractive index of fused silica which is described by an empirical equation [84]

$$n = 1.4508554 - 0.0031268\,\lambda^2 - 0.0000381\,\lambda^4 + \frac{0.0030270}{\lambda^2 - 0.035} - \frac{0.0000779}{(\lambda^2 - 0.035)^2} + \frac{0.0000018}{(\lambda^2 - 0.035)^3}. \quad (4.1)$$

From Eqs. 2.13 and 4.1, the dispersion coefficient D is -31.976 ps/nm-km at 1041 nm and is -21.385 ps/nm-km at 1103 nm. Substituting these D values in Eq. 2.12, for the Fourier transform Gaussian pulses with a 200-fs pulsewidth, the pulse broadening after a 100-m-long fiber is 25 ps for the 1041-nm pulse and is 19 ps for the 1103-nm pulses (Using Eq. 2.8 and $\Delta\lambda = \lambda^2\Delta\nu/c$, the spectral bandwidth in terms of wavelength of the 200-fs pulses is 8 nm for the 1041-nm pulses and is 9 nm for the 1103-nm pulses). Thus, the total pulse broadening from the fiber stretcher and grating stretcher before sending the pulses into the preamplifier Yb:fiber is 72 ps for the 1041-nm pulses and is 58 ps for the 1103-nm pulses.

Now we obtain the total GDD in the system before compressing the pulses. From Eq. 2.15 and the calculated D values, the GDD for the 100-m fiber stretcher is 1.838 ps^2 for the 1041-nm pulses and is 1.380 ps^2 for the 1103-nm pulses. The GDD values are positive numbers indicating a positive chirp from normal dispersion fibers. In the two-color Yb:fiber CPA system, the fiber length of the preamplifier was 7.5 m and the fiber length of the main amplifier was 10.5 m. This adds a dispersion length of 18 m to the 100-m fiber stretcher. Thus, the total GDD for the total 118-m fiber length is 2.169 ps^2 for the 1041-nm pulses and is 1.629 ps^2 for the 1103-nm pulses. From these calculations, the total positive GDD in the system including fiber stretcher, grating pulse stretcher, and Yb:fibers is 5.553 ps^2 for the 1041-nm pulses and is 4.452 ps^2 for the 1103-nm pulses. The total GDD values will be used later to find the difference between the total positive GDD and the total negative GDD in the system.

For the pulse compressor, from Eq. 2.17 and with the incident angle at the Littrow angle $\theta_i = 42$ degrees, the GDD is -1.796 ps^2 for the compressor length $L = 134$ mm at the wavelength 1041 nm and is -6.572 ps^2 for the compressor length $L = 310$ mm at the wavelength 1103 nm. From measurements, a 500-fs pulsewidth was achieved on both colors after optimizing the pulse compressor lengths mentioned above. The GDD in the pulse compressor is negative indicating a negative chirp imposed on the pulses.

Comparing the total positive GDD and the negative GDD values, there are an extra negative GDD (-3.757 ps^2) on the 1041-nm pulses and an extra positive GDD (2.12 ps^2) on the 1103-nm pulses before the pulse compressor. The negative GDD for the 1041-nm pulses can partly be explained by the gain narrowing effect in the Yb:fiber amplifiers. The gain spectrum of the Yb:fibers is sharp on the short wavelength side around the wavelength 1040 nm resulting in the gain narrowing at these wavelengths. With the narrowed bandwidth 1041-nm pulses, one needs to impose less amount of GDD for compressing the pulses to the Fourier transform limit at the expense of an increased pulsewidth. From experimental

results, the bandwidth of the 1041-nm pulses decreases approximately by a factor of 1/2 after amplification. Therefore, for a positive GDD of 5.553 ps^2, a negative GDD of 2.777 ps^2 is sufficient for compressing the pulses to the Fourier transform limit. Now, the pulsewidth of the narrowed bandwidth 1041-nm pulses after compression should be around 400-fs. From experiment, the pulsewidth of the 1041-nm pulses was around 500 fs. However, considering the gain narrowing, there is still a negative 1-ps^2 GDD in the system for the 1041-nm pulses before the pulse compressor. This may be related to an absorption-induced refractive index change of the doped silica fiber. In fact, from the strong reabsorption process for the wavelengths close to 1035 nm, the average power of the 1041-nm pulses in both preamplifier and amplifier Yb:fibers decreases abruptly as the pulses propagate in the long fibers (see Figs. 3.15 and 3.22). For this, obtaining the refractive index of the Yb:fibers by the use of Kramers-kronig analysis in the operation regime with pump-probe experiments may elucidate the problem.

Finally, the negative GDD on the 1041-nm pulses cannot be explained by the third order dispersion in the fibers. To obtain the third order dispersion, the GDD is expanded in a Taylor's series up to the first order

$$\mathrm{GDD} = \mathrm{GDD}\Big|_{\omega_0} + \frac{d\,\mathrm{GDD}}{d\omega}\Big|_{\omega_0} \Delta\omega \tag{4.2}$$

where the second term describes the third order dispersion. From numerical calculations, the third order dispersion from the 118-m fiber has a contribution to the GDD by an amount of -0.0690 ps^2 for the 8-nm bandwidth 1041-nm pulses and -0.0795 ps^2 for the 9-nm bandwidth 1103-nm pulses.

4.2.2 The B-integral parameter in the Yb:fiber amplifiers

In the two-color Yb:fiber CPA, ultrashort two-color pulses were temporally stretched before passing through Yb:fiber amplifiers. This is because ultrashort laser pulses have a large peak intensity in the fiber core that nonlinear phenomena such as self phase modulation become so important [31]. The peak intensity of the 200-fs, 50-MHz, laser pulses with a 100-mW average power is 80 GW/cm^2 in the preamplifier output with a 4-μm core diameter. The peak intensity increases to 350 GW/cm^2 for the amplified pulses with an average power of 1 W in the main amplifier output with a 6-μm core diameter. For such high intensity laser pulses, the refractive index changes by [61]

$$n = n_0 + n_2\, I(t) \tag{4.3}$$

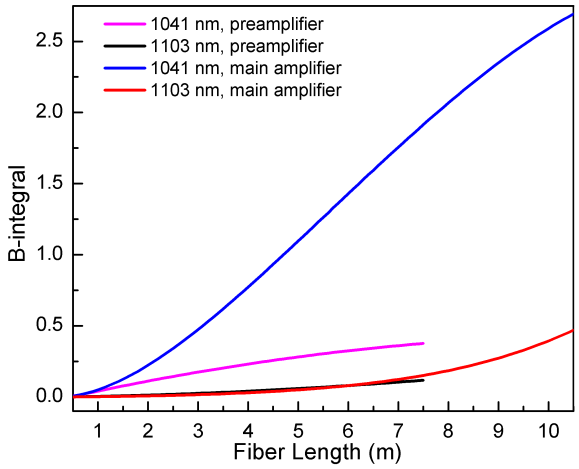

Figure 4.4: The variations of the cumulated B-integral parameter as a function of fiber length in the preamplifier and main amplifier Yb:fibers. The variations of the average power of the two colors as a function of fiber length are those illustrated in Fig. 3.15 for the preamplifier and in Fig. 3.22 for the main amplifier.

where n_0 is the zero-filed refractive index, n_2 is the nonlinear refractive index coefficient, and I is the time-dependent intensity of the laser pulses. Now, the refractive index of the fiber becomes self modulated with the pulse intensity resulting in a nonlinear phase function (for example, for the Gaussian pulses the phase function becomes self modulated with the Gaussian function).

With the nonlinear phase function, there is a nonlinear frequency shift along the ultrashort amplified laser pulses in the Yb:fiber amplifier. Such laser pulses are broadened in a nonlinear fashion that makes it difficult to be recompressed to the initial pulsewidth by the regular pulse compression techniques so that part of the pulse energy remains in the pulse wings which is not much useful. For the SPM, the extent of nonlinearity is calculated from a parameter called B-integral parameter [91]

$$B = \frac{2\pi}{\lambda} \int n_2 \, I \, dz. \tag{4.4}$$

In order to have the laser pulses not much affected by the SPM effect, the cumulated B-integral parameter should be < 1 [91]. This is achieved by stretching the laser pulses to the extent that the propagating laser pulses in the Yb:fiber amplifiers satisfy the cited criteria.

Fig. 4.4 shows the results of calculations on the variations of the cumulated B-parameter as a function of fiber length on the blue and red color pulses with the respective central wavelengths of 1041 nm and 1103 nm in the two-color ultrafast Yb:fiber system, in the plane-wave approximation and by assuming the pulsewidth remains constant in the fibers. The pulsewidth of the two-color pulses is 1 nanosecond. These calculations have been performed for the simulated average powers of the two-color pulses in the preamplifier and main amplifier Yb:fibers illustrated, respectively, in Fig. 3.15 and Fig. 3.22. The nonlinear refractive index coefficient is assumed to be constant along the Yb:fibers with a value of 3.2×10^{-16} cm^2/W for the fused silica [61]. From this figure, for the 1-ns laser pulses the total B-integral parameter from the 7.5-m-long preamplifier and 10.5-long amplifier fibers is 3.1 radians for the 1041-nm pulses and is 0.6 radians for the 1103-nm pulses. From these crude calculations, with the 1041-nm pulses stretched to more than 3 ns pulses we obtain $B \leq 1$. As was described earlier, the blue-color pulses were stretched to a 72-ps pulsewidth and the red-color pulses were stretched to a 58-ps pulsewidth which are clearly lower than the nanosecond scale mentioned above. From these calculations, in order to increase the pulsewidths of the two-color pulses to the nanosecond scale, the compressor length should have been increased to more than 5 m which was beyond the available space in the experimental setup.

4.3 Experimental setup of the short-pulse MIR generation

For MIR generation, I used the experimental setup from Ref. [39]. Fig. 4.5 depicts the schematic of the experimental setup for the ultrafast mid-infrared generation and detection in this thesis. Synchronized s-polarized pump optical pulses (the short wavelength color or blue color) and p-polarized signal optical pulses (the long wavelength color or red color) were combined by a polarization beam splitter to travel as a single beam. The PBS is highly reflective for the s-polarization beam and is highly transmissive for the p-polarization beam. The combined beam was sent toward a periscope. After the periscope, the polarization of the beam is rotated by 90 degrees. Now, the pump beam is p-polarized and the signal beam is s-polarized. This is illustrated in Fig. 2.2. This orientation of the polarizations is necessary for the angle phase matching because GaSe is a negative uniaxial crystal so that its ordinary refractive index is larger than its extraordinary refractive index [63, 97]. Thus, the right-hand side of the phase matching equation 2.4 can take positive numbers for a range of angles as the crystal is rotated whereas at the critical phase matching angle it equals to the left hand-side of the equation. A 400-mm-focal-length focusing lens was

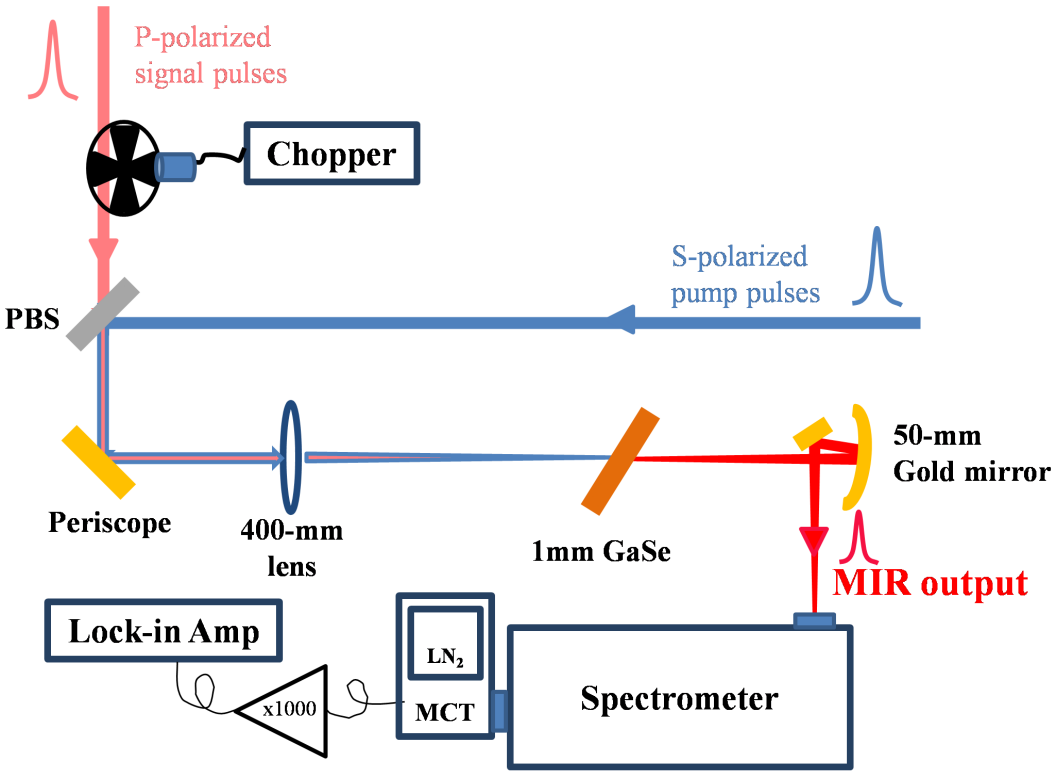

Figure 4.5: Schematic of the experimental setup for the ultrafast MIR generation and detection.

used to focus the combined beam into a 1-mm-thick GaSe crystal. The GaSe crystal was hold by a rotation stage by which the crystal could be rotated about its optic axis for the azimuthal angle ϕ and perpendicular to the principal plane for the phase matching angle θ. The azimuthal angle ϕ maximizes d_{eff} in Eq. 2.1 and is not important for the phase matching [63, 98]. The focused beam in GaSe crystal was 1:1 imaged by a 50-mm-focal-length spherical gold mirror placed at a ∼100-mm distance to the crystal with an angle near to normal incidence. After reflection from a flat gold mirror, the image was formed onto the entrance slit of a 50-grooves/mm monochromator for measuring the MIR spectra. At the exit of the monochromator, a 1-mm-thick germanium filter was used to filter out the pump and signal pulses and then the MIR radiation was detected by a liquid nitrogen cooled HgCdTe (MCT) detector. For the measurement of the average power of the MIR pulses, the detector with the filter at the place was placed exactly at the location of the entrance slit of the monochromator. The weak output of the HgCdTe was preamplified by

a battery-operated operational amplifier (op-amp) to a factor of 1000. A lock-in amplifier was used to measure the output of the op-amp to improve the signal to noise ratio. The lock-in amplifier was triggered by the chopping frequency from a $\sim$ 1-kHz chopper wheel. Only one of the pump or signal beams is chopped (here the red color). This ensured us that the lock-in amplifier only monitors the MIR output (when either pump or signal pulses were blocked, a zero average voltage obtained from the lock-in amplifier). From datasheet, the responsivity of the MCT+(op-amp) is maximum with a value of 152 mV/mW at the wavelength 22 μm and it drops by $\sim$ 50% to the value of 75 mV/mW at the wavelength 18.5 μm. Considering the $\sim$ 35% transmission coefficient of the germanium filter at the wavelength 18.5 μm, a conversion factor of 38 μW/mV is obtained at the wavelength 18.5 μm. This conversion factor has been decreased by a factor of four to a value of 9.3 μW/mV for ultrashort laser pulses at the wavelength 18.5 μm to compensate the voltage jump at the peak intensity of the ultrashort laser pulses. This conversion factor has given a reasonable agreement with the calculated average power of the 18.5-μm ultrashort MIR pulses.

4.4 Phase matching angles in GaSe crystal

From experiments, the incident phase matching angle θ_p for the pump pulses measured to the normal line (in air) was achieved at an angle roughly 35° for difference frequency mixing of the blue color and red color pulses centered at the wavelength 1041 nm and 1103 nm respectively. From calculations, this corresponds to the in-crystal phase matching angle $\theta = 12.0°$ for the type-I phase matching (eoo) and $\theta = 12.3°$ for the type-II phase matching (eoe). For the calculations, Eqs. 2.2, 2.4, and 2.5 are solved simultaneously. In the equations, the λ-dependent ordinary refractive index is calculated from [97]

$$n_o^2 = 7.443 + \frac{0.4050}{\lambda^2} + \frac{0.0186}{\lambda^4} + \frac{0.0061}{\lambda^6} + \frac{3.1485\lambda^2}{\lambda^2 - 2194}, \tag{4.5}$$

and the principle value of the λ-dependent extraordinary refractive index is calculated from [97]

$$n_e^2 = 5.760 + \frac{0.3879}{\lambda^2} - \frac{0.2288}{\lambda^4} + \frac{0.1223}{\lambda^6} + \frac{1.855\lambda^2}{\lambda^2 - 1780}. \tag{4.6}$$

Table 4.1 summarizes the calculated phase matching angles for the 1041-nm pump optical pulses and for the 1103-nm signal optical pulses. From this Table, the in-air phase matching angles θ_p and θ_s for the pump and signal are 35.32° and 35.47° in type-I phase matching and 36.32° and 36.48° in type-II phase matching respectively. The in-air phase

Table 4.1: Calculated phase matching angles for DFG with type-I and type-II configurations in GaSe for the wavelengths $\lambda_p = 1041$ nm, $\lambda_s = 1103$ nm, and $\lambda_i = 18.52$ μm as well as the calculated Fresnel transmission coefficient for the interacting fields.

Type	λ_p (nm)	λ_s (nm)	λ_i (μm)	n_p	n_s	n_i	θ_p	θ_s	θ_i	θ	T_p	T_s	T_i
I	1041	1103	18.52	2.78115	2.79107	2.61931	35.32	35.47	33.00	12.00	84.19%	70.80%	74.33%
II	1041	1103	18.52	2.78026	2.79107	2.60224	36.32	36.48	33.66	12.30	84.58%	70.35%	85.69%

matching angles are calculated by using Snell's equation, phase matching angles, and refractive indices from Eqs. 4.5 and 4.6. The generated MIR radiation has an angle of 33.00° and 33.66° with respect to the normal line at the exit from the back surface of the crystal in the type-I and type-II phase matching configurations respectively.

From experiments, the crystal was rotated roughly by minus one degree as the generated MIR wavelength increased from 16.2 μm to 20.0 μm. For the 16.2-μm MIR radiation, the wavelengths of the pump and signal pulses were 1038 nm and 1109 nm and for the 20-μm MIR radiation, the wavelengths of the pump and signal pulses were 1045 nm and 1102 nm respectively. This result is confirmed by calculations whereas θ_p decreases from 36° to 35° for the type-I phase matching and from 37° to 36° for the type-II phase matching for the corresponding wavelengths cited above.

4.5 Results and discussion on the maximum average power of the generated MIR pulses

A two-color ultrafast spectrum with the center wavelengths of 1041 nm and 1103 nm was generated by the two-color ultrafast YDFA system. The two-color pulses were compressed to an optimal value close to their Fourier transform limits after the two-color pulse compressor. Then, the two color pulses were temporally overlapped by adjusting the delay line in the two-color laser compressor. With an average power of 1350 mW in the 1041-nm blue color pulses and an average power of 76 mW in the 1103-nm red color pulses, ultrashort MIR pulses with an average power of 1.5 mW was achieved. This corresponds to a 2% photon conversion efficiency with respect to the 1041-nm blue color pulses. The average powers of the two color pulses were measured before the GaSe crystal. The FWHM of the blue color and red color pulses were measured $\sim$ 500 fs. From measurements, the two colors had an almost equal spectral bandwidth of $\sim$ 4 nm.

Figs. 4.6(a) and (b) show, respectively, the variations of the average power of the 1041-nm pump pulses and 1103-nm signal pulses, before the GaSe crystal, as a function of

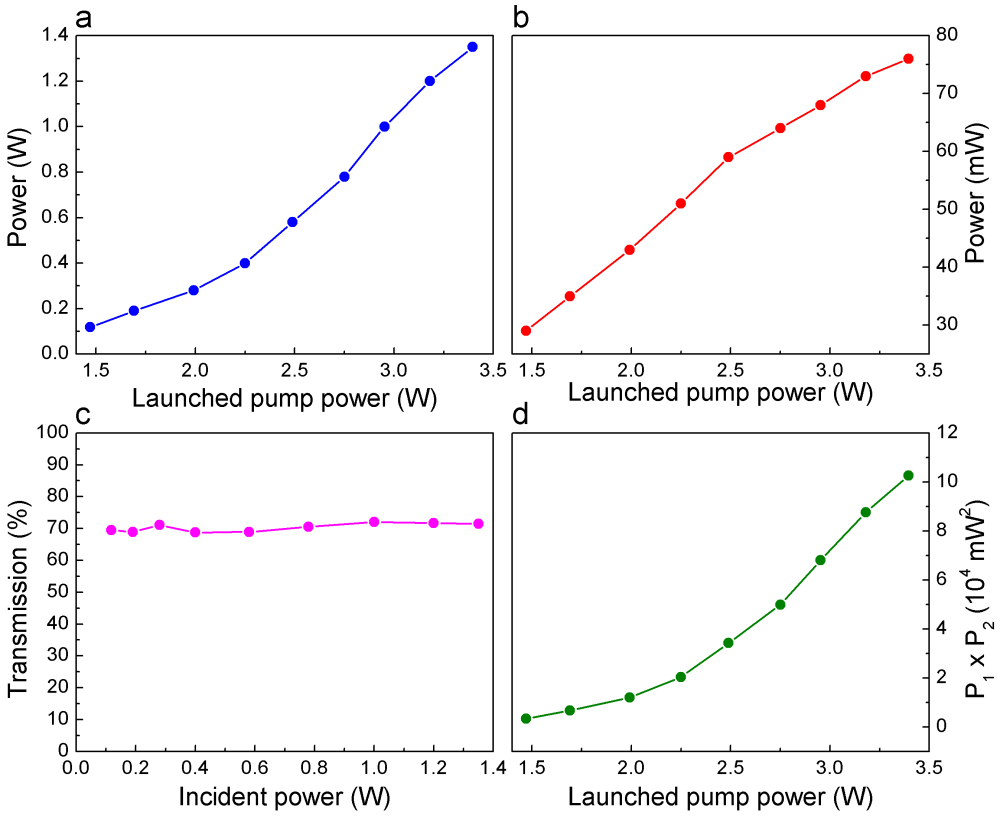

Figure 4.6: Variations of (a) P_1, (b) P_2, and (d) $P_1 \times P_2$ as a function of launched pump power into the main amplifier and (c) the variations of transmission of the input 1041-nm blue color pulses from the 1-mm-thick GaSe crystal as a function of the average power of the input pump pulses. P_1 is the average power of the pump pulses and P_2 is the average power of the signal pulses.

launched optical power of the multi-mode 975-nm laser diode in the main amplifier. From these figures, the maximum average power on the blue color is 1350 mW and on the red color is 76 mW. The coupling efficiency of the pump laser to the inner fiber cladding has been estimated 60%. From these figures, the 1041-nm blue color is in the unsaturated regime and the 1103-nm red color is in the saturated regime. The maximum efficiency of the system for conversion of the launched pump power to the two color power is almost 40% and this is obtained at the maximum pump power. Fig. 4.6(d) depicts the variations of the product of the average power of the two colors $P_1\,P_2$ as a function of the launched pump power into the main amplifier. From this figure, $P_1\,P_2$ could be maximized by increasing

the launched pump power above the 3.5 W. The pump laser power was not increased further in order to avoid damaging the system. Fig. 4.6(c) illustrates the variations of the transmission of the 1041-nm blue-color pulses (focused by the 400-mm focusing lens) from the 1-mm-thick GaSe crystal as a function of the average power of the incident 1041-nm pulses. The crystal angle was at the phase matching angle ($\sim 12^{\circ}$) for the difference frequency mixing of the 1041-nm pump and 1103-nm signal pulses. The phase matching angle measured between the incident beam and the normal line to the crystal surface was roughly 35°. From this figure, the transmission is constant within these average powers of the blue color and there is no clear signature of the two photon absorption process. In the case of the TPA to occur, we would expect to observe a decline from the constant transmission line.

Also from Fig. 4.6(c), the average transmission coefficient of the 1041-nm pulses at the phase matching angle $\sim 12^{\circ}$ is 72.1%. Considering the back reflection from the back surface of the GaSe crystal, the Fresnel transmission coefficient for the 1041-nm radiation is calculated by taking the square root of the 72.1% giving us 84.91%.

Losses from the Fresnel reflection of the pump and signal radiations from the crystal front surface at the phase matching angle decreases the transmitted pump and signal powers into the GaSe crystal. As a result of that, the generated MIR power decreases. Also the Fresnel reflection for the generated MIR radiation from the crystal back surface at the phase matching angle decreases the transmitted MIR power from the GaSe crystal. The transmission coefficient from the Fresnel's equations for the s-polarized light is given by [99]

$$T_s = 1 - \left| \frac{n_i \cos\theta_i - n_t \cos\theta_t}{n_i \cos\theta_i + n_t \cos\theta_t} \right|^2 , \tag{4.7}$$

and for the p-polarized light is given by [99]

$$T_p = 1 - \left| \frac{n_i \cos\theta_t - n_t \cos\theta_i}{n_i \cos\theta_t + n_t \cos\theta_i} \right|^2 . \tag{4.8}$$

where i and t denote the first and second optical media respectively. Table 4.1 summarizes the calculated Fresnel transmission coefficients for the 1041-nm pump, 1103-nm signal, and 18.5-μm MIR radiations for the type-I and type-II phase matching angles. From this Table, the Fresnel transmission coefficient for the 1041-nm pump radiation at the type-II phase matching angle is 84.58% which is very close to the measured transmission coefficient 84.91%. From Table 4.1, for the type-II phase matching, T_s is $\sim 70\%$ for the 1103-nm signal radiation and the Fresnel transmission coefficient at the MIR wavelength 18.5 μm is 86% for the type-II phase matching which is larger than the 74% transmission coefficient for the type-I phase matching.

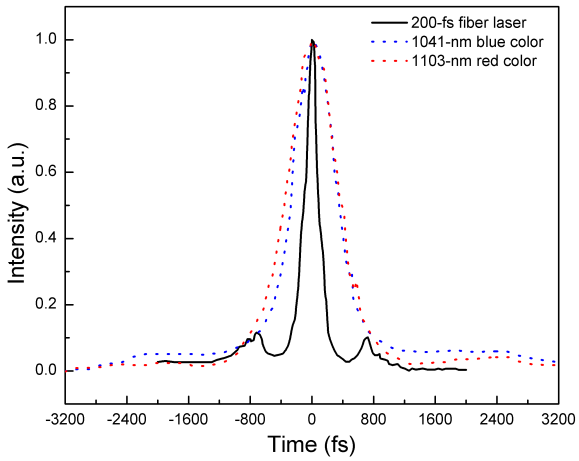

Figure 4.7: Measured autocorrelation pulse intensity as a function of time for the 200-fs Yb:fiber laser pulses and the compressed 1041-nm blue color and 1103-nm red color pulses. The spectra are scaled with the time scale of the 200-fs Yb:fiber laser pulses.

One of the most challenging steps to achieve powerful ultrafast MIR radiations was to have optimally compressed two-color pulses at the same time. The output supercontinuum from the photonic crystal fiber changed over the time which was dramatic on the 1041-nm blue color side resulting in a dramatically altered pulsewidth after the pulse compressor. The optimized pulsewidth showed very much sensitivity with temperature fluctuations and air turbulence in the lab imposing the mechanical stress forces on the PCF. As a result, the phase modulation in the PCF was affected resulting in an unstable supercontinuum. In order to control the spectrum after the PCF, the polarization of the launched 200-fs 1030-nm Yb:fiber laser pulses to the PCF had to be readjusted by rotating the first $\lambda/2$ waveplate to fix the two color spectrum. The pulsewidth of the two-color spectrum (especially on the blue color side) was very sensitive to the polarization of the input pulses to the PCF. After rotating the first waveplate in the system, the other four $\lambda/2$ waveplates, *i.e.*, one before the two-color pulse stretcher, one between the preamplifier and Faraday isolator, one between the Faraday isolator and the polarization maintaining amplifier, and one between the amplifier and the pulse compressor had to be rotated to optimize the two-color power. Meanwhile, the alignment of the two color system changed over the time specially for the preamplifier. For this, most of optical components of the two-color YDFA system needed to be tweaked many times over the course of experiments.

Fig. 4.7 illustrates the pulse intensity as a function of time for the 200-fs Yb:fiber laser pulses, the compressed 1041-nm blue-color pulses and the compressed 1103-nm red-color

pulses. The three temporal pulse profiles were measured using a real time intensity autocorrelator with a few minutes time interval between each measurement for the alignment of the optical pulses into the autocorrelator. This figure shows the results on the autocorrelation measurements right after achieving the 1.5-mW MIR pulses with the two-color spectrum shown in Fig. 4.8(a). From Fig. 4.7, the FWHM of the blue color and red color pulses are minimized to an equal value of $\sim$ 500 fs. To achieve these ultrashort two-color pulses with an almost equal pulsewidth, the two color spectrum was first optimized by tweaking the waveplates to produce the most powerful second harmonic generation from each color after the two-color pulse compressor. For the SHG generation, the two beams were focused onto a BBO crystal by a 10-cm focal-length lens resulting in a green-color light for the blue-color pulses and a yellow-color light for the red-color pulses at the time. Then, the 1041-nm blue color pulses were recompressed by changing the compressor length of the blue-color compressor resulting in an increased power on the SHG green light. The tweaking of the waveplates and the compressor length were repeated until the powers of the green light and the yellow light were maximized. Finally, the red-color pulses were recompressed by changing the compressor length of the red-color pulse compressor resulting in an increased power on the SHG yellow-color light. The whole procedure was repeated for several times until nearly Fourier transform limited two-color pulses measured from the two-color spectra were achieved. The average power of the SHG green-color light was more than 10 mW and that of the SHG yellow-color light was more than 1 mW. It was possible to get more than $\sim$ 3 mW average power on the yellow-color light by optimizing the two-color YDFA system. At the time, the FWHM of the red color pulses was $\sim$ 260 fs. However, the blue-color pulses could not be recompressed to the nearly bandwidth limited pulses. Now, the optimal length of the blue-color pulse compressor was 134 mm and the optimal length of the red-color pulse compressor was 310 mm. The two-color stretcher has two 30-cm focal-length lenses for stretching each color. The length between the first grating and the first focusing lens was 23 cm, the length between the second lens and the second grating was 45 mm for the 1041-nm blue color pulses and was 182 mm for the 1103-nm red color pulses. Finally, the two color pulses were temporally overlapped by moving the back mirror of the blue-color compressor. This was accomplished by producing the sum frequency generation of the two color pulses in the BBO crystal.

Fig. 4.8(a) depicts the two-color ultrafast spectra centered at the wavelengths 1041 nm and 1103 nm with the average powers corresponding to the four highest average powers illustrated in Figs. 4.6(a) and (b). From this figure, the FWHM of the spectra of the two colors are equally $\sim$ 4 nm. From the relation $t = 0.441\lambda^2/(c\,\Delta\lambda)$ [85], the $\sim$ 4-nm FWHM is enough to generate 400-fs pulsewidth Fourier transform limited Gaussian pulses from the 1041-nm blue color pulses.

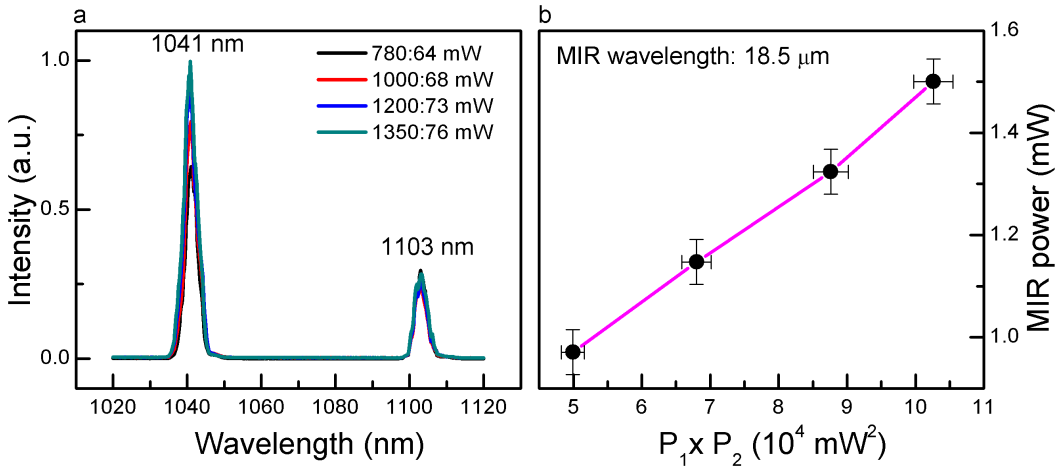

Figure 4.8: (a) Two-color ultrafast spectra used to measure the scalability of the average power of the short-pulse MIR radiation. (b) Variations of the average power of the MIR pulses as a function of $P_1 \times P_2$.

Fig. 4.8(b) depicts the variations of the corresponding average power of the short-pulse MIR radiation (centered at the wavelength 18.5 μm) generated by difference frequency mixing of the two-color spectra shown in Fig. 4.8(a) as a function of the product of the average powers of the two short-pulse colors, *i.e.* $P_1 \times P_2$. From Fig. 4.8(b), the maximum average power of the MIR pulses is 1.5 mW corresponding to the average powers of $P_1 = 1350$ mW and $P_2 = 76$ mW of the incident pump pulses and signal pulses onto the GaSe crystal respectively. The average power of the two color pulses were measured before the GaSe crystal. From this figure, the average power of the MIR pulses scales up linearly with $P_1 \times P_2$. This is justified as follows.

The idler intensity I_i in the plane-wave fixed-field approximation (undepleted pump power and fixed signal power) under perfectly phase matching condition is given by [61]

$$I_i = \frac{8\pi^2 d_{\text{eff}}^2}{\epsilon_0 c\, n_i\, n_p\, n_s\, \lambda_i^2} I_p\, I_s\, L^2, \tag{4.9}$$

where I_p and I_s are, respectively, the peak intensities of the pump and signal laser pulses in the NLO crystal, d_{eff} is the effective 2nd-order nonlinear optical susceptibility, L is the interaction length in the NLO crystal, ϵ_0 is the permittivity of the free space, c is speed of light in vacuum, n_i, n_p, and n_s are, respectively, the refractive indices of the GaSe crystal at the phase matching angle for the idler, pump, and signal radiations, and λ_i is the wavelength of the MIR pulses in vacuum. Now, we rewrite Eq. 4.9 in terms of the

average power of the three fields

$$P_i = T_p\, T_s\, T_i\, \frac{8\pi^2 d_{\text{eff}}^2}{\epsilon_0 c\, n_i\, n_p\, n_s\, \lambda_i^2\, A\, t\, f} P_p\, P_s\, L^2 g, \tag{4.10}$$

where we included the Fresnel transmission coefficients of T_p, T_s, and T_i, respectively, for the incident pump and signal pulses to the GaSe crystal and the output MIR pulses from the GaSe crystal. Considering the plane wave approximation, we also replaced the peak intensity with the peak power divided by the beam area ($I_{\text{peak}} = P_{\text{peak}}/A$) and assumed that the pump, signal and idler optical beams have the same beam area A in the NLO crystal. We then replaced the peak power with the average power using ($P_{\text{peak}} = P_{\text{ave}}/t\, f$) where t is the pulsewidth and f is the repetition frequency of the pulses. The pulsewidth of the three interacting fields are not necessarily equal. For this, the factor g has been included in the equation.

From Eq. 4.10, the average power of the MIR pulses scales up with the product of the average powers of the pump and signal pulses $P_p \times P_s$ which agrees very well with the results shown in Fig. 4.8(b). Thus, in this thesis, the two-color ultrafast YDFA system was optimized for maximizing the $P_p \times P_s$ product as was explained in Sections 3.3 and 3.4.

The MIR power scales up by tight focusing the interacting pump and signal radiations. This can be seen from Eq. 4.10 by the beam area A in the denominator. The tight focusing is at the expense of decreasing the interaction length. This is because of the walk-off angle between the o-beam and e-beam in the birefringent crystals. For the o-beam, the direction of propagation of the wavevector and Poynting vector is parallel but for the e-beam they are not. The walk-off angle $\rho(\theta)$ between the propagation direction of the e-beam and o-beam is given by [100]

$$\tan\rho = \frac{1}{2}[(\frac{n_{\text{o}}}{n_{\text{e}}})^2 - 1]\sin 2\theta, \tag{4.11}$$

where θ is the phase matching angle, n_o is the ordinary refractive index, and n_e is the principle value of the extraordinary refractive index. From this equation, for the type-II phase matching angle of 12.3° in the GaSe crystal, the walk-off angle for the 1041-nm as an e-beam is 3.60° ($n_{\text{o}} = 2.79925$ obtained from Eq. 4.5 and $n_{\text{e}} = 2.45318$ obtained from Eq. 4.6 at $\lambda = 1041$ nm). From this walk-off angle, the 1041-nm pump e-beam and the 1103-nm signal o-beam are separated by 63 μm on the back surface of the 1-mm-thick GaSe crystal. At the first glance, this puts a 63-μm limit on the beam radius at the focusing point on the crystal surface. Now, the beam diffraction angle comes into play by which the two beams are not completely separated at the crystal back surface but they still partially overlap. Therefore, one tries to optimize the beam spot size to make a balance with the

walk-off angle to increase the efficiency of the DFG process. For this, two lenses with the focal lengths of 40 cm and 1 m were tested. The highest MIR power was achieved with the 40-cm lens.

The focused beam size is also limited by the threshold damage intensity of the crystal surface and the threshold intensity of the two photon absorption process. Considering the 7-GW/cm^2 damage threshold intensity for the 70-ps pulses reported for the GaSe crystal [72], for the 500-fs laser pulses, the damage threshold intensity is 1 TW/cm^2 (in fact the damage threshold fluence should not exceed 1 J/cm^2 [72]). From this, for the 500-fs 50-MHz 1350-mW laser pulses, the beam radius is $\sim$ 1.3 μm at the damage threshold intensity. On the other hand, the TPA threshold intensity of the GaSe has been reported as $\sim$ 100 MW/cm^2 [72]. This puts a 130-μm limitation on the minimum beam radius of the focused 1041-nm 500-fs pump pulses. Obviously, the TPA gives a larger critical beam radius for the 1041-nm pump pulses. From plane-wave approximation, the beam radius at the focusing point on the GaSe crystal is approximately calculated 100 μm after focusing the pump pulses with an initial beam radius of $\sim$ 2.5 mm by the 40-cm focal-length focusing lens. This beam radius is smaller than the TPA limit and as cited above it was experimentally found to give a good balance between the minimum beam spot size and the walk-off angle in the 1-mm-thick GaSe crystal with no evidence of the TPA.

After achieving phase matching, the crystal was rotated about its optic axis for maximizing the MIR output. In fact, this rotates the crystal into the azimuthal angle ϕ. The detector response was maximized at angles approximately 0, 60, 120, 180, 240, and 300. The effective 2nd-order nonlinear optical susceptibility d_{eff} is a function of the azimuthal angle ϕ for the type-I phase matching condition by [63]

$$d_{\text{eff}} = d_{22} \cos\theta \sin 3\phi, \tag{4.12}$$

and for the type-II phase matching by [63]

$$d_{\text{eff}} = d_{22} \cos^2\theta \cos 3\phi, \tag{4.13}$$

where d_{22} is equal to 54 pm/V and is the only non-zero second-order nonlinear optical coefficient of GaSe and θ is the phase matching angle. From Eq. 4.12, for the type-I phase matching, d_{eff} is maximized for the azimuthal angles of 30, 90, 150, 210, 270, and 330. From Eq. 4.13, for the type-II phase matching, d_{eff} is maximized for the azimuthal angles obtained experimentally and cited above.

Equation 4.11 has been used to estimate the average power of the MIR pulses for P_p = 1350 mW and P_s = 76 mW in the type-II phase matching configuration. From measurements, the average pulsewidth of the two color pulses is roughly 500 fs as discussed

previously. The beam radius of the focused pump and signal radiations is assumed to be 100 μm. For the sake of simplicity, we assume that $g = 1$. The pulse repetition frequency f is 50 MHz and the refractive indices and Fresnel coefficients are given in Table 4.1. For the type-II phase matching, we obtain an average power of 0.8 mW for the ultrashort MIR pulses at the wavelength 18.5 μm. The measured average power of the MIR pulses at the wavelength 18.5 μm was 1.5 mW which has the same order of magnitude of the calculated power.

Finally, I would like to discuss the group velocity walk-off (GVW) on the two color pulses in the GaSe crystal. The GVW separates the two mixing pulses temporally [68]. This brings down the efficiency of MIR generation in long NLO crystals. The GVW in the mixing crystal with a thickness of L is defined by [68]

$$\text{GVW} = L\,(v_p^{-1} - v_s^{-1}), \tag{4.14}$$

where v_p and v_s are the group velocities of the pump and signal pulses in the NLO crystal. For an NLO crystal with a thickness L, it is required to have the GVW much shorter than the pulse durations. The group velocity is given by [84]

$$v_g^{-1} = \frac{1}{c}\left(n - \lambda\frac{dn}{d\lambda}\right), \tag{4.15}$$

where c is the speed of light in vacuum, n is the index of refraction of the medium, and λ is the wavelength. For the e-polarized 1041-nm blue-color pulses, n_e was calculated from Eq. 2.5 at the phase matching angle 12.3° and Eq. 4.6 for the two wavelengths adjacent to the 1041 nm and then v_g^{-1} was calculated from Eq. 4.15. For the o-polarized 1103-nm red-color pulses, n was calculated from Eq. 4.5 for the two wavelengths adjacent to the 1103 nm and then v_g^{-1} was calculated from Eq. 4.15. From calculations, for the 1041-nm pulses we obtain $v_g^{-1} = 9.74958$ ps/mm and for the 1103-nm pulses we obtain $v_g^{-1} = 9.73967$ ps/mm. Thus, from Eq. 4.14, the GVW is calculated 10 fs for the 1041-nm pulses and 1103 nm for traveling in a 1-mm-thick GaSe crystal. Obviously, the calculated GVW is much smaller than the pulsewidth of the 500-fs two color pulses. In the tunable MIR experiments, the delay time between the two color pulses was slightly altered to compensate the GVW in the GaSe crystal for different pump and signal wavelengths.

4.6 Tunable ultrafast MIR generation

In order to explore the MIR tuning range, the tuning range of the two-color ultrafast YDFA system was investigated. For this, the central wavelengths of the two-color seed pulses to

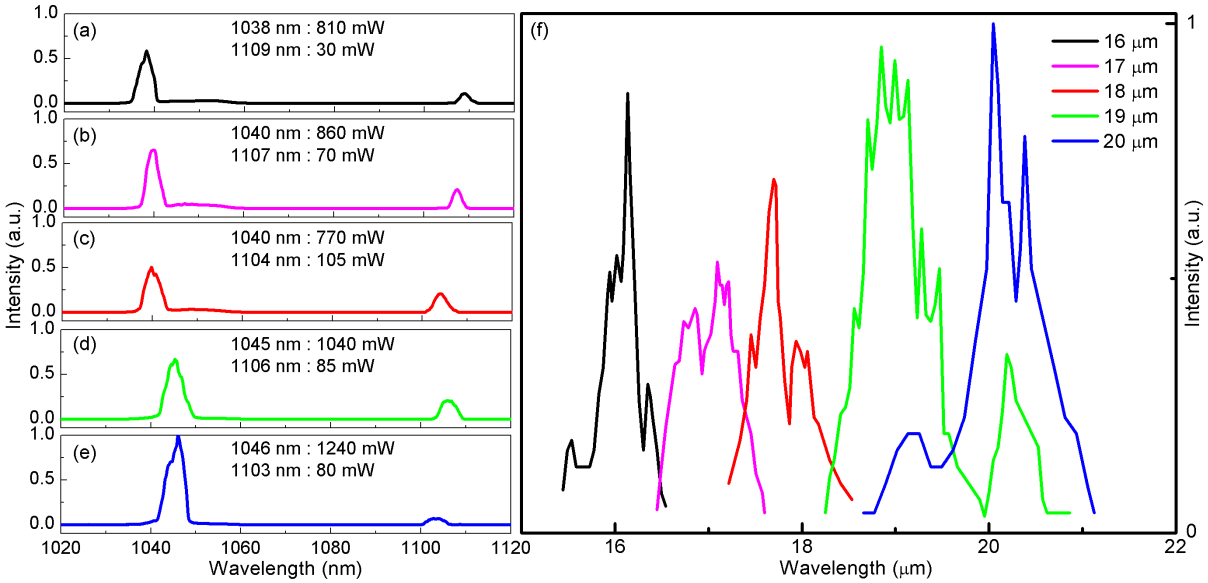

Figure 4.9: (a-e) Experimental two-color ultrafast spectra, scaled with the peak of the spectrum in the panel (e) (in the panels, can be seen the peak wavelength and average power of each color). (f) Corresponding generated ultrafast MIR spectra, scaled with the peak of the 20-μm spectrum. The color of the two-color spectrum matches with the color of the corresponding MIR spectrum. The little bump on the right shoulder of the blue color seen in panels (a) to (c) is the ASE which was not blocked in the pulse compressor. (Published in Ref. [96].)

the preamplifier were changed and the amplified two-color spectrum was measured before the MIR setup. The central wavelengths of the two-color seed were changed via adjusting the opening of the four knife edges in the two-color pulse stretcher. Two notch filters were used in series between the preamplifier and the main amplifier to block the ASE generated by the preamplifier. The central wavelength and rejection bandwidth of the two notch filters are, respectively, 1065 nm and 45 nm for a normal incident beam. However, these can be changed by varying the incident angle. By tuning the incident angles of the two notch filters, a tunable rejection bandwidth between 48 and 55 nm centered at 1073 nm was achieved. Having set the knife edges and notch filters, the five $\lambda/2$ waveplates were adjusted to maximize the average power of the two color pulses and minimize the pulsewidth of the two colors after the pulse compressor as explained above.

The blue color from the lower wavelength side and the red color from the upper wavelength side were limited to 1038 nm and 1109 nm respectively. Any attempt to spectrally

separate the two colors further apart was not successful due to insufficient seed power to the preamplifier. Increasing the tuning range will require either a higher power seed or another preamplifier. Because of the 20-μm cut-off absorption wavelength of GaSe, the peak wavelengths at minimum color separation were 1046 nm and 1103 nm.

The two colors were temporally overlapped using the movable mirror in the blue-color compressor arms. In the MIR setup, the two colors are made orthogonally polarized, collinear, and focused into the 1-mm-thick GaSe crystal as explained earlier. Phase matching was achieved by rotating the GaSe crystal perpendicular to the principal plane. The crystal orientation at the phase matching angle is approximately 35°. The crystal was rotated by approximately 1 degree for the generation of the MIR wavelengths between 16 and 20 μm. The MIR spectra were measured by a 50 grooves/mm monochromator. The monochromator was calibrated for the MIR wavelengths by the 1105-nm red-color pulses through the detection of the first order to the 19th order of diffraction.

Figs. 4.9 shows the two-color spectra with a 2 nm resolution and corresponding MIR spectra with a 0.01 μm resolution. From these figures, the peak MIR wavelengths agree with the difference frequency of the peak wavelengths of the blue and red colors. Note that, one convenient way to generate tunable MIR is to fix one of the mixing wavelengths and change the other wavelength, however both colors are varied to optimize the product of their power. From Fig. 4.9(f), it can be seen that the generated MIR at the central wavelengths 16, 18, and 20 μm are very sharp at the peak wavelength when the blue color is sharp at the peak wavelength. From this figure, the ratio of the MIR spectral weight at 19.0 μm to that at 17 μm is 1.45. This number agrees with 1.47 that is the ratio of P_1P_2 between the corresponding two-color spectra.

Based on measured MIR spectra, the MIR pulses have a picosecond pulse duration in the wavelengths 16-20 μm. The FWHM of measured spectra of the MIR pulses increases from 0.3 μm to 0.8 μm as the MIR wavelength increases from 16 μm to 20 μm. According to Fourier transform theory and from Eq. 2.8, the FWHM of the MIR spectra corresponds to a picosecond pulse duration assuming that the MIR pulses are perfectly Fourier-transform-limited Gaussian pulses.

4.7 Conclusion

In summary, in this research, a tunable two-color ultrafast Yb:fiber chirped pulse amplifier was developed. An average power of roughly 200 mW was achieved after the single-clad YDFA co-pumped with 350 mW and counter-pumped with 500 mW using 986-nm single-mode laser diodes and seeded with a 2.5-mW two-color spectrum centered at 1041 nm and

1103 nm. The average power on the two-color spectrum was increased to more than 2.7 W by a polarization maintaining double-clad YDFA counter-pumped with a 6-W, 975-nm laser diode. A maximum wavelength separation of 71 nm was achieved between the two colors in the watt-level regime. Thanks to the preamplifier that decreased the amplified spontaneous emission from the main amplifier noticeably. Any attempt to spectrally separate the two colors for more than 71 nm was not successful due to insufficient seed power to the preamplifier resulting in the ASE lasing spikes in the main amplifier. Increasing the wavelength separation will require either a higher power seed or another preamplifier. The amplified two-color pulses were compressed to a 500-fs pulsewidth using a two-color transmission grating pulse compressor.

A tunable DFG-based short-pulse MIR source was developed between 16 μm and 20 μm by difference mixing of the two short-pulse colors with the peak wavelengths in the range of 1038-1046 nm and 1103-1109 nm from the output of the two-color ultrafast YDFA system. The MIR range from the short-wavelength side was limited to the 71-nm wavelength separation limit between the two colors. The MIR range from the long-wavelength side was limited to the 20-μm cut-off transparency range of the GaSe crystal. Based on measured MIR spectra, the MIR pulses have a picosecond pulse duration in the wavelengths 16-20 μm. The FWHM of measured spectra of the MIR pulses increases from 0.3 μm to 0.8 μm as the MIR wavelength increases from 16 μm to 20 μm. According to Fourier transform theory, the FWHM of the MIR spectra corresponds to a picosecond pulse duration assuming that the MIR pulses are perfectly Fourier-transform-limited Gaussian pulses.

An average power of 1.5 mW was achieved at $\sim$18.5 μm corresponding to the difference frequency of 500-fs two-color pulses with the peak wavelengths of 1041 nm and 1103 nm and average powers of 1350 mW and 76 mW respectively. From theoretical calculations based on the plane-wave fixed-field approximation, we obtain an average power of 0.8 mW for the short-pulse MIR radiation at the wavelength 18.5 μm which agrees with the order of magnitude of the measured 1.5-mW average power. From measurements with the 500-fs, 50-MHz, 1041-nm pulses with an estimated peak intensity up to 170 MW/cm^2, there was no evidence of the two photon absorption in the 1-mm GaSe crystal.

Finally, the positive-chirped short-wavelength pulses acquired a negative chirp before the two-color pulse compressor which cannot be explained by third order dispersion of the total fiber length in the system. The negative chirp was confirmed by the optimized compressor length for the nearly bandwidth limited 500-fs, 1041-nm pulses. This may originate from an absorption-induced refractive index change in the ytterbium doped fiber amplifiers on the physical ground of the strong reabsorption process on short-wavelength side of YDFA gain profile.

Chapter 5

Concluding remarks

This thesis focused on the development of a tunable two-color ultrafast ytterbium doped fiber amplifier system for the generation of tunable short-pulse mid-infrared radiation. Ytterbium doped fiber amplifier is a suitable laser gain medium in the two-color laser systems mainly because of its two superior properties: the large gain bandwidth and high average output power. Moreover, YDFA is pumped by commercially available 975-nm laser diodes because of its 975-nm peak absorption. In the two-color ultrafast YDFA system, two-color pulses are amplified in the same YDFA simultaneously. This was found useful for the elimination of thermo-mechanical noise on the phase difference between the two laser pulses and therefore it was unnecessary to control the pulse jitter electronically.

In summary, in this research, a tunable two-color ultrafast Yb:fiber chirped pulse amplifier was developed. An average power of roughly 200 mW was achieved after the 7.5-m-long single-clad YDFA (preamplifier) co-pumped with 350 mW and counter-pumped with 500 mW using 986-nm single-mode laser diodes and seeded typically with a 2.5-mW two-color spectrum centered at 1041 nm and 1103 nm. The average power on the two-color spectrum was increased to more than 2.7 W by a 10.5-m-long polarization maintaining double-clad YDFA (main amplifier) counter-pumped with a 6-W, 975-nm laser diode. A maximum wavelength separation of 71 nm was achieved between the two colors in the watt-level regime. This achievement was particularly made possible by optimizing the preamplifier and main amplifier stages. With an increased output power from a powerful preamplifier, the ASE power decreased drastically from the main amplifier. Furthermore, with the main amplifier which is now a polarization maintaining YDFA, the efficiency of the polarization transmission grating pulse compressor increased. Any attempt to spectrally separate the two colors for more than 71 nm was not successful due to insufficient seed power to the preamplifier resulting in the ASE lasing spikes in the main amplifier. The

amplified two-color pulses were compressed to a 500-fs pulsewidth using a two-color transmission grating pulse compressor. Typical average powers of 1200 mW and 100 mW were achieved, respectively, on the short wavelength and long wavelength pulses after the pulse compressor.

Based on experimental facts, short-wavelength pulses acquired a negative chirp before pulse compression which cannot be explained by third order dispersion of the total fiber length in the system. The negative chirp was justified by the optimized compressor length for the nearly bandwidth limited 500-fs, 1041-nm pulses. This may originate from an absorption-induced refractive index change in the ytterbium doped fiber amplifiers on the physical ground of the strong reabsorption process on the short-wavelength side of the YDFA gain profile. For this, a future investigation on the refractive index change of the Yb:fibers in the operation regime will help to elucidate this behavior.

A tunable DFG-based short-pulse MIR source was achieved between 16 μm and 20 μm by difference mixing of two collinear and orthogonally polarized short pulses in a 1-mm-long GaSe crystal. The peak wavelengths of the pulses were tuned in the wavelength ranges of 1038-1046 nm and 1103-1109 nm. The MIR range from the short-wavelength side was limited to the 71-nm wavelength separation limit between the two colors and from the long-wavelength side was limited to the 20-μm cut-off transparency range of the GaSe crystal. Based on measured FWHM of MIR spectra, the MIR pulses had a picosecond pulse duration in the wavelengths 16-20 μm assuming that the MIR pulses were perfectly Fourier-transform-limited Gaussian pulses. The FWHM of measured spectra of the MIR pulses increases from 0.3 μm to 0.8 μm as the MIR wavelength increases from 16 μm to 20 μm.

An average power of 1.5 mW was achieved at the MIR wavelength $\sim$18.5 μm by difference frequency of 500-fs two-color pulses with the peak wavelengths of 1041 nm and 1103 nm and average powers of 1350 mW and 76 mW respectively.

Closely linked to the experimental setup, the amplification of two-color laser pulses was modeled in the YDFAs as a function of fiber length. For the modeling, the rate and propagation equations for a two-level energy scheme in the cw regime were used and a LabVIEW program was developed in order to numerically calculate the variations of power of the two-color, ASE, and pump laser spectra at the output of the preamplifier and main amplifier YDFAs as a function of fiber length. The modeling was successful to find the optimum fiber length of the preamplifier and main amplifier in order to achieve two-color laser pulses with (i) a wavelength separation more than 70 nm, (ii) a combined average power of more than 2.7 W optimized for the MIR generation, and (iii) a sufficient bandwidth at each color for the subpicosecond pulse duration. From the modeling, the

output average power is 2.7 W, the P_1 P_2 is maximized, and the spectral bandwidth of the short-wavelength color is roughly 4 nm. The 4-nm bandwidth is enough to achieve the 500-fs pulses at the wavelengths 1041 nm and 1103 nm. The modeled two-color spectra and average power of the two color pulses after the Yb:fiber amplifiers agreed very well with the experimental results.

The tunable two-color ultrafast Yb:fiber chirped pulse amplifier that was developed in this thesis will find applications for example in pump-probe ultrafast spectroscopy, short-pulse MIR generation as demonstrated in this thesis, and optical frequency combs generation. The tunable short-pulse MIR radiation will find applications for example in time-resolved MIR spectroscopy and remote gas detection. The 16-20 μm MIR range is in the long wavelength side of the "molecular fingerprint" where few ultrafast laser sources with a broad tunability range can be found within this part of spectrum. At the time of writing of this thesis and to the best knowledge of the author, the 1.5-mW average power of the short-pulse MIR radiation at the wavelength 18.5 μW is the maximum average power that has been generated from applying DFG technique to two short pulses. The maximum tunability range of the MIR pulses generated from the two-color ultrafast YDFA system in this research is not as broad as that generated from two-color ultrafast Ti:sapphire lasers + DFG, OPO + DFG, OPG, and OPA. However, for those applications required short-pulse MIR radiation in the 16-20 μm, the two-color ultrafast YDFA is advantageous for its high power, compactness, robustness, maintenance free, and lower cost.

APPENDICES

Appendix A

Ytterbium doped silica fiber, optical properties, concentration quenching, and lifetime quenching

In condensed matter, optical properties of solids are described in terms of outermost energy levels of the constituent atoms. This is because, these energy levels have lower energies compared to the core electronic shells and therefore they can resonate with low-energy photons. For this, in Appendix A.1, I will describe the energy levels in the outermost electronic shell of Yb^{+3} in silica fibers and, based on that, I will describe some of its resultant absorption and emission properties in the near infrared region.

A large Yb^{3+} concentration and a long fluorescence lifetime are highly desired in Yb:fiber amplifiers because they result to store a large amount of optical energy in the fiber. A mechanism called "concentration quenching" is responsible for lowering the population density of the excited Yb^{3+} ions and the fluorescence lifetime of Yb^{3+} in highly doped Yb:fibers [14,15,101]. These will be explained in Appendices A.2 and A.3. With co-doping the Yb:fibers with aluminum and phosphorus the concentration quenching effect can be decreased resulting to an increased ytterbium concentration and to a long fluorescence lifetime of ytterbium ions in the silica fibers [102]. This will be explained in Appendix A.3. As we will see, two major types of concentration quenching are prohibited in Yb:fibers. This has been simplified the modeling of the YDFA's in this thesis. Furthermore, in the modeling of the YDFA's in this thesis, the fluorescence lifetime of the Yb:fiber is assumed to be 0.8 ms. This will be justified under the subject of lifetime quenching.

A.1 Electronic configuration and optical properties of Yb^{3+} in the silica fiber

Lanthanoid series are fifteen chemical elements located in the first place of the third row of transition elements in periodic table. Lanthanoids are most stable in the trivalent state of ionization in condensed matter [14, 15, 103]. Ytterbium with an atomic number of 70 is the fourteenth chemical element in the lanthanoid series. Lanthanoids are also well known for filling the $4f$ orbitals. The $4f$ shell is not the outer shell but it lies inside the closed shells of $5p^6 6s^2$. Because of screening by core electrons, the two electrons in the atomic orbital $6s^2$ are loosely bound to nucleus, therefore, they are the first two electrons which are removed from ytterbium. The next electron will be removed from the f shell. Thus, the electronic configuration of Yb^{3+} takes the form $[Xe]4f^{13}$ which is a reduced electronic configuration of $[Xe]4f^{14}6s^2$ for the neutral ytterbium.

The $4f^{13}$ electrons in Yb^{3+} are shielded by the $5p^6$ electrons from environment. This $5P^6$ shielding has major consequences on the absorption/emission properties of Yb^{3+} considering the variation of host material. That is the absorption/emission spectra arising from $4f - 4f$ transitions do not suffer very much from changing the host material. This feature becomes attractive when similar gain profiles from Yb:fibers, in some extent, is desired regardless of the host material composition. For example, Yb:fiber is co-doped with materials such as aluminum and phosphorus for a better performance which will be described in Appendices A.2 and A.3.

The infrared spectrum of Yb^{3+} is a result of transitions between the energy levels of the $4f$ states. Spin-orbit $(L - S)$ coupling, *i.e.* Russell-Saunders coupling, has been used to explain the energy levels of the $4f$ electrons in lanthanoids [14, 15, 103]. From Hund's rule, for the thirteen electrons in the $4f$ shell of Yb^{3+}, we find the total orbital momentum quantum number $L = 3$ and the total spin quantum number $S = 1/2$. The total angular momentum quantum number J lies between $L + S$ and $|L - S|$ which only takes $7/2$ and $5/2$ for Yb^{3+}. These two sates are ${}^2F_{7/2}$ and ${}^2F_{5/2}$ where 2 stands for $2S + 1$ and F stands for $L = 3$ in this notation. Moreover, from Hund's third rule, for more than half-full shells such as the $4f^{13}$ shell for Yb^{3+}, the ground state is the energy state with a larger total angular momentum quantum number, that is ${}^2F_{7/2}$ for Yb^{3+}. This simple two-level energy scheme prohibits the up-conversion and cross relaxation energy transfers as explained in Appendix A.2.

For ytterbium doped crystals or glasses (silica fibers), the ${}^2F_{7/2}$ and ${}^2F_{5/2}$ states are further split into stark levels through an interaction with local crystal fields. This crystal field splitting is a consequence of breaking field symmetry in the environment of Yb^{3+}.

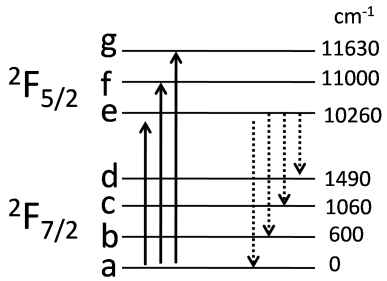

Figure A.1: Energy diagram of Yb^{3+} in silica fibers. The ground state $^2F_{7/2}$ includes four Stark levels and the excited state $^2F_{5/2}$ includes three Stark levels. (Reproduced with permission from Ref. [105]. ©1995 IEEE.)

Therefore, the symmetry of the crystal structure is a key factor to the number of Stark levels. Moreover, the energy separation between the Stark levels depends on the local crystalline field strength applied on the Yb^{3+} ions. For example, for a crystal electric field with a cubic symmetry the ground state $^2F_{7/2}$ splits into three Stark levels and the excited state $^2F_{5/2}$ splits into two Stark levels but for a local electric field with a rhombic symmetry the number of Stark levels increases, respectively, to four and three as a result of lowering the crystal field symmetry [104].

Fig. A.1 illustrates the ground state and excited state of Yb^{3+} in silica fibers [105]. As can be seen, the ground state has split into four Stark sub-levels and the excited state has split into three Stark sub-levels. From this figure, those upward vertical lines show major electronic transitions for absorption and those downward vertical lines show major electronic transitions for emission.

At room temperature ($kT \sim 200$ cm^{-1}) and when there is no external excitation, the stark sub-levels in the excited state $^2F_{5/2}$ are almost empty because of their large energy separations from the energy level (a) in the ground state manifold. For example, from Boltzmann factor, *i.e.* $e^{-E/kT}$, we obtain a factor of $e^{-10260/208} = 3.8 \times 10^{-22}$ for the probability of occupation of the Stark sub-level (e) which is quite a negligible number.

The Stark sub-levels (f) and (g) are not stable. That is, when they are populated by electronic transitions from the ground state through an absorption process they rapidly decay to the stark sub-level (e). This process is a non-radiative decay and is supported by creation of phonons resulting to the generation of heat in Yb:fibers. As a result, high power Yb:fibers should be cooled appropriately. Moreover, because of this decay process, peak emission lines happen for transitions between the Stark sub-level (e) and the four Stark sub-levels in the $^2F_{7/2}$ manifold. From Table A.1, these emission lines are 975, 1035,

Table A.1: Absorption and emission peaks of Yb^{3+} in silica fibers corresponding to transitions shown in Fig. A.1.

Emission Peak		Absorption Peak	
Transition	Wavelength (nm)	Transition	Wavelength (nm)
e → a	975	a → e	975
e → b	1035	a → f	909
e → c	1087	a → g	860
e → d	1140		

1087, and 1140 nm.

The Boltzmann factor for the Stark sub-level (b) in the ${}^2F_{7/2}$ manifold is ~ 0.05 which is obviously not a negligible number. For example, for a ytterbium concentration of 8×10^{25} m^{-3}, the population of the sub-level (b) is 4×10^{24} at room temperature. This causes an electronic transition between the sub-levels (b) and (e) corresponding to an absorption at 1035 nm. This becomes the well-known re-absorption problem for Yb:fibers working at wavelengths close to the 1035 nm. The problem becomes serious when there is not enough pump power in the Yb:fiber to provide gain for the 1035 nm signals. Three peak absorption lines happen for transition between the energy level (a) and the three Stark sub-levels in the ${}^2F_{5/2}$ manifold. From Table A.1, the three peak absorption lines are 975, 909, and 860 nm.

The silica fiber does not have any symmetry attributed to crystalline solids. This type of solids are called amorphous solids or just glasses. Because of lack of crystalline symmetry in amorphous solids, the local crystal field does not have any symmetry. For this, the stark energy levels of Yb^{3+} ions in the silica fibers are not sharp any more but they are broadened. From this line broadening and the fact that the Stark sub-levels are separated by a small amount of energy (between 400 cm^{-1} and 800 cm^{-1}), they overlap which means that the ground state ${}^2F_{7/2}$ and the excited state ${}^2F_{5/2}$ become energy bands in the Yb:fibers. For this reason, the absorption and emission spectra of Yb:fibers are continuous.

A.2 Concentration quenching

Concentration quenching (reduction of concentration) is a depopulation mechanism of the upper state energy level of a laser gain medium through undesired energy transfer processes which lowers the quantum efficiency [15]. Two types of concentration quenching

are "cooperative up-conversion" and "cross relaxation". In the cooperative up-conversion, for the two ions initially in the excited state, the energy is exchanged in a way that one ion relaxes to the ground state and the other ion goes to an upper energy state. In the cross relaxation, one ion is initially in the excited state and the other ion is in the ground state. The energy is exchanged between the two ions in a way that both ions migrate to an intermediate energy state. Noticing that the two mechanisms need three energy states, fortunately, non of these mechanisms can happen for Yb:fibers because Yb^{3+} ions has just two multiplet manifolds in the 900-1200 nm. However, the energy can be exchanged from ions to ions in a "cooperative energy transfer" mechanism. This mechanism also does not result to the concentration quenching in the Yb:fibers unless the energy transfer process is terminated by a defect point in highly doped Yb:fibers. The highly doped Yb:fibers usually refer to the ytterbium concentration more or less above 10^{25} m^{-3}.

The concentration quenching in Yb:fibers may also happen from a mechanism called "multi-phonon non-radiative relaxation". The multi-phonon relaxation to the ground state is undertaken through a chain of transitions by a number of phonons. For this happens, the only assumption is the presence of thermally excited phonons originated from the silica host. Another consequence of the multi-phonon non-radiative relaxation is a decreased fluorescence lifetime which lowers the stored energy in the Yb:fibers.

A.3 Lifetime quenching from multi-phonon relaxation

The change in the fluorescence lifetime in terms of number of phonons and temperature can been found rigorously [106, 107]. A simple approach to derive the same functionality can be taken by the use of combinational theory as it follows.

The mean number of thermally excited phonons is given by Bose-Einstein population number:

$$n = \frac{1}{e^{h\nu/kT-1}}, \tag{A.1}$$

where h is the Plank constant, k is the Boltzmann constant, and T is the absolute temperature. For n phonons and g energy levels, we use a simple illustration by n dots and *g-1* vertical lines [99]. For example, for three phonons and two energy levels, the phonons can be distributed among the energy levels through these configurations: •••|, ••|•, •|••, and |••• where for a bullet before a vertical line means that the phonon is in the upper state and vice versa. From the theory of combinations, the total number of combinations of *n+g-1* distinguishable objects is (*n+g-1*)!. However, for n identical objects (bullets)

and *g-1* identical objects (lines), the total distinct combinations must be divided by $n!$ and $(g\text{-}1)!$. Thus, the total distinct combinations is [99]

$$W(n,g) = \frac{(n+g-1)!}{n!(g-1)!} \tag{A.2}$$

For a two level system (g=2), the total distinct combinations becomes *n+1*. Because phonons obey Bose-Einstein statistics, n is the Bose-Einstein population number. This dependency has also been discussed in the context of Stokes Raman spectra where Raman spectra exhibit temperature and frequency dependency through the *n+1* factor [108, 109]. For a multi-phonon relaxation process when p phonons are needed to cascadedly bridge the energy gap (ΔE) where for simplicity we assume that $\Delta E = ph\nu$, that is all phonons have identical energy, and as a result of multiplication of probabilities, the number of distinct combinations and consequently the non-radiative relaxation rate grows by a factor of $(n+1)^p$. Thus the non-radiative decay rate is given by [14, 15, 106, 107]

$$\frac{1}{\tau_{nr}} = \frac{1}{\tau_0}(1+n)^p = \frac{1}{\tau_0}(1-\mathrm{e}^{-h\nu/kT})^{-p}, \tag{A.3}$$

where $1/\tau_0$ is the non-radiative decay rate at $T = 0$. Because $1/\tau_0$ behaves as an exponential function, Eq. A.3 is written into a phenomenological form [14, 15, 107]

$$1/\tau_{nr} = Be^{-\alpha\Delta E}(1-e^{-h\nu/kT})^{-p} \tag{A.4}$$

In the silica glass the phonon energies are between 400 cm^{-1} and 1100 cm^{-1} [110]. The largest probability for a multiphonon non-radiative transition corresponds to the smallest number of phonons needed to bridge the gap, *i.e.* the 1100-cm^{-1} phonons. On the other hand, we assume that fast transitions happen, compared to the fluorescence lifetime, among the energy sub-levels in the upper and lower manifolds of Yb^{3+} such that only the lowest energy state in each manifold is occupied. For a transition between the lowest-energy states of the upper manifold and lower manifold in Yb^{3+}, we have $\Delta E = 10260$ cm^{-1} [105]. Thus, for $h\nu = 1100$ cm^{-1} we find $p = 9$ and , therefore, $(1-e^{-h\nu/kT})^{-p} = 1.15$ at room temperature, *i.e.* at $kT = 208$ cm^{-1}. For the silica host, it has been reported $B = 1.4\times10^{12}$ s^{-1} and $\alpha = 4.7\times10^{-3}$ cm [14] therefore from Eq. A.4 we find $1/\tau_{nr} = 1.8\times10^{-9}$ s^{-1}. This value is tremendously smaller than $1/\tau_r = 1000$ s^{-1} that is the nominal fluorescence decay rate of Yb^{3+} in silica fibers. As a result, the concentration quenching due to the multi-phonon relaxation process in Yb:fibers is negligible. This conclusion has been used in Chpt. 2.16 for casting the amplifier rate equations in Yb:fibers.

However, the nonradiative quenching becomes important for highly doped Yb:fibers due to formation of clustered ytterbium ions [14, 15, 101]. For example, the nonradiative decay rate $1/\tau_{nr}$ has been reported up to $170,000$ s^{-1} for the ytterbium concentration as high as 3.4×10^{27} m^{-3} in Yb:fibers [111]. When the ytterbium clusters are formed, chances are within the clusters, some of excited Yb^{3+} ions give up their energies to defect points and consequently the stored energy will be dissipated and also the Yb^{3+} upper state lifetime decreases [101]. The decreased Yb^{3+} upper state lifetime is realized from $1/\tau = 1/\tau_r + 1/\tau_{nr}$ where $1/\tau$ is the quenched upper state decay rate, $1/\tau_r$ is the radiative decay rate of the non-quenched Yb^{3+}, and $1/\tau_{nr}$ is the non-radiative decay rate of the quencher channel.

To avoid the formation of the ytterbium clustering, silica fiber is usually co-doped with other chemical elements to increase the level of solubility of Yb^{3+} in the silica host. On the other hand, the co-dopant element will affect on the absorption/emission cross section properties of Yb^{3+}. Therefore, there is a trade off between increasing the concentration of co-dopant elements and fluorescence properties of Yb:fibers.

Jetschke *et al* have reported 2.60×10^{26} m^{-3} for the ytterbium concentration with no sign of lifetime quenching for the co-doped Yb:fibers with phosphorus and aluminum [102]. The authors have observed that the fluorescence lifetime at 1020 nm decreases from 830 μs to 670 μs as the ytterbium concentration increased from 2.60×10^{26} m^{-3} to 4.86×10^{26} m^{-3} but for a ytterbium concentration below 2.60×10^{26} m^{-3}, there was no indication of significant changes in both fluorescence lifetime and fluorescence intensity.

In this thesis, the ytterbium concentration has been roughly 8×10^{25} m^{-3} in both single-clad and double-clad Yb:fibers. Furthermore, for the numerical modeling, the fluorescence lifetime τ of the ytterbium ions is assumed to be equal to the theoretical value of 800 μs and not effected by the concentration quenching effect.

Appendix B

Saturation power of the seed signal in the YDFA

From a laser amplifier, more power is usefully delivered to the output seed signal as the input average power increases. The figure of merit of the input seed power is saturation power [9]. Here, I have followed Ref. [14] to find an appropriate equation for the input seed saturation power in Yb:fibers from an analytical approach. Then, the equation will be used to calculate the numerical values of the input seed saturation power to the single-clad and double-clad Yb:fibers used in this thesis.

We assume that the ASE field does not build up in the beginning of the fiber noticeably. This simplifies Eq. 2.52 to

$$\begin{aligned}\frac{dN_2}{dt} = -\frac{N_2}{\tau} - \frac{\Gamma_p}{Ahc}\sum_i^{\text{Pump}} \lambda_i \left[(\sigma_e^i + \sigma_a^i)N_2 - \sigma_a^i N_t\right](uP_i^{p+} + vP_i^{p-}) \\ - \frac{\Gamma_s}{Ahc}\sum_j^{\text{Seed}} \lambda_j \left[(\sigma_e^j + \sigma_a^j)N_2 - \sigma_a^j N_t\right] P_j^s\,.\end{aligned} \tag{B.1}$$

We also assume that the pump laser and the seed signal are single wavelength laser sources at the wavelengths λ_p and λ_s respectively, therefore, the sum operators are removed from Eq. B.1. We also replace $uP_i^{p+} + vP_i^{p-}$ with P^p for a total pump power from both fiber ends. Furthermore, we assume that the system is in steady state. As soon as ytterbium

ions in Yb:fiber are irradiated by the pump and seed lasers, the upper state population density increases by absorbing the pump and seed photons and thereafter it decreases by the spontaneous emission and stimulated emission processes. This will continue until the rates of population and depopulation of the upper state become equal. At this time, the system is in the steady state regime, therefore $\frac{dN_2}{dt} = 0$. Using the above assumptions, Eq. B.1 is simplified to

$$-\frac{N_2}{\tau} - \left[(\sigma_e^p + \sigma_a^p)N_2 - \sigma_a^p N_t\right]\frac{\Gamma_p \lambda_p P_p}{Ahc} - \left[(\sigma_e^s + \sigma_a^s)N_2 - \sigma_a^s N_t\right]\frac{\Gamma_s \lambda_s P_s}{Ahc} = 0. \tag{B.2}$$

From Eq. B.2, N_2 is given by

$$N_2 = \frac{\frac{\Gamma_p \lambda_p \tau \sigma_a^p}{Ahc} P_p + \frac{\Gamma_s \lambda_s \tau \sigma_a^s}{Ahc} P_s}{1 + \frac{\Gamma_p \lambda_p \tau (\sigma_a^p + \sigma_e^p)}{Ahc} P_p + \frac{\Gamma_s \lambda_s \tau (\sigma_a^s + \sigma_e^s)}{Ahc} P_s} N_t. \tag{B.3}$$

From Eq. 2.59 and assuming the fiber attenuation is negligible in the beginning of the fiber, the propagation of the seed signal in the the fiber core is governed by

$$\frac{dP_s}{dz} = \Gamma_s \left[(\sigma_e^s + \sigma_a^s)N_2 - \sigma_a^s N_t\right] P_s. \tag{B.4}$$

From Eq. B.4, the saturation gain coefficient at the seed wavelength λ_s is written as

$$g = \Gamma_s \left[(\sigma_a^s + \sigma_e^s)N_2 - \sigma_a^s N_t\right]. \tag{B.5}$$

After substituting Eq. B.3 in Eq. B.5, the saturation gain coefficient is given by

$$g = \frac{\left[\frac{\Gamma_p \lambda_p \tau}{Ahc}\left(\frac{\sigma_e^s}{\sigma_a^s}\sigma_a^p - \sigma_e^p\right)P_p - 1\right]\Gamma_s \sigma_a^s N_t}{1 + \frac{\Gamma_p\, \lambda_p \tau (\sigma_a^p + \sigma_e^p)}{Ahc} P_p + \frac{\Gamma_s\, \lambda_s \tau (\sigma_a^s + \sigma_e^s)}{Ahc} P_s}. \tag{B.6}$$

From Eq. B.6, the threshold pump power is obtained for $g > 0$ and is given by

$$P_p^{th} = \frac{\frac{Ahc}{\Gamma_p \lambda_p \tau}}{\frac{\sigma_e^s}{\sigma_a^s}\sigma_a^p - \sigma_e^p}, \tag{B.7}$$

where P_p^{th} is the total threshold pump power. For Yb:fibers, the maximum absorption takes place at the wavelength 975 nm (see Fig. 2.1) where we have

$$\sigma_a^p = \sigma_e^p. \tag{B.8}$$

Using Eq. B.8, Eqs. B.7 is simplified to

$$P_p^{th} = \left(\frac{Ahc}{\Gamma_p \lambda_p \tau \sigma_a^p}\right) \frac{1}{\frac{\sigma_e^s}{\sigma_a^s} - 1}. \tag{B.9}$$

From Eq. B.6, the pump saturation power P_p^{sat} at the wavelength 975 nm is defined by

$$P_p^{sat} = \frac{Ahc}{2\Gamma_p \lambda_p \tau \sigma_a^p}, \tag{B.10}$$

Using Eqs. B.9 and B.10, Eq. B.6 is rewritten as

$$g = \frac{\left(\frac{P_p}{P_p^{th}} - 1\right) \Gamma_s \sigma_a^s N_t}{1 + \frac{P_p}{P_p^{sat}} + \frac{P_s}{P_{0,s}^{sat}}}, \tag{B.11}$$

where, $P_{0,s}^{sat}$ is zero-pump seed saturation power for $P_p = 0$ and is defined by

$$P_{0,s}^{sat} = \frac{Ahc}{\Gamma_s \lambda_s \tau (\sigma_a^s + \sigma_e^s)}. \tag{B.12}$$

Now, Eq. B.11 is written as

$$g = \frac{\left(\frac{P_p}{P_p^{th}} - 1\right) \Gamma_s \sigma_a^s N_t}{1 + \frac{P_p}{P_p^{sat}}} \frac{1}{1 + \frac{P_s}{P_{0,s}^{sat}(1 + \frac{P_p}{P_p^{sat}})}}. \tag{B.13}$$

The core area A for the single-clad Yb:fiber with a 4-μm core diameter is 1.26×10^{-11} m^2 and for the double-clad Yb:fiber with a 6-μm core diameter is 2.83×10^{-11} m^2. Using these values as well as Γ_p for the SC and DC Yb:fibers from Table 2.1 and invoking the emission and absorption cross sections of the seed signal from Fig. 2.6 and $\sigma_a^p = 2.6 \times 10^{-24}$ m^2 for $\lambda_p = 975$ nm, from Eq. B.9, the threshold pump power for the single-clad Yb:fiber pumped from both ends is 50 μW at 1035 nm and 2.2 μW at 1105 nm; for the single-clad Yb:fiber pumped from one end, these values are multiplied by 2 and the threshold pump power for the double-clad is 80 mW at 1035 nm and is 3.5 mW at 1105 nm. From Eq. B.10, the saturation pump power for the SC-YDFA pumped from one end is 0.744 mW and for the SC-YDFA pumped from both ends is 0.372 mW and for the DC-YDFA pumped from

one end is 603 mW. Therefore, the saturation pump power is larger than the threshold pump power approximately by one order of magnitude for the two types of the Yb:fiber.

In practice, the pump power is very large at the beginning of the fiber and it exceeds the saturation pump power. Thus, with a pump power $P_p \gg P_p^{sat}$, the seed saturation gain coefficient given by Eq. B.13 after some algebra is simplified to

$$g = \frac{\frac{\Gamma_s N_t}{2}(\sigma_e^s - \sigma_a^s)}{1 + \frac{P_s}{P_{0,s}^{sat}(1+\frac{P_p}{P_p^{sat}})}} = \frac{g_{ss}}{1 + \frac{P_s}{P_{0,s}^{sat}(1+\frac{P_p}{P_p^{sat}})}}. \tag{B.14}$$

The seed saturation power is defined as the seed power that the gain coefficient g drops to half of the small signal gain coefficient g_{ss}. Thus, from Eq. B.14, the seed saturation power is given by

$$P_s^{sat} = P_{0,s}^{sat}(1 + \frac{P_p}{P_p^{sat}}). \tag{B.15}$$

Using Eq. B.12, Fig. B.1 depicts $P_{0,s}^{sat}$ as a function of wavelength for the single-clad and double-clad Yb:fibers used in this thesis. As can be seen the minimum saturation power takes place at the wavelengths close to 1030 nm. From this figure, the saturation power $P_{0,s}^{sat}$ for the SC-YDFA is 6 mW at 1035 nm and 23 mW at 1105 nm and for the DC-YDFA is 14 mW at 1035 nm and 51 mW at 1105 nm.

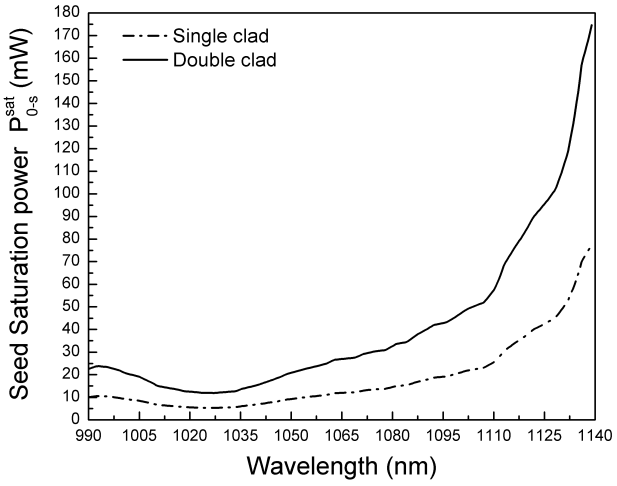

Figure B.1: The zero-pump seed saturation power $P_{0,sat}$ in the Yb:fibers.

Table B.1: Zero-pump seed saturation power $P_{0,sat}$ at the selective seed wavelengths 1035, 1041, 1103, and 1105 nm for the single-clad and double-clad Yb:fibers used in this thesis.

	1035 nm	1041 nm	1103 nm	1105 nm
(Single-clad YDFA); $P_{0,sat}$ (mW)	6	7	22	23
(Double-clad YDFA); $P_{0,sat}$ (mW)	14	16	50	51

From Eq. B.14, the seed saturation power P_s^{sat} in the presence of pump laser increases linearly with the pump power. Recalling the pump saturation power, P_p^{sat} for the SC-YDFA is 0.744 mW and for the DC-YDFA is 0.6 W, thus, the seed saturation power P_s^{sat} increases by a factor of 337 for the SC-YDFA with a launched pump power of 250 mW and by a factor of 7 for the DC-YDFA with a launched pump power of 3.6 W. The increased seed saturation powers are valid for a constant pump power, however, the pump power decreases from both absorption process and from the amplification process of the seed signal. Therefore, as the pump power decreases, the seed saturation power decreases to the $P_{0,s}^{sat}$. This will happen in the beginning of the Yb:fibers. Thus, the $P_{0,s}^{sat}$ is a good estimate for the seed saturation power in the YDFA's for pumping with the 975-nm laser diodes due to the large pump absorption.

Table B.1 summarizes the zero-pump seed saturation power $P_{0,sat}$ at the selective seed wavelengths 1035, 1041, 1103, and 1105 nm for the single-clad and double-clad Yb:fibers used in this thesis. From this table, the seed saturation power to the main amplifier is 16 mW at 1041 nm and is 50 mW at 1103 nm. From experimental results, these seed powers have been found to extract power efficiently from the main amplifier with a suppressed ASE at the output.

List of publications

Peer-reviewed publications

1. **M. Hajialamdari**, A. M. Alkadry, and D. Strickland. Modeling of a two-color, two-stage, ultafast Yb-doped fiber amplifier. *Opt. Commun.*, **284**, 2843, 2011.

2. **M. Hajialamdari** and D. Strickland. Tunable mid-infrared source from an ultrafast two-color Yb:fiber chirped-pulse amplifier. *Opt. Lett.*, **37**, 3570, 2012.

Conference papers

1. **M. Hajialamdari** and D. Strickland. Two-color Yb:fiber chirped pulse amplifier for tunable difference-frequency-based mid-infrared generation. *Paper CIPI-LAS & APP-8-49-2 presented at Photonic North Conference, Montreal*, 2012.

2. **M. Hajialamdari** and D. Strickland. A tunable mid-infrared (16-20 μm) source from a two-color Yb:fiber chirped pulse amplifier. *Paper CTU2M.1 presented at Conference on Lasers and Electro-Optics (CLEO), San Jose*, 2012.

3. M. Al-Kadry, **M. Hajialamdari**, and D. Strickland. 0.4 mW average power at 17.5 microns from frequency mixing of two-color fiber chirped pulse amplifier. *Paper CThD3 presented at Conference on Lasers and Electro-Optics (CLEO), Baltimore*, 2011.

4. **M. Hajialamdari**, A. M. Al-Kadry, and D. Strickland. Two-color fiber chirped pulse amplifier for mid-infrared generation. *Paper FLA-16-2-2 presented at Photonics North, Ottawa*, 2011.

5. **M. Hajialamdari**, A. M. Al-Kadry, and D. Strickland. Two-color fiber chirped pulse amplifier for mid-infrared generation. *Paper FThG1 presented at Frontiers in Optics (FIO), Rochester*, 2010.

Copyright permissions

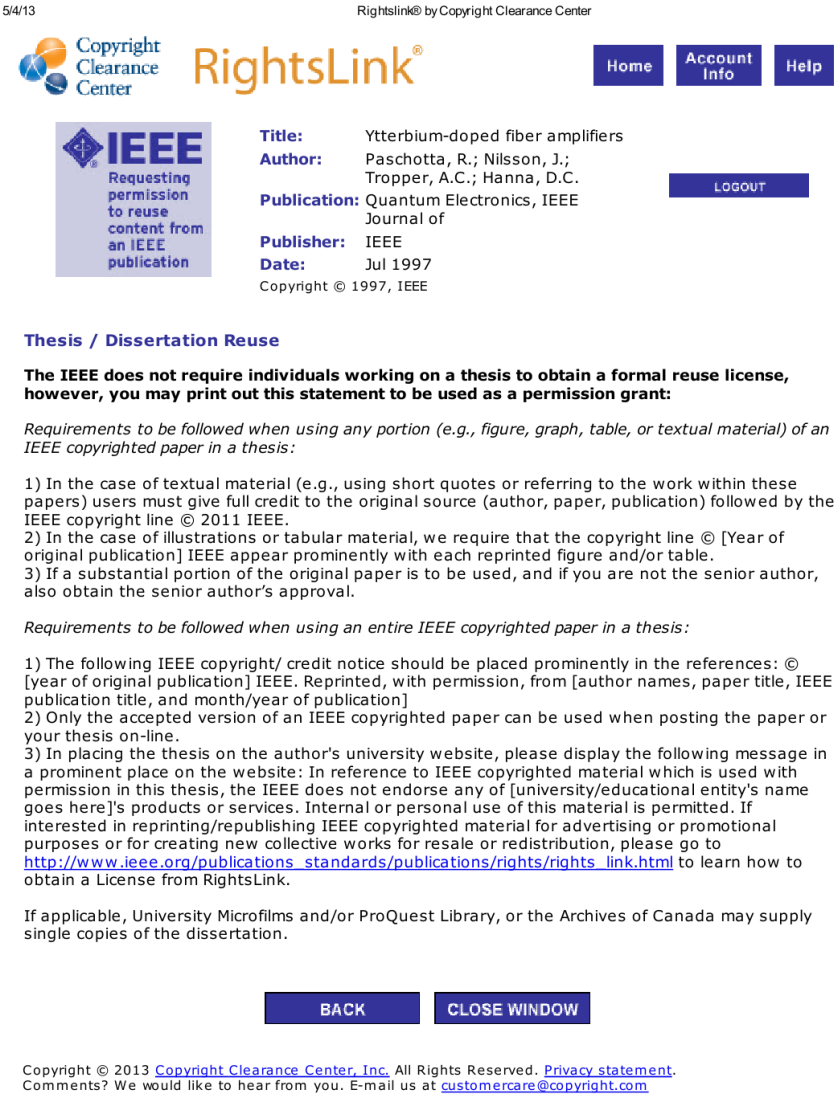

5/4/13 Rightslink® by Copyright Clearance Center

Copyright Clearance Center RightsLink®

Home | Account Info | Help

IEEE Requesting permission to reuse content from an IEEE publication

Title: Ytterbium-doped fiber amplifiers
Author: Paschotta, R.; Nilsson, J.; Tropper, A.C.; Hanna, D.C.
Publication: Quantum Electronics, IEEE Journal of
Publisher: IEEE
Date: Jul 1997
Copyright © 1997, IEEE

LOGOUT

Thesis / Dissertation Reuse

The IEEE does not require individuals working on a thesis to obtain a formal reuse license, however, you may print out this statement to be used as a permission grant:

Requirements to be followed when using any portion (e.g., figure, graph, table, or textual material) of an IEEE copyrighted paper in a thesis:

1) In the case of textual material (e.g., using short quotes or referring to the work within these papers) users must give full credit to the original source (author, paper, publication) followed by the IEEE copyright line © 2011 IEEE.
2) In the case of illustrations or tabular material, we require that the copyright line © [Year of original publication] IEEE appear prominently with each reprinted figure and/or table.
3) If a substantial portion of the original paper is to be used, and if you are not the senior author, also obtain the senior author's approval.

Requirements to be followed when using an entire IEEE copyrighted paper in a thesis:

1) The following IEEE copyright/ credit notice should be placed prominently in the references: © [year of original publication] IEEE. Reprinted, with permission, from [author names, paper title, IEEE publication title, and month/year of publication]
2) Only the accepted version of an IEEE copyrighted paper can be used when posting the paper or your thesis on-line.
3) In placing the thesis on the author's university website, please display the following message in a prominent place on the website: In reference to IEEE copyrighted material which is used with permission in this thesis, the IEEE does not endorse any of [university/educational entity's name goes here]'s products or services. Internal or personal use of this material is permitted. If interested in reprinting/republishing IEEE copyrighted material for advertising or promotional purposes or for creating new collective works for resale or redistribution, please go to http://www.ieee.org/publications_standards/publications/rights/rights_link.html to learn how to obtain a License from RightsLink.

If applicable, University Microfilms and/or ProQuest Library, or the Archives of Canada may supply single copies of the dissertation.

BACK | CLOSE WINDOW

Copyright © 2013 Copyright Clearance Center, Inc. All Rights Reserved. Privacy statement.
Comments? We would like to hear from you. E-mail us at customercare@copyright.com

Copyright permission to republish the experimental emission and absorption cross sections of the Yb-doped silica fibers in Figs. 2.1 and 2.6.

My Orders My Library My Profile Welcome mojtaba248@yahoo.ca Log out | Help

My Orders > Orders > All Orders

License Details

This is a License Agreement between Mojtaba Hajialamdari ("You") and Elsevier ("Elsevier"). The license consists of your order details, the terms and conditions provided by Elsevier, and the payment terms and conditions.

Get the printable license.

License Number	[redacted]
License date	Jun 11, 2013
Licensed content publisher	Elsevier
Licensed content publication	Optics Communications
Licensed content title	Modeling of a two-color, two-stage, ultrafast Yb-doped fiber amplifier
Licensed content author	M. Hajialamdari,A.M. Alkadry,D. Strickland
Licensed content date	1 June 2011
Licensed content volume number	284
Licensed content issue number	12
Number of pages	6
Type of Use	reuse in a thesis/dissertation
Portion	full article
Format	both print and electronic
Are you the author of this Elsevier article?	Yes
Will you be translating?	No
Order reference number	None
Title of your thesis/dissertation	Tunable Two-Color Ultrafast Yb:Fiber Chirped Pulse Amplifier Modeling, Experiment, and Application in Mid-Infrared Generation
Expected completion date	Aug 2013
Elsevier VAT number	GB 494 6272 12
Permissions price	0.00 USD
VAT/Local Sales Tax	0.00 USD
Total	**0.00 USD**

Back

Copyright permission to reuse the materials in publication [93].

Copyright permission to reuse the materials in publication [96].

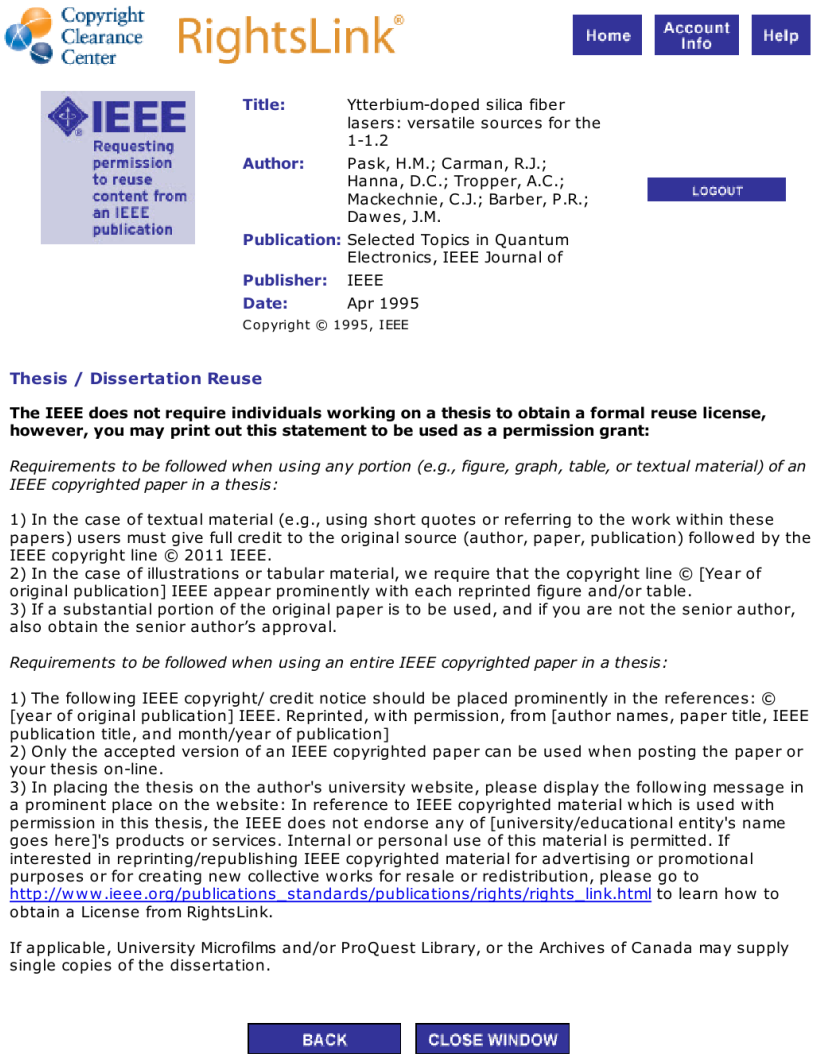

Copyright Clearance Center RightsLink®

Home | Account Info | Help

IEEE Requesting permission to reuse content from an IEEE publication

Title: Ytterbium-doped silica fiber lasers: versatile sources for the 1-1.2

Author: Pask, H.M.; Carman, R.J.; Hanna, D.C.; Tropper, A.C.; Mackechnie, C.J.; Barber, P.R.; Dawes, J.M.

Publication: Selected Topics in Quantum Electronics, IEEE Journal of

Publisher: IEEE

Date: Apr 1995

Copyright © 1995, IEEE

LOGOUT

Thesis / Dissertation Reuse

The IEEE does not require individuals working on a thesis to obtain a formal reuse license, however, you may print out this statement to be used as a permission grant:

Requirements to be followed when using any portion (e.g., figure, graph, table, or textual material) of an IEEE copyrighted paper in a thesis:

1) In the case of textual material (e.g., using short quotes or referring to the work within these papers) users must give full credit to the original source (author, paper, publication) followed by the IEEE copyright line © 2011 IEEE.
2) In the case of illustrations or tabular material, we require that the copyright line © [Year of original publication] IEEE appear prominently with each reprinted figure and/or table.
3) If a substantial portion of the original paper is to be used, and if you are not the senior author, also obtain the senior author's approval.

Requirements to be followed when using an entire IEEE copyrighted paper in a thesis:

1) The following IEEE copyright/ credit notice should be placed prominently in the references: © [year of original publication] IEEE. Reprinted, with permission, from [author names, paper title, IEEE publication title, and month/year of publication]
2) Only the accepted version of an IEEE copyrighted paper can be used when posting the paper or your thesis on-line.
3) In placing the thesis on the author's university website, please display the following message in a prominent place on the website: In reference to IEEE copyrighted material which is used with permission in this thesis, the IEEE does not endorse any of [university/educational entity's name goes here]'s products or services. Internal or personal use of this material is permitted. If interested in reprinting/republishing IEEE copyrighted material for advertising or promotional purposes or for creating new collective works for resale or redistribution, please go to http://www.ieee.org/publications_standards/publications/rights/rights_link.html to learn how to obtain a License from RightsLink.

If applicable, University Microfilms and/or ProQuest Library, or the Archives of Canada may supply single copies of the dissertation.

BACK | CLOSE WINDOW

Copyright permission to republish Fig. A.1.

References

[1] A. Gambetta, G. Galzerano, A. G. Rozhin, A. C. Ferrari, R. Ramponi, P. Laporta, and M. Marangoni. Sub-100 fs two-color pump-probe spectroscopy of single wall carbon nanotubes with a 100 MHz Er-fiber laser system. *Opt. Express*, 16:11727, 2008. 2, 5

[2] X. Zhao, Z. Zheng, L. Liu, Q. Wang, H. Chen, and J. Liu. Fast, long-scan-range pump-probe measurement based on asynchronous sampling using a dual-wavelength mode-locked fiber laser. *Opt. Express*, 20:25584, 2012. 2, 5

[3] S. T. Cundiff, J. Ye, and J. L. Hall. Optical frequency synthesis based on mode-locked lasers. *Rev. Sci. Instrum.*, 27:3749, 2001. 2, 5

[4] T. Udem, R. Holzwarth, and T. W. Hänsch. Optical frequency metrology. *Nature*, 416:233, 2002. 2, 5

[5] H.-B. Liu and X.-C. Zhang. *Terahertz Spectroscopy for Explosive, Pharmaceutical, and Biological Sensing Applications:Terahertz Frequency Detection and Identification of Materials and Objects*. R. E. Miles and X. C. Zhang and H. Eisele and A. Krotkus, eds. Springer, 2007. 2

[6] J. Wilkinson, C. T. Konek, J. S. Moran, E. M. Witko, and T. M. Korter. Terahertz absorption spectrum of triacetone triperoxide (TATP). *Chem. Phys. Lett.*, 478:172, 2009. 2

[7] T. H. Maiman. Stimulated optical radiation in ruby. *Nature*, 187:493, 1960. 4

[8] A. Javan, W. R. Bennett, Jr., and D. R. Herriott. Population inversion and continuous optical maser oscillation in a gas discharge containing a He-Ne mixture. *Phys. Rev. Lett.*, 6:106, 1961. 4

[9] W. Koechner. *Solid State Laser Engineering*. Springer, 2006. 5, 9, 10, 12, 48, 128

[10] C. Fischer and M. W. Sigrist. *Solid-State Mid-Infrared Laser Sources: Mid-IR Difference Frequency Generation*. I. T. Sorokina and K. L. Vodoppyanov, eds. Springer, 2003. 5

[11] H. W. Etzel, H. W. Gandy, and R. J. Ginther. Stimulated emission of infrared radiation from ytterbium activated silicate glass. *Appl. Opt.*, 1:534, 1962. 5

[12] D. C. Hanna, R. M. Percival, I. R. Perry, R. G. Smart, P. J. Suni, J. E. Townsend, and A. C. Tropper. Continuous-wave oscillation of a monomode ytterbium-doped fibre laser. *Electron. Lett.*, 24:1111, 1988. 5

[13] R. Paschotta, J. Nilsson, A. C. Tropper, and D. C. Hanna. Ytterbium-doped fiber amplifiers. *IEEE J. Quantum. Electron.*, 33:1049, 1997. 5, 6, 33, 34, 62

[14] P. C. Becker, N. A. Olsson, and J. R. Simpson. *Erbium-Doped Fiber Amplifiers: Fundamental and Technology*. Academic Press, San Diego, first edition, 1999. 5, 29, 30, 31, 33, 34, 35, 37, 39, 121, 122, 126, 127, 128

[15] M. J. F. Digonnet. *Rare-Earth-Doped Fiber Lasers and Amplifiers*. Marcel Dekker Inc., New York, second edition, 2001. 5, 121, 122, 124, 126, 127

[16] F. Ö. Ilday, J. Buckley, L. Kuznetsova, and F. W. Wise. Generation of 36-femtosecond pulses from a ytterbium fiber laser. *Opt. Express*, 11:3550, 2003. 5

[17] J. R. Buckley, S. W. Clark, and F. W. Wise. Generation of ten-cycle pulses from an ytterbium fiber laser with cubic phase compensation. *Opt. Lett.*, 31:1340, 2006. 5

[18] X. Zhou, D. Yoshitomi, Y. Kobayashi, and K. Torizuka. Generation of 28-fs pulses from a mode-locked ytterbium fiber oscillator. *Opt. Express*, 16:7055, 2008. 5

[19] L. A. Gomes, L. Orsila, T. Jouhti, and O. G. Okhotnikov. Picosecond SESAM-based ytterbium mode-loced fiber lasers. *IEEE J. Sel. Topics in Quantum Electron.*, 10:129, 2004. 5

[20] D. C. Hanna, R. M. Percival, I. R. Perry, R. G. Smart, P.J. Sun, and A. C. Tropper. An ytterbium-doped monomode fiber laser: broadly tunable operation from 1.010 to 1.162 μm and three-level operation at 974 nm. *J. Mod. Opt.*, 37:192, 1990. 5, 6

[21] J. K. Sahu, C. C. Renaud, K. Furusawa, R. Selvas, J. A. Alvarez-Chavez, D. J. Richardson, and J. Nilsson. Jacketed air-clad cladding pumped ytterbium-doped.fibre laser with wide turning range. *Electron. Lett.*, 37:1116, 2001. 5, 6

[22] F. Röser, J. Rothhard, B. Ortac, A. Liem, O. Schmidt, T. Schreiber, , J. Limpert, and A. Tünnermann. 131 W 220 fs fiber laser system. *Opt. Lett.*, 30:2754, 2005. 6, 88

[23] T. Eidam, S. Hadrich, Fabian Röser, E. Seise, T. Gottschall, J. Rothhardt, Thomas Schreiber, J. Limpert, and A. Tünnermann. A 325-W-average-power fiber CPA system delivering sub-400 fs pulses. *IEEE J. Sel. Topics in Quantum Electron.*, 15:187, 2009. 6

[24] T. Eidam, S. Hanf, E. Seise, T. V. Andersen, T. Gabler, C. Wirth, T. Schreiber, J. Limpert, and A. Tünnermann. Femtosecond fiber CPA system smitting 830 W average output power. *Opt. Lett.*, 35:94, 2010. 6, 61

[25] Y. Jeong, A. J. Boyland, J. K. Sahu, S. Chung, J. Nilsson, and D. N. Payne. Multi-kilowatt single-mode ytterbium-doped large-core fiber laser. *J. Opt. Soc. Korea*, 13:416, 2009. 6

[26] E. Stiles. New developments in IPG fiber laser technology. In *in Proceedings of the 5th International Workshop on Fiber*, 2009. 6

[27] J. Limpert, Fabian Röser, T. Schreiber, and A. Tünnermann. High-power ultrafast fiber laser systems. *IEEE J. Sel. Topics in Quantum Electron.*, 12:233, 2006. 6, 7

[28] D. J. Richardson, J. Nilsson, and W. A. Clarkson. High power fiber lasers: current status and future perspectives invited. *J. Opt. Soc. Am. B*, 27:B63, 2010. 6

[29] A. Tünnermann, T. Schreiber, and J. Limpert. Fiber lasers and amplifiers: an ultrafast performance evolution. *Appl. Opt.*, 49:F71, 2010. 6, 7

[30] J. Nilsson and D. N. Payne. High-power fiber lasers. *Science*, 332:921, 2011. 6

[31] G. P. Agrawal. *Fiber Optic Communication Systems*. Academic Press, 2001. 6, 100

[32] S. Jetschke, S. Unger, A. Schwuchow, M. Leich, and J. Kirchhof. Efficient Yb laser fibers with low photodarkening by optimization of the core composition. *Opt. Express*, 16:15540, 2008. 6

[33] Y. Wang. Heat dissipation in kilowatt fiber power amplifiers. *IEEE J. Quantum. Electron.*, 40:731, 2004. 6, 47

[34] Y. Wang, C.-Q. Xu, and H. Po. Thermal effects in kilowatt fiber lasers. *IEEE Photonic. Tech. L.*, 16:63, 2004. 6, 47

[35] Y. Fan, B. He, J. Zhou, J. Zheng, H. Liu, Y. Wei, J. Dong, and Q. Lou. Thermal effects in kilowatt all-fiber MOPA. *Opt. Express*, 19:15162, 2011. 6

[36] M. K. Davis, M. J. F. Digonnet, and R. H. Pantell. Thermal effects in doped fibers. *J. Lightwave Tech.*, 16:1013, 1998. 6

[37] D. Liu, J. Song, and D. Strickland. Dual-wavelength, ultrashort, Yb:fiber amplifier. *Proc. SPIE*, 5579:744, 2004. 7, 27

[38] R. Romero-Alvarez, Z. Wu R. Pettus, and D. Strickland. Two-color fiber amplifier for short-pulse, mid-infrared generation. *Opt. Lett.*, 33:1065–1067, 2008. 7, 15, 17, 18, 27, 88

[39] A. M. Al-kadry and D. Strickland. Generation of 400 μw at 17.5 μm using a two-color Yb fiber chirped pulse amplifier. *Opt. Lett.*, 36:1080, 2011. 7, 8, 15, 17, 18, 27, 61, 88, 89, 90, 91, 93, 102

[40] A. J. Budz, J. Waisman, H. F. Tiedje, and H. K. Haugen. Short-pulse dual-wavelength system based on mode-locked diode lasers with a single polarization-maintaining Yb:fiber amplifier. *J. Lightwave Tech.*, 27:3416, 2009. 7, 8, 37, 40, 42, 47, 50, 65, 88

[41] Y. Bai, W. Xiang, P. Zu, and G. Zhang. Tunable dual-wavelength passively mode-locked Yb-doped fiber laser using SESAM. *Chin. Opt. Lett.*, 10:111405, 2012. 7, 8

[42] O. G. Okhotnikov, L. Gomes, N. Xiang, T. Jouhti, and A. B. Grudinin. Mode-locked ytterbium fiber laser tunable in the 9801070-nm spectral range. *Opt. Lett.*, 28:1522, 2003. 8

[43] P. F. Moulton. Spectroscopic and laser characteristics of Ti:Al_2O_3. *J. Opt. Soc. Am. B*, 3:125, 1986. 9

[44] U. Morgner, F. X. Kartner, S. H. Cho, Y. Chen, H. A. Haus, J. G. Fujimoto, E. P. Ippen, V. Scheuer, G. Angelow, and T. Tschudi. Sub-two-cycle pulses from a Kerr-lens mode-locked Ti:sapphire laser. *Opt. Lett.*, 24:411, 1999. 9

[45] D. H. Sutter, G. Steinmeyer, L. Gallmann, N. Matuschek, F. Morier-Genoud, U. Keller, V. Scheuer, G. Angelow, and T. Tschudi. Semiconductor saturable-absorber mirrorassisted Kerr-lens mode-locked Ti:sapphire laser producing pulses in the two-cycle regime. *Opt. Lett.*, 24:631, 1999. 9

[46] M. R. X. de Barros and P. C. Becker. Two-color synchronously mode-locked femtosecond Ti:sapphire laser. *Opt. Lett.*, 18:631, 1993. 9, 10

[47] D. R. Dykaar and S. B. Darack. Sticky pulses: two-color cross-mode-locked femtosecond operation of a single Ti:sapphire laser. *Opt. Lett.*, 18:634, 1993. 9, 10, 11

[48] J. M. Evans, D. E. Spence, D. Burns, and W. Sibbett. Dual-wavelength self-mode-locked Ti:sapphire laser. *Opt. Lett.*, 18:1074, 1993. 9, 10, 11

[49] A. Leitenstorfer, C. Fürst, and A. Laubereau. Widely tunable two-color mode-locked Ti:sapphire laser with pulse jitter of less than 2 fs. *Opt. Lett.*, 20:916, 1995. 9, 10, 11

[50] Z. Zhang, A. M. Deslauriers, and D. Strickland. Dual-wavelength chirped-pulse amplification system. *Opt. Lett.*, 25:581, 2000. 9, 12

[51] J. F. Xia, J. Song, and D. Strickland. Development of a dual-wavelength Ti:sapphire multi-pass amplifier and its application to intense mid-infrared generation. *Opt. Commun.*, 206:149, 2002. 9, 12, 13

[52] J. M. Fraser, I. W. Cheung, F. Légaré, D. M. Villeneuve, J. P. Likforman, M. Joffre, and P. B. Corkum. High-energy sub-picosecond pulse generation from 3 to 20 μm. *Appl. Phys. B*, 74:S153, 2002. 9, 11, 12, 15, 17, 18, 61

[53] K. Yamakawa and C. P. J. Barty. Two-color chirped-pulse amplification in an ultrabroadband Ti:sapphire ring regenerative amplifier. *Opt. Lett.*, 28:2402, 2003. 9, 11, 12, 13, 61

[54] K. Asakawa and A. Assion *et al. Springer Handbook of Lasers and Optics*. Springer, 2012. 10

[55] D. Strickland and G. Mourou. Compression of amplified chirped optical pulses. *Opt. Commun.*, 55:447, 1985. 13, 22

[56] K. Yamakawa and C. P. J. Barty. Ultrafast, ultrahigh-peak, and high-average power Ti:sapphire laser system and its applications. *IEEE J. Sel. Top. Quant. Electron.*, 6:658, 2000. 13, 14

[57] A. Rundquist, C. Durfee, Z. Chang, G. Taft, E. Zeek, S. Backus, M. M. Murnane, H. C. Kapteyn, I. Christov, and V. Stoev. Ultrafast laser and amplifier sources. *Appl. Phys. B*, 65:161, 1997. 13

[58] G. K. Samantaa, S. Chaitanya Kumar, K. Devi, and M. Ebrahim-Zadeh. High-power continuous-wave Ti:sapphire laser pumped by fiber-laser green source at 532 nm. *Opt. Laser Eng.*, 50:215, 2012. 13

[59] J. Squier, G. Korn, G. Mourou, G. Vaillancourt, and M. Bouvier. Amplification of femtosecond pulses at 10-KHz repetition rate in Ti:Al_2o_3. *Optics Letters*, 18:625, 1993. 14

[60] I. Matsushima, H. Yashiro, and T. Tomie. 10 KHz 40 W Ti:sapphire regenerative ring amplifier. *Opt. Lett.*, 31:2066, 2006. 14

[61] R. Boyd. *Nonlinear Optics*. Elsevier, 2008. 14, 15, 16, 26, 100, 102, 110

[62] G. B. Abdullaev, L. A. Kulevskii, A. M. Prokhorov, A. D. Savelev, E. Yu. Salaev, and V. V. Smirnov. Gase, a new effective material for nonlinear optics. *JETP Lett.*, 16:90, 1972. 15, 16

[63] V. G. Dmitriev, G. G. Gurzadyan, and D. N. Nikogosyan. *Handbook of Nonlinear Optical Crystals*. Springer, 1999. 15, 16, 102, 103, 112

[64] R. A. Kaindl, D. C. Smith, M. Joschko, M. P. Hasselbeck, M. Woerner, and T. Elsaesser. Femtosecond infrared pulses tunable from 9 to 18 μm at an 88-MHz repetition rate. *Opt. Lett.*, 23:861, 1998. 15, 17, 18

[65] S. Ehret and H. Schneider. Generation of subpicosecond infrared pulses tunable between 5:2 μm and 18 μm at a repetition rate of 76 MHz. *Appl. Phys. B*, 66:27, 1998. 15, 17, 19, 61

[66] K. L. Vodopyanov. Mid-infrared optical parametric generator with extra-wide (319 μm) tunability: applications for spectroscopy of two-dimensional electrons in quantum wells. *J. Opt. Soc. Am. B*, 16:1579, 1999. 15, 20

[67] J. M. Fraser, D. Wang, A. Hache, G. R. Allan, and H. M. van Driel. Generation of high-repetition-rate femtosecond pulses from 8 to 18 μm. *Appl. Opt.*, 36:5044, 1997. 17, 19

[68] M. H. Dunn and M. Ebrahimzadeh. Parametric generation of tunable light from continuous-wave to femtosecond pulses. *Science*, 286:1513, 1999. 19, 113

[69] G. Cerullo and S. De Silvestri. Ultrafast optical parametric amplifiers. *Rev. Sci. Instrum.*, 74:1, 2003. 19, 20

[70] M. Zimmermann, C. Gohle, R. Holzwarth, T. Udem, and T. W. Hänsch. Optical clockwork with an offset-free difference-frequency comb: accuracy of sum- and difference-frequency generation. *Opt. Lett.*, 29:310, 2004. 19

[71] K. L. Vodopyanov, G. M. H. Knippels, A. F. G. van der Meer, J. P. Maffetone, and I. Zwieback. Optical parametric generation in CGA crystal. *Opt. Commun.*, 202:205, 2002. 20

[72] K. L. Vodopyanov, S. B. Mirov, V. G. Voevodin, and P. G. Schunemann. Two-photon absorption in GaSe and $CdGeAs_2$. *Opt. Commun.*, 155:47, 1998. 20, 112

[73] F. Rotermund and V. Petrov. Mercury thiogallate mid-infrared femtosecond optical parametric generator pumped at 1.25 μm by a Cr:forsterite regenerative amplifier. *Opt. Lett.*, 25:746, 2000. 20

[74] J. Faist, F. Capasso, D. L. Sivco, A. L. Hutchinson, and A. Y. Cho. Quantum cascade laser. *Sceince*, 264:553, 1994. 21

[75] F. Capasso. High-performance midinfrared quantum cascade lasers. *Opt. Eng.*, 49(11):111102–1, 2010. 21

[76] J. Faist. *Quantum cascade lasers*. Oxford University Press, 2013. 21

[77] Y. Yao, A. J. Hoffman, and C. F. Gmachl. Mid-infrared quantum cascade lasers. *Nature Photon.*, 6:432, 2012. 21

[78] A. Hugi, R. Terazzi, Y. Bonetti, A. Wittmann, M. Fischer, M. Beck, J. Faist, and E. Gini. External cavity quantum cascade laser tunable from 7.6 μm to 11.4 μm. *Appl. Phys. Lett.*, 95:061103–1, 2009. 21

[79] C. Y. Wang, L. Kuznetsova, V. M. Gkortsas, L. Diehl, F. X. Kärtner, M. A. Belkin, A. Belyanin, X. Li, D. Ham, H. Schneider, P. Grant, C. Y. Song, S. Haffouz, Z. R. Wasilewski, H. C. Liu, and F. Capasso. Mode-locked pulses from mid-infrared quantum cascade lasers. *Opt. Express*, 17:12929, 2009. 22

[80] R. L. Fork, E. Martinez, and J. P. Gordon. Negative dispersion using pairs of prisms. *Opt. Lett.*, 9:150, 1984. 22

[81] O. E. Martinez. 3000 times grating compressor with positive group velocity dispersion: Application to fiber compensation in 1.3-1.6 μm region. *IEEE J. Quantum. Electron.*, QE-23:59, 1987. 22, 25

[82] E. B. Treacy. Optical pulse compression with diffraction gratings. *IEEE J. Quantum. Electron.*, QE-5:454, 1969. 23, 26

[83] J. C. Diels and W. Rudolph. *Ultrashort laser pulse phenonmena, fundamentals, techniques, and applications on a femtosecond time scale*. Els, 2006. 23, 24

[84] A. Yariv and P. Yeh. *Optical Electronics in Modern Communications*. Oxford University Press, 2007. 24, 25, 28, 43, 44, 98, 113

[85] O. Svelto. *Principle of Lasers*. Springer, 2010. 25, 26, 109

[86] M. Ebrahim-Zadeh and I. T. Sorokina. *Mid-Infrared Coherent Sources and Applications*. Springer, 2008. 26

[87] J. M. Dudley, G. Genty, and S. Coen. Supercontinuum generation in photonic crystal fiber. *Rev. Mod. Phys.*, 78:1135, 2006. 27

[88] F. Druon and P. Georges. Pulse-compression down to 20 fs using a photonic crystal fiber seeded by a diode-pumped Yb:SYS laser at 1070 nm. *Opt. Express*, 12:3383, 2004. 27

[89] D. E. McCumber. Einstion relations connecting broadband emission and absorption spectra. *Phys. Rev.*, 136:954, 1964. 31, 33

[90] X. Zou and H. Toratani. Evaluation of spectroscopic properties of Yb^{3+} -doped glasses. *Phys. Rev. B*, 52:15889, 1995. 33

[91] P. W. Millonni and J. H. Eberely. *Laser Physics*. John Wiely & Sons, 2010. 35, 41, 101

[92] I. H. Malitson. Interspecimen comparison of the refractive index of fused silica. *J. Opt. Soc. Am*, 55:1205, 1965. 35

[93] M. Hajialamdari, A. M. Alkadry, and D. Strickland. Modeling of a two-color, two-stage, ultrafast Yb-doped fiber amplifier. *Opt. Commun.*, 284:2843, 2011. 37, 40, 42, 70, 137

[94] J. T. Verdeyen. *Laser Electronics*. Prentice Hall, 1995. 41

[95] I. Kelson and A. Hardy. Optimization of strongly pumped fiber lasers. *J. Lightwave Tech.*, 17:791, 1999. 47

[96] M. Hajialamdari and D. Strickland. Tunable mid-infrared source from an ultrafast two-color Yb:fiber chirped-pulse amplifier. *Opt. Lett.*, 37:3570, 2012. 76, 77, 85, 114, 138

[97] K. L. Vodopyanov and L. A. Kulevskii. New dispersion relationships for gase in the 0.65-18 μm spectral region. *Opt. Commun.*, 115:357, 1995. 102, 104

[98] Y. J. Ding W. Shi, X. Mu, and N. Fernelius. Tunable and coherent nanosecond radiation in the range of 2.728.7 μm based on difference-frequency generation in gallium selenide. *Appl. Phys. Lett.*, 80:3889, 2002. 103

[99] G. R. Fowels. *Introduction to Modern Optics*. Dover Publications, 1989. 107, 125, 126

[100] Q. D. Boyd, A. Ashkin, J. M. Dziedzic, and D. A. Kleinman. Second-harmonic generation of light with double refraction. *Phys. Rev.*, 137(4A):A1305, 1965. 111

[101] R. Paschotta, J. Nilsson, P. R. Barber, J. E. Caplen, A. C. Tropper, and D.C. Hanna. Lifetime quenching in Yb-doped fibres. *Opt. Commun.*, 136:375, 1997. 121, 127

[102] S. Jetschke, S. Unger, U. Ropke, and J. Kirchhof. Photodarkening in Yb doped fibers: experimental evidence of equilibrium states depending on the pump power. *Opt. Express*, 14:14838, 2007. 121, 127

[103] C. E. Housecroft and A. G. Sharpe. *Inorganic Chemistry*. Pearson Education, 2005. 122

[104] R. Pappalardo and D. L. Wood. Spectrum of Yb^{3+} in yttrium gallium garnet. *J. Chem. Phys.*, 33:1734, 1960. 123

[105] H. M. Pask, R. J. Carman, D. C. Hannna, A. C. Tropper, C. J. Mackechnie, P. R. Barber, and J. M. Dawes. Ytterbium-doped silica fiber lasers: Versatile sources for the 1-1.2 μm. *IEEE J. Sel. Top. Quant. Electron.*, 1:2, 1995. 123, 126

[106] L. A. Riseberg and H. W. Moos. Multiphonon orbit-lattice relaxation of excited states of rare-earth ions in crystals. *Phys. Rev.*, 174:429, 1968. 125, 126

[107] C. B. Layne, W. H. Lowdermilk, and M. J. Weber. Multiphonon relaxation of rare-earth ions in oxide glasses. *Phys. Rev. B*, 16:10, 1977. 125, 126

[108] M. Cardona and G. Guntherodt. *Light Scattering in Solids II*. Springer, 1982. 126

[109] M. Hajialamdari. Crystal Growth , Raman Scattering and Optical Properties of the Superconductor $Cd_2Re_2O_7$ (^{16}O, ^{18}O). Master's thesis, Brock University, 2008. 126

[110] A. S. Kurkov and E. M. Dianov. Moderate-powers cw fibre lasers. *Quantum Electron.*, 34:881, 2004. 126

[111] Z. Burshtein, Y. Kalisky, S. Z. Levy, P. Le Boulanger, and S. Rotman. Impurity local phonon nonradiative quenching of Yb^{3+} fluorescence in ytterbium-doped silicate glasses. *IEEE J. Quantum. Electron.*, 36:1000, 2000. 127